7-18-2019

Fault Slip and Exhumation History of the Willard Thrust Sheet, Sevier Fold-Thrust Belt, Utah: Relations to Wedge Propagation, Hinterland Uplift, and Foreland Basin Sedimentation

W. A. Yonkee
Weber State University, ayonkee@weber.edu

Bryan Eleogram
University of Nevada, Las Vegas

Michael L. Wells
University of Nevada, Las Vegas, michael.wells@unlv.edu

Daniel F. Stockli
University of Texas at Austin

Shari Kelley
New Mexico Tech

See next page for additional authors

Repository Citation
Yonkee, W. A., Eleogram, B., Wells, M. L., Stockli, D. F., Kelley, S., Barber, D. E. (2019). Fault Slip and Exhumation History of the Willard Thrust Sheet, Sevier Fold-Thrust Belt, Utah: Relations to Wedge Propagation, Hinterland Uplift, and Foreland Basin Sedimentation. *Tectonics* 1-44. American Geophysical Union.
http://dx.doi.org/10.1029/2018TC005444

Authors
W. A. Yonkee, Bryan Eleogram, Michael L. Wells, Daniel F. Stockli, Shari Kelley, and D. E. Barber

AGU100 ADVANCING EARTH AND SPACE SCIENCE

Tectonics

RESEARCH ARTICLE
10.1029/2018TC005444

Key Points:
- New thermochronometric data constrain the fault slip and exhumation history of the Willard thrust sheet, western Sevier belt
- Major slip on the Willard thrust from 125 to 90 Ma was synchronous with increased foreland sedimentation and hinterland crustal thickening
- Fault-slip histories of dominant thrust sheets in the Sevier belt reflect evolving plate margin dynamics and primary crustal architecture

Supporting Information:
- Supporting Information S1
- Table S1
- Table S2
- Table S3

Correspondence to:
W. A. Yonkee,
ayonkee@weber.edu

Citation:
Yonkee, W. A., Eleogram, B., Wells, M. L., Stockli, D. F., Kelley, S., & Barber, D. E. (2019). Fault slip and exhumation history of the Willard thrust sheet, Sevier fold-thrust belt, Utah: Relations to wedge propagation, hinterland uplift, and foreland basin sedimentation. *Tectonics*, *38*. https://doi.org/10.1029/2018TC005444

Received 5 DEC 2018
Accepted 23 MAY 2019
Accepted article online 18 JUL 2019

Fault Slip and Exhumation History of the Willard Thrust Sheet, Sevier Fold-Thrust Belt, Utah: Relations to Wedge Propagation, Hinterland Uplift, and Foreland Basin Sedimentation

W. A. Yonkee[1], B. Eleogram[2], M. L. Wells[2], D. F. Stockli[3], S. Kelley[4], and D. E. Barber[3]

[1]Department of Geosciences, Weber State University, Ogden, UT, USA, [2]Department of Geoscience, University of Nevada, Las Vegas, Las Vegas, NV, USA, [3]Department of Geological Sciences, University of Texas at Austin, Austin, TX, USA, [4]New Mexico Bureau of Geology and Mineral Resources, New Mexico Tech, Socorro, NM, USA

Abstract Zircon (U-Th)/He (ZHe) and zircon fission track thermochronometric data for 47 samples spanning the areally extensive Willard thrust sheet within the western part of the Sevier fold-thrust belt record enhanced cooling and exhumation during major thrust slip spanning approximately 125–90 Ma. ZHe and zircon fission track age-paleodepth patterns along structural transects and age-distance relations along stratigraphic-parallel traverses, combined with thermo-kinematic modeling, constrain the fault slip history, with estimated slip rates of ~1 km/Myr from 125 to 105 Ma, increasing to ~3 km/Myr from 105 to 92 Ma, and then decreasing as major slip was transferred onto eastern thrusts. Exhumation was concentrated during motion up thrust ramps with estimated erosion rates of ~0.1 to 0.3 km/Myr. Local cooling ages of approximately 160–150 Ma may record a period of regional erosion, or alternatively an early phase of limited (<10 km) thrust slip. Propagation of the Sevier wedge front and major thrust slip during the late Early to mid-Cretaceous were synchronous with increasing subsidence and deposition of thick synorogenic strata in the foreland, crustal thickening in the hinterland, growing igneous activity in the Sierran magmatic arc, and increasing plate convergence rates. Along-strike, other parts of the Cordilleran retroarc fold-thrust belt also experienced major shortening during the late Early to mid-Cretaceous, following a period of earlier Cretaceous quiescence. Late Jurassic shortening was concentrated nearer the arc, and thus mostly in the hinterland at the latitude of northern Utah, related to width and location of the passive-margin sedimentary wedge relative to the plate margin.

1. Introduction

Quantifying the timing and rates of fault slip within retroarc fold-thrust belts, documenting relations between upper crustal shortening in thrust belts and lower crustal thickening and growth of orogenic plateaus in hinterlands, and determining responses of foreland basins to thrust loading and sediment redistribution are fundamental to understanding the evolution of Cordilleran style orogenic systems. The Sevier fold-thrust belt, which forms a key component of the North American Cordillera, is one of the best studied retroarc fold-thrust belts on Earth, and has served as a natural laboratory for seminal studies of thrust mechanics and kinematics (e.g., Boyer & Elliott, 1982; Hubbert & Rubey, 1959) and foreland basin evolution (e.g., DeCelles & Giles, 1996; Jordan, 1981). However, questions remain on thrust timing with possible shortening pulses, along-strike linkages of fault systems, and relations to changing plate margin dynamics (DeCelles & Coogan, 2006; DeCelles & Graham, 2015; Giallorenzo et al., 2018; Heller & Paola, 1989; Pana & van der Pluijm, 2015).

The North American Cordillera formed during protracted Jurassic to Paleogene subduction and terrane accretion, with development of an accretionary complex, fore-arc basin, magmatic arc, hinterland plateau, retroarc fold-thrust belt, and broad foreland basin (Figure 1; see reviews by DeCelles, 2004; Dickinson, 2004; Yonkee & Weil, 2015). Contraction within the retroarc was accommodated within an evolving orogenic wedge that at the latitude of northern Nevada to Utah grew to a width of ~1,000 km and included the Jurassic Luning-Fencemaker belt that developed in back arc basin strata (Wyld, 2002), the Late Jurassic(?) to Early Cretaceous central Nevada belt that developed along the shelf-slope transition (Long et al., 2014; Taylor et al., 2000), a hinterland belt with a complex history of Late Jurassic to Paleogene crustal thickening and later upper crustal extension (Camilleri & Chamberlain, 1997; Druschke et al., 2011;

10.1029/2018TC005444

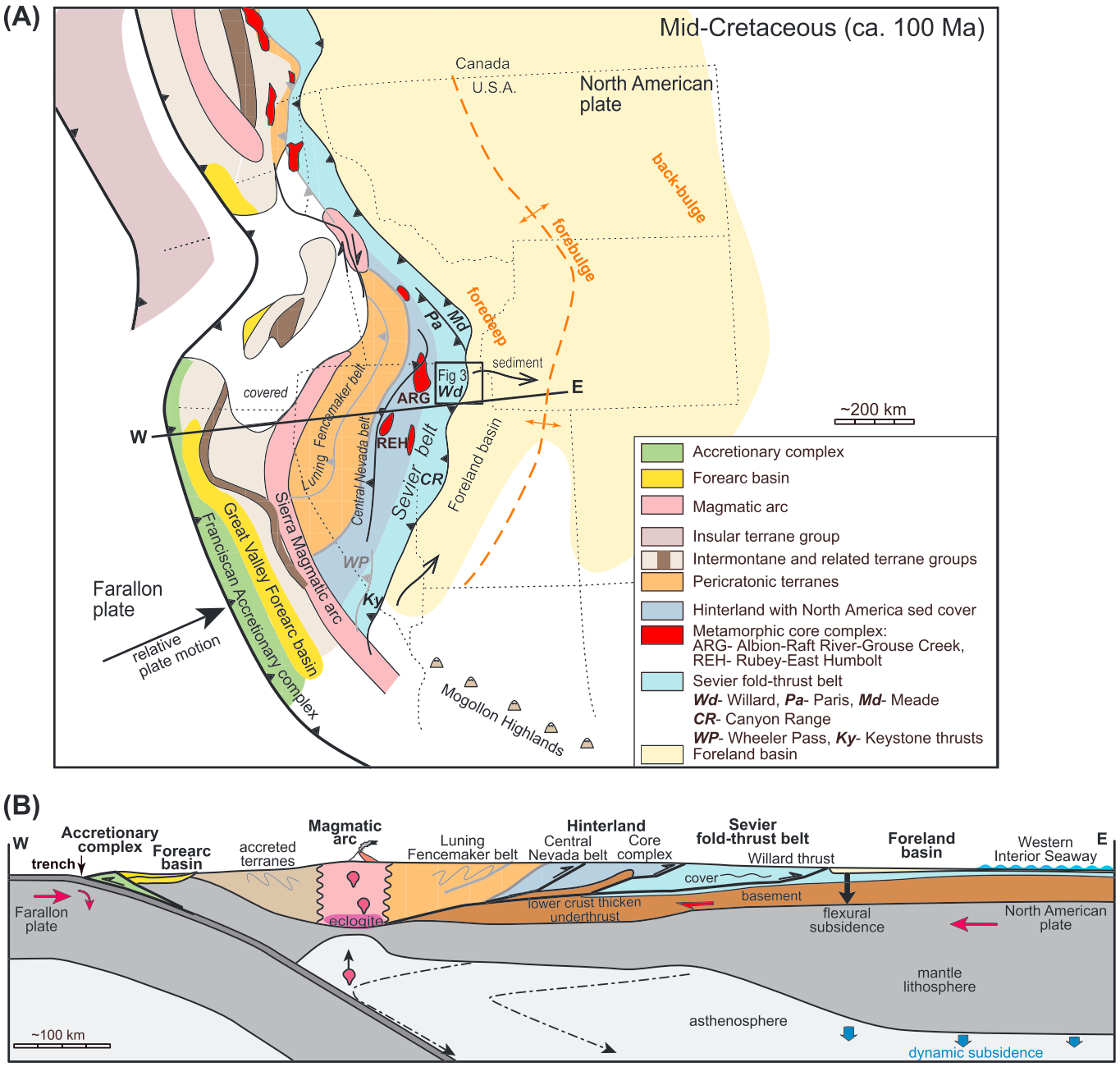

Figure 1. (a) Palinspastically restored tectonic map shows components of the North American Cordillera orogenic system at approximately 100 Ma, including the Sevier fold-thrust belt and Willard thrust (box outlines study area in Figure 3). Dotted lines are palinspastically restored state boundaries. (b) Schematic lithospheric cross section shows relations among the trench, accretionary complex, fore-arc basin, magmatic arc, hinterland, Sevier belt, and foreland basin. Thin-skinned shortening in the Sevier belt is balanced by lower crustal thickening in the hinterland. Synorogenic strata are deposited across the foreland basin (with foredeep, forebulge, back-bulge zones) that forms in response to flexure from thrust loading and regional dynamic subsidence.

McGrew et al., 2000; Wells, 1997; Wells et al., 2012), and the mostly Early Cretaceous to Early Eocene Sevier fold-thrust belt that developed in passive-margin to platform strata (Armstrong, 1968; Royse, 1993; Yonkee & Weil, 2015). For this paper, the term "Sevier belt" is used for the region dominated by thin-skinned thrusting, whereas "hinterland" is used for the region marked by middle to lower crustal metamorphism and thickening. Although a general west to east progression in deformation across the retroarc is well documented (DeCelles, 2004), timing and rates of thrust slip across different belts remain incompletely understood. The western part of the Sevier belt is dominated by the Willard and Canyon Range thrusts in

northern to central Utah, which experienced large-magnitude (~50 to 100 km) slip. Previous interpretations for the age of initial slip in this western system have varied widely, from approximately 150 to 110 Ma, reflecting ambiguous relations of foreland basin strata and limited thermochronometric data (Armstrong & Oriel, 1965; Burtner & Nigrini, 1994; Currie, 1998; DeCelles et al., 1995; DeCelles & Coogan, 2006; Heller et al., 1986; Heller & Paola, 1989). Despite the importance of these dominant western thrust sheets to the total shortening budget and mechanical evolution of the orogenic wedge, uncertainties remain on spatial-temporal patterns of fault slip.

Timing and rates of thrust fault slip can be constrained from crosscutting relations, depositional patterns of synorogenic strata, geochronology of deformation fabrics, and thermochronometric studies of hanging wall cooling and exhumation (Figure 2). Crosscutting relations bracket the timing for onset and cessation of faulting, but constraints may only be broad if key strata are removed by erosion or are not exposed. Subsidence patterns of synorogenic strata provide a record of flexural loading during thrust sheet emplacement, redistribution of mass by erosion and sediment deposition, and regional dynamic subsidence, but separating contributions from multiple processes is challenging (e.g., Liu et al., 2014; Painter & Carrapa, 2013). Provenance of synorogenic strata, based on conglomerate clast counts, sandstone petrography, and detrital zircon U-Pb age patterns, provides a record of thrust sheet unroofing (e.g., DeCelles, 1994; Dickinson & Gehrels, 2008; Lawton et al., 2010; Laskowski et al., 2013; Gentry et al., 2018), but preservation of clasts during erosion and transport depends on source rock type, evolving topography, and climate, and care is needed to compensate for varying zircon fertility of different bedrock sources. Geochronologic studies of deformation fabrics, such as fault gouge at shallow levels, and shear zones and strain fringes at deeper levels, provide quantitative ages (e.g., Pana & van der Pluijm, 2015; Wells et al., 2008), but may only record parts of the deformation and associated fluid-alteration history.

A powerful approach to constrain the timing and rates of fault slip and associated exhumation is from thermochronometric studies (e.g., Brandon et al., 1998; Reiners & Brandon, 2006; Reiners & Ehlers, 2005). Many prior studies have examined timing of footwall exhumation in extensional tectonic settings (e.g., Brichau et al., 2006; Singleton et al., 2014; Stockli, 2005; Stockli et al., 2001; Wells et al., 2000). While applications to reverse faults have increased (e.g., Anderson et al., 2018; Carrapa et al., 2011; Fosdick et al., 2015; Herman et al., 2010; Long et al., 2012; Parra et al., 2009; von Hagke et al., 2012), quantifying thermal effects associated with varying fault slip rates and exhumation in structurally complex areas is challenging. Estimates for the onset, duration, and rates of contractional deformation can be improved by integrating systematic sampling with sequential structural restorations and thermal modeling (e.g., Almendral et al., 2015; Lock & Willett, 2008; Mancktelow & Grasemann, 1997; McQuarrie & Ehlers, 2015; Rak et al., 2017). Sampling designs include (i) vertical transects across structural levels to determine cooling age-depth relations, (ii) horizontal traverses parallel to fault slip directions, and (iii) use of multiple thermochronometers to determine temperature-time (*T*-*t*) paths (Figure 2; Reiners & Brandon, 2006). Exhumation above thrust ramps results in decreasing cooling ages with increasing structural depth, as progressively deeper levels are advected through closure isotherms of thermochronometric systems. The top and bottom inflections of a steeper age-depth gradient record onset and cessation of enhanced cooling during thrust slip. In detail, isotherms may change position during deformation due to heat advection from fault slip and erosion, which can be evaluated with thermo-kinematic modeling (Almendral et al., 2015). Exhumation rates, however, also partly depend on evolving topography, climate, and rock erodibility, in addition to kinematic uplift rates tied to fault slip, which can be evaluated from unroofing histories preserved in synorogenic strata.

In this paper we integrate zircon (U-Th)/He (ZHe) and zircon fission track (ZFT) thermochronometric analysis of the Willard thrust sheet with thermo-kinematic modeling to address the following questions.

1. What were the ages for onset and cessation of fault slip in the western part of the Sevier fold-thrust belt at the latitude of northern Utah, and did slip rates vary temporally?
2. What were the connections between thrust sheet emplacement and sedimentation patterns of the foreland basin?
3. What were the relations between upper crustal shortening in the Sevier belt and lower crustal thickening and topographic growth in the hinterland?
4. What were the along-strike variations in fault timing and linkages within the Sevier belt and relations to plate margin dynamics?

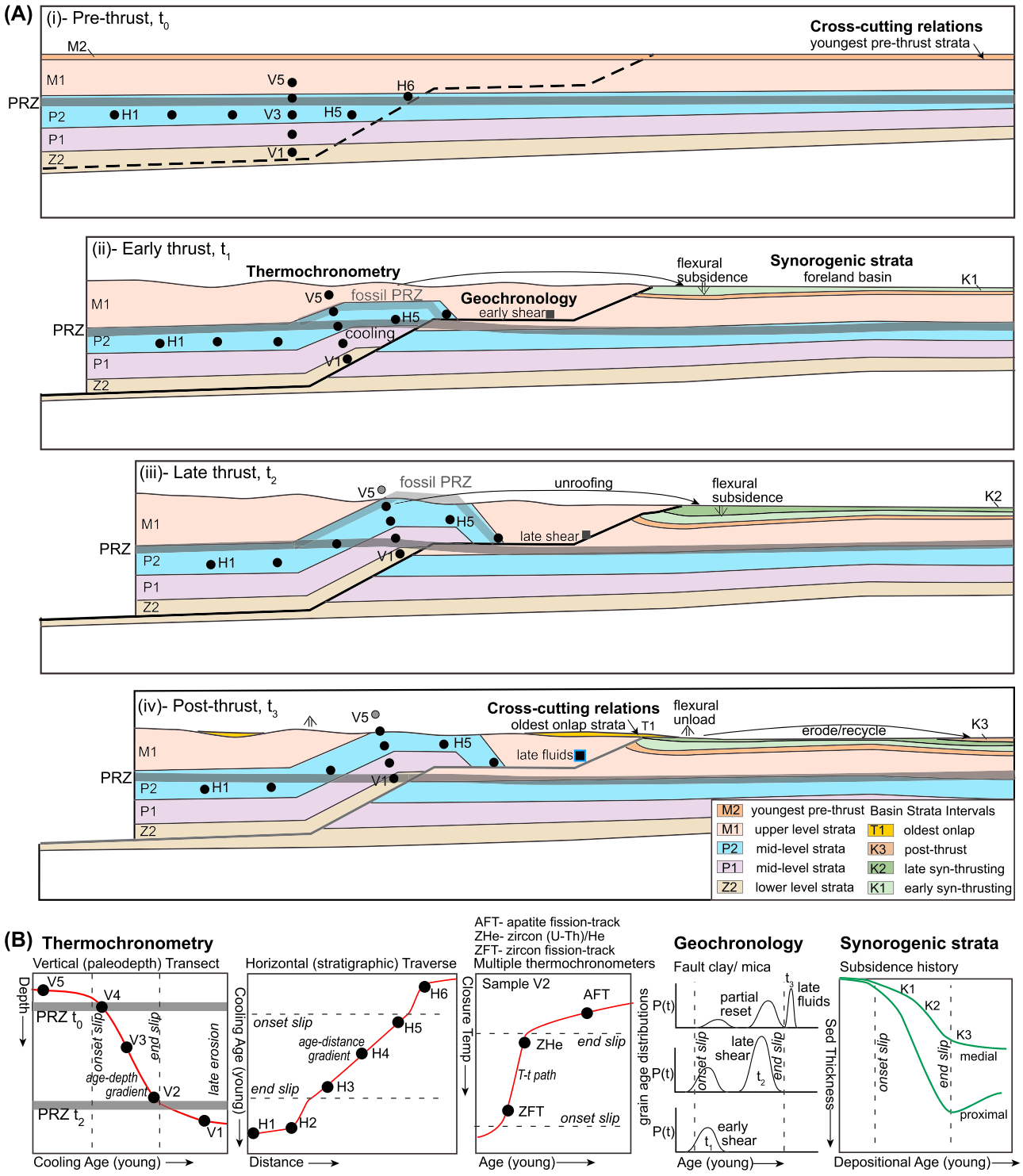

Figure 2. Conceptual model for determining timing of thrust fault slip using thermochronometry, geochronology, synorogenic strata, and crosscutting relations. (a) Schematic cross sections show (i) prethrust, (ii) early and (iii) late synthrust, and (iv) postthrust relations. Rocks within the thrust sheet are progressively uplifted through a partial retention zone (PRZ) during fault slip and erosion, while synorogenic strata are deposited in a foreland basin. (b) Cooling age-paleodepth relations along a vertical transect (*V*) record enhanced cooling during fault slip, cooling age-distance relations across a horizontal traverse (*H*) reflect ramp position and slip rate, and multiple thermochronometers record *T*-*t* paths. Geochronologic ages of fault rocks record early to late shear and fluid alteration. Subsidence patterns of synorogenic strata reflect flexural loading during thrusting and redistribution of mass by erosion and sedimentation.

The Willard thrust sheet is ideally suited for application of the ZHe and ZFT systems that have closure temperatures of ~160 to 250 °C and record upper crustal exhumation through depths of ~6 to 12 km (Reiners & Brandon, 2006). The Willard thrust sheet contains abundant siliciclastic strata exposed over this paleodepth range, and much of the sheet experienced >4 km of structural throw and exhumation. ZHe and ZFT data are presented for four paleodepth transects and three stratigraphic-parallel traverses across the sheet, providing key constraints for timing and rates of contractional deformation within part of the North American Cordilleran system.

2. Geologic Setting

The western part of the Sevier belt includes the areally extensive Willard thrust sheet in northern Utah, and related Paris and Meade thrust sheets in southeast Idaho, which carry thick passive-margin strata and were emplaced >50 km eastward (Figure 3; Crittenden, 1972; Yonkee, 2005). The Willard thrust sheet is well exposed due to younger differential uplift and erosion above the basement-cored Wasatch anticlinorium that developed during later Cretaceous to Paleocene slip on more eastern thrusts, and in footwalls of Neogene Basin-and-Range normal faults. This differential uplift exhumed a range of structural levels, providing a composite, down-plunge view of the thrust sheet. The Willard thrust has a stair-step geometry with a western flat at the base of micaceous Neoproterozoic strata, a composite western ramp (structural relief ~5 km) with a local flat at the base of Neoproterozoic quartzite, a central flat in Middle Cambrian shale, and an eastern ramp (structural relief ~5 km) up to an eastern flat in Jurassic evaporite-bearing strata. The thrust likely had a frontal ramp through Lower Cretaceous synorogenic strata that are preserved to the north at Red Mountain along the leading edge of the Meade thrust (DeCelles et al., 1993). The Willard sheet displays large-scale fault-bend and fault-propagation folds, locally modified by shear. The main Willard thrust has 50 km of top-to-ESE slip, with an additional 10 km of shortening from folds and slip on the imbricate Providence thrust (Figure 3b). Upper levels of the Willard sheet are relatively little deformed, but internal deformation increases downward and westward in the sheet, with development of tectonic foliation that records a component of thrust-parallel simple shear (Yonkee et al., 2013). The lower, western part of the Willard sheet underwent greenschist-facies metamorphism with neocrystallization of muscovite, biotite, and chloritoid in slate (Condie, 1967; Yonkee, 2005).

The geometry of the Willard thrust was influenced by primary stratigraphic architecture (Figure 4). The Willard sheet carries Neoproterozoic to Devonian passive-margin strata that thicken westward, from ~3 km along the frontal part of the sheet to ~8 km in the western part. Eastward in the Willard footwall, Neoproterozoic strata are absent and Cambrian to Devonian platform strata are <2 km thick. Mississippian to Permian strata deposited during early breakup of the passive margin thicken from ~1.5 km along the frontal part of the sheet to locally >4 km in the Oquirrh Basin toward the west. Triassic to Middle Jurassic strata have been mostly eroded from the Willard sheet, but are preserved in the footwall and parts of the Meade sheet to the north, where they have a combined thickness of ~3 to 4 km. Triassic strata are also locally preserved farther west toward the hinterland. During the Middle to early Late Jurassic, subsidence increased with deposition of the Twin Creek, Preuss, and Stump Formations that record increasing siliciclastic input from western sources, followed by development of an erosional unconformity across the future Sevier belt, while the hinterland in western Utah to Nevada underwent local shortening and intrusion of granitic plutons (Allmendinger & Jordan, 1984; Miller et al., 1997).

The Willard thrust sheet, and associated Paris and Meade thrust sheets to the north, had a protracted deformation and exhumation history based on crosscutting relations, characteristics of synorogenic strata, and limited apatite fission track data, but details of slip history are uncertain. The Willard thrust cuts Middle Jurassic strata along its frontal trace, whereas flat-lying Paleocene to Early Eocene strata locally overlie eastern to central parts of the sheet (Coogan & King, 2016; Dover, 1995), broadly bracketing the timing of deformation. The mostly Aptian (125–113 Ma) lower part of the Gannett Group may record early slip on the Paris thrust, but the age of basal strata and their relation to thrusting are debated (Armstrong & Oriel, 1965; Heller et al., 1986). The Albian (113–105 Ma) upper part of the Gannett Group contains thick proximal conglomerates that record unroofing and major slip on the Meade thrust (DeCelles et al., 1993). Upper Albian to Turonian strata record continued unroofing of the Willard sheet (Gentry et al., 2018). Apatite fission track ages of 111 ± 8 to 141 ± 34 Ma along the Paris and Meade thrusts record cooling during the Early

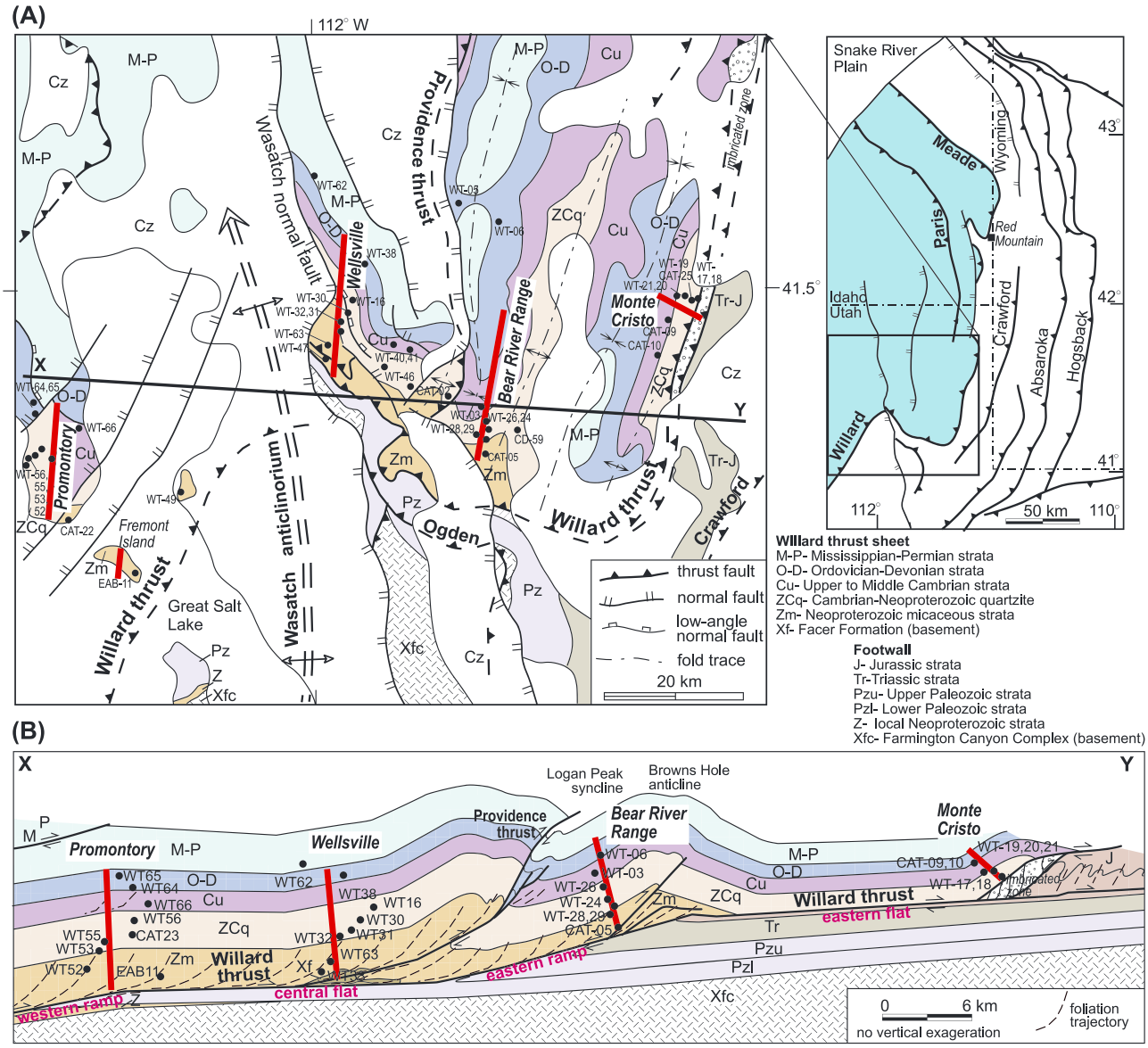

Figure 3. (a) Generalized geologic map of the Willard thrust sheet showing locations of structural (paleodepth) transects: Promontory (plus Fremont Island), Wellsville, Bear River Range, and Monte Cristo. Tilting of the Willard sheet above the north plunge of the Wasatch anticlinorium resulted in exposure of a wide range of structural levels. Inset shows locations of the Willard-Paris-Meade sheet (blue), Red Mountain where proximal synorogenic strata are preserved, and other major thrusts in the Wyoming salient of the Sevier belt. (b) Cross section of the Willard thrust sheet, incorporating down-plunge projections and with effects of subsequent uplift of the Wasatch anticlinorium and Neogene extension removed. The thrust has a ramp-flat geometry and transported thick passive margin strata eastward. Projected positions of samples and paleodepth transects indicated. Section modified from Yonkee (2005).

Cretaceous (Burtner & Nigrini, 1994). The $^{40}Ar/^{39}Ar$ laser probe ages of muscovite and biotite in the western, basal part of the Willard thrust sheet, which experienced lower greenschist facies metamorphism, range mostly from 140 to 125 Ma (Wells et al., 2015). Muscovite grew slightly below the closure T of ~400 °C, recording crystallization during shear that preceded to overlapped with onset of major thrust slip. Biotite ages may record crystallization or slight cooling during early exhumation.

Following emplacement of the Willard thrust sheet, slip propagated eastward onto the Crawford, Absaroka, and Hogsback thrusts, as recorded by Upper Cretaceous to Lower Eocene synorogenic strata (DeCelles, 1994; Wiltschko & Dorr, 1983). Imbricate slices of basement were incorporated into the Wasatch anticlinorium during slip on the eastern thrusts (Yonkee, 1992), and parts of the Willard sheet were uplifted and eroded during later Cretaceous growth of the anticlinorium (DeCelles, 1994). Thus, major slip on the

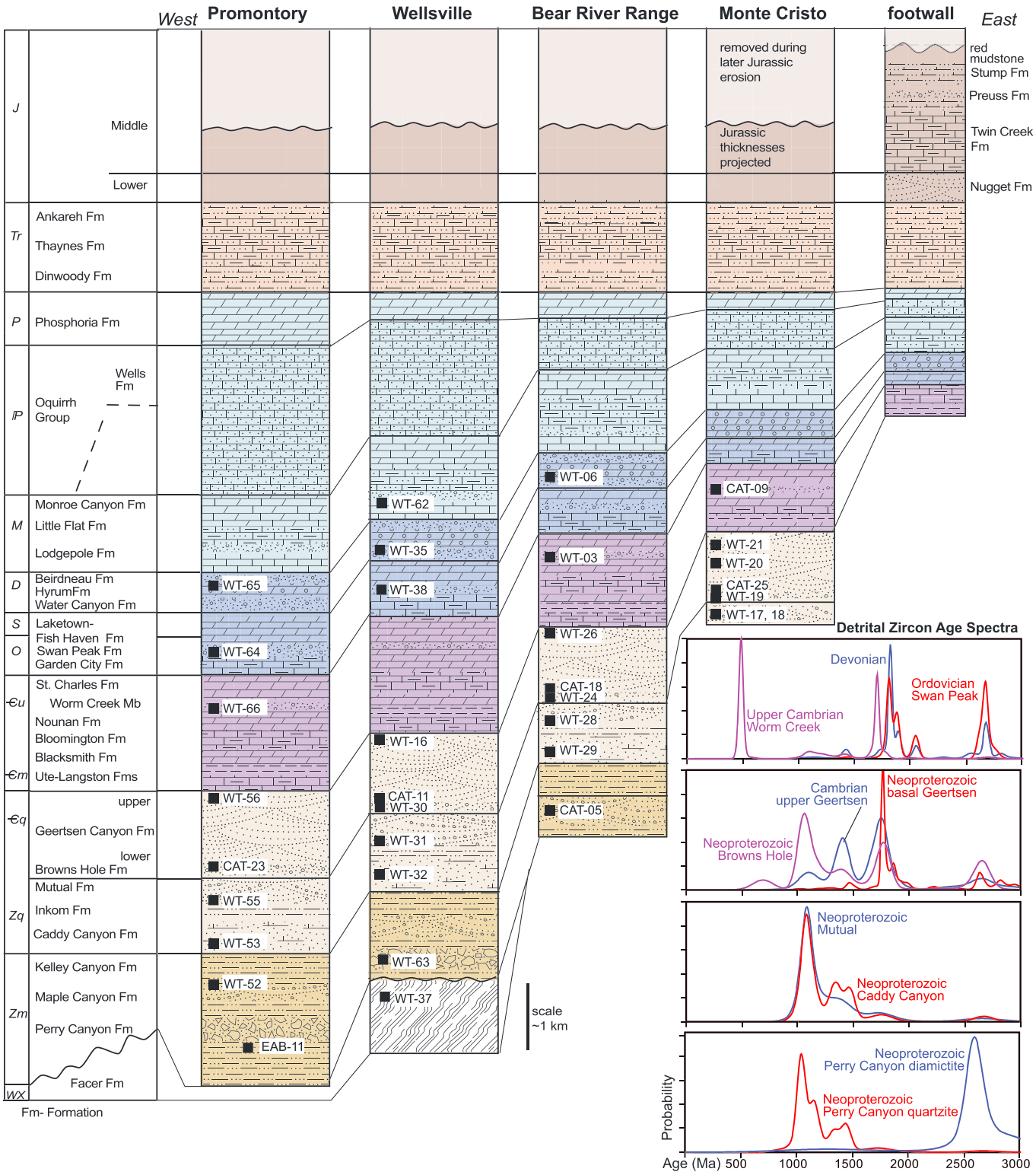

Figure 4. Stratigraphic columns across the Willard thrust sheet show formation thicknesses and sample depths for the Promontory, Wellsville, Bear River Range, and Monte Cristo transects. Thicknesses of Triassic to Middle Jurassic strata that have been mostly eroded from the sheet are based on preserved relations in the Willard footwall and Meade sheet to the north. Detrital zircon U-Pb age spectra show distinctive patterns for different formations.

Willard-Paris-Meade thrusts is broadly bracketed to have occurred during the Early to mid-Cretaceous, followed by growth of the Wasatch anticlinorium, but the timing of initial fault slip and slip-rate history are uncertain.

3. Methods

3.1. Zircon (U-Th)/He and Fission Track Thermochronometric Systems

The zircon (U-Th)/He (ZHe) and zircon fission track (ZFT) systems have been widely applied to determine cooling histories at shallow (~5 to 15 km) crustal depths (Reiners & Brandon, 2006; Stockli, 2005). The ZHe system is based on accumulation of radiogenic ^{4}He produced by the alpha decay of U and Th, along with loss of He by thermally controlled diffusion (Farley, 2002; Reiners, 2005; Reiners et al., 2004). Borehole studies indicate partial retention of He in zircon begins at depths where T ~180–200 °C, with essentially complete retention at depths where T ~130–140 °C, defining the base and top of the ZHe partial retention zone (PRZ), respectively (Stockli, 2005; Wolfe & Stockli, 2010). For cooling rates of 1 to 10 °C/Myr and grain sizes of 40 to 80 μm, the ZHe system has an estimated closure temperature of ~160–190 °C for a simple Arrhenius relation (Reiners, 2005). ZHe closure temperature, however, also depends on accumulated radiation damage that influences He diffusivity (Guenthner et al., 2013; Ketcham et al., 2013). Guenthner et al. (2013) proposed a model in which He diffusivity decreases with increasing radiation damage below a percolation threshold, and then increases (closure T decreases) above the threshold. This model can be used to calculate ZHe ages for grains with a range of U-Th contents (represented by eU = U + 0.235*Th in ppm) and sizes for a given thermal history, and predicts large dispersion in cooling ages for grains not heated above 200 °C (Figure 5). Interpretation of ZHe ages of detrital grains in sedimentary rocks presents additional challenges as grains may have experienced different basement thermal histories prior to erosion and deposition, resulting in variable inheritance of He and radiation damage. By combining calculated ZHe-eU relations for maximum inheritance, based on the U-Pb age of a grain, and zero inheritance prior to deposition, a composite envelope can be constructed (Figure 5). Key features of the envelope include younger ZHe ages along its lower part that record timing of enhanced cooling, and older ages of retentive grains with He inheritance related to maximum temperature and basement source age. For rocks heated above 200 °C, He inheritance is negligible, ZHe ages are reset prior to cooling, and grain ages define a quasi-normal distribution with a mean age similar to that estimated using a simple Arrhenius relation (Reiners, 2005).

The ZFT system is based on accumulation of fission tracks produced by spontaneous fission of ^{238}U, along with thermally controlled annealing that reduces track length and density (Gleadow et al., 1976). Various annealing models have been proposed based on experimental data, but annealing mechanisms are incompletely understood (Guedes et al., 2013; Tagami et al., 1998; Yamada et al., 2007), and studies of naturally exhumed crustal sections indicate a wide range of annealing behaviors that depend on accumulated radiation damage (Garver et al., 2005; Reiners & Brandon, 2006). For cooling rates of 1 to 10 °C/Myr, the ZFT system has an estimated closure T of ~200–250 °C for grains with moderate levels of radiation damage, based on relations in exhumed crustal sections (Bernet, 2009; Brandon et al., 1998). In comparison, the calculated closure T for annealed (zero-damage) zircon is 290–310 °C, based on extrapolation of experimental studies to geologic cooling rates (Rahn et al., 2004). The ZFT partial annealing zone (PAZ) has a wide temperature range of ~150–300 °C based on dispersion of grain ages in exhumed crustal sections (Bernet, 2009). For samples heated above the PAZ and subsequently exhumed, all grains are reset and have young FT ages related to cooling during exhumation. For samples heated into the higher-temperature part of a fossil PAZ, individual grains vary from partly to totally reset, with less retentive grains defining a young age subgroup related to cooling during exhumation. For samples only heated into the lower temperature part of a fossil PAZ, most grains are only partly reset and do not directly record timing of exhumation.

3.2. Sampling Design

A total of 47 samples of siliciclastic rocks were collected and analyzed for ZHe and ZFT thermochronometry from the Willard thrust sheet. Thirty-seven samples were collected along four structural (paleodepth) transects: (1) Monte Cristo in the eastern (frontal) part of the sheet, (2) Bear River Range in the central part, (3) Wellsville in the west-central part, and (4) Promontory in the western part (Figure 3). Samples were collected at a paleodepth spacing of ~1 km, focusing on the following units: Neoproterozoic Perry Canyon Formation at the lowest level, Neoproterozoic Caddy Canyon and Mutual Formations at lower levels, uppermost

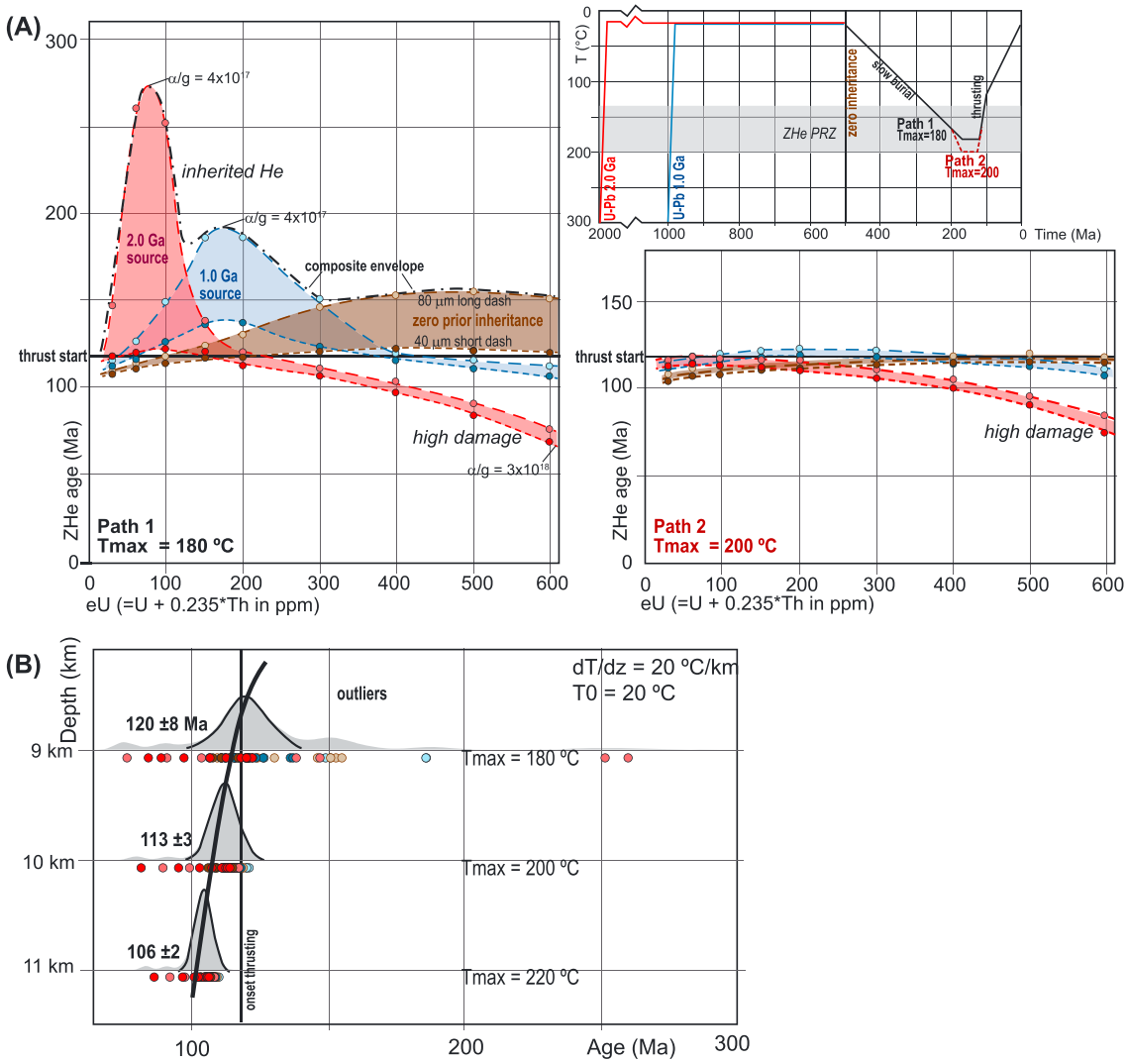

Figure 5. (a) Model of ZHe age-eU relations for detrital zircon grains with varying basement source ages and thermal histories (T_{max} = 180 °C and 200 °C for paths 1 and 2, respectively, and rapid cooling from 120 to 100 Ma). Colored envelopes and dots show ZHe-eU values for grains sourced from 2.0-Ga basement (red), 1.0-Ga basement (blue), and zero inheritance (brown), calculated using HeFTY software (Ketcham, 2005) and model of Guenthner et al. (2013). Zircon grains that warm into the partial retention zone (T_{max} = 180 °C) display large dispersion in ZHe ages related to varying inherited He. Grains heated above 200 °C have prior He degassed, but partly retain radiation damage that affects diffusion, which increases (ZHe ages decrease) for radiation damage >4 × 10^{17} alpha/g. (b) Model of ZHe age-paleodepth relations for a transect spanning T_{max} = 180 to 220 °C, erosion rate of 0.2 km/Myr, and thermal gradient of 20 °C/km. ZHe grain ages display wide dispersion at shallow levels, and converge at deeper levels with mean age similar to age estimated from the Arrhenius relation of Reiners et al. (2004) (black line). Probability density functions of ZHe grain ages (gray fill) define quasi-normal distributions, along with outlier older ages at shallow levels and younger ages for high-damage grains.

Neoproterozoic to Lower Cambrian Browns Hole and Geertsen Canyon Formations at middle levels, and siliciclastic layers in carbonate-rich Paleozoic strata (Upper Cambrian Worm Creek Member, Ordovician Swan Peak Formation, and Devonian Water Canyon and Beirdneau Formations) at upper levels (Figure 4). Additional samples were collected for three stratigraphic-parallel traverses along the Perry Canyon, Browns Hole, and Worm Creek units across the thrust sheet. Paleodepths of samples were estimated from preserved thicknesses of Neoproterozoic to Permian strata, along with an estimated ~3- to 4-km thickness for Triassic to Middle Jurassic strata that were partly removed by erosion prior to onset of major thrust slip.

Each sampled unit has a distinctive detrital zircon U-Pb age distribution, based on laser ablation–inductively coupled plasma–mass spectrometry dating of grains (Figure 4). Diamictite and quartzite layers in the Neoproterozoic Perry Canyon Formation contain mostly Archean and 1.0–1.3-Ga grains, respectively.

Quartzite in the Neoproterozoic Caddy Canyon, Mutual, and Browns Hole formations contains abundant 1.0–1.3-Ga grains. The Geertsen Canyon Formation contains abundant 1.7–1.8-Ga and some 1.0–1.3-Ga grains. The Worm Creek Member contains a distinctive group of 0.5-Ga grains, along with some older grains. Ordovician and Devonian strata contain abundant 1.8–2.1-Ga grains. These age distributions are similar to those reported by Yonkee et al. (2014).

3.3. Analytical Techniques

Samples were crushed and mineral separates obtained using standard water table, magnetic, and heavy-liquid techniques. Zircon separates for each sample were then observed with transmitted and polarizing light microscopy and ~30 grains were handpicked for potential ZHe analysis, based on being free of visible fractures and inclusions, and having overall tetragonal shapes with widths of ~60 to 100 μm and lengths of ~200 μm (giving equivalent spherical radii of ~35 to 80 μm).

ZHe analysis was completed at the UTChron Laboratory of the University of Texas at Austin following the procedures of Wolfe and Stockli (2010). Zircon grains were first prescreened following the analytical procedures of Marsh and Stockli (2015). For prescreening, zircon grains were mounted on adhesive tape and laser ablation–inductively coupled plasma–mass spectrometry was used to measure U-Th-Pb contents over depth profiles of ~20 μm, with U-Pb ages calculated using IOLITE software (Petrus & Kamber, 2012). Six suitable grains per sample were then selected for ZHe analysis, based on consistent U-Th concentrations in profiles, moderate eU (= U + 0.235*Th) of ~30–300 ppm, and U-Pb ages mostly from 1.0 to 2.0 Ga, giving broadly similar values of maximum accumulated radiation damage. Selected grains were photographed and measured to calculate alpha-ejection correction factors following the method of Farley (2002). Grains were packed in platinum tubes and degassed in an ultrahigh-vacuum extraction line by diode laser at 1,300 °C for 10 min until total (>99%) He extraction. Following He degassing, grains were dissolved by HF-HCl pressure-vessel digestion and grain U-Th contents determined using inductively coupled plasma–mass spectrometry with isotope dilution.

Analytical uncertainty in individual grain He ages had a standard error of ±4% of grain age, based on long-term reproducibility of laboratory age standards. As typically observed in ZHe studies of natural zircons, most samples in this study displayed dispersion among individual grain ages greater than analytical uncertainty (typical sample $1\sigma \approx \pm 10\%$ of mean age), likely reflecting variations in He diffusivity related to accumulated radiation damage, variable inherited He in retentive grains, U-Th zonation that affects diffusion profiles and correction for alpha ejection, grain defects, and nonideal grain shapes (Hourigan et al., 2005; Guenthner et al., 2013; Bargnesi et al., 2016; Danisik et al., 2017). Zircon grains with anomalous ZHe ages (ages $>3\sigma$ removed from the sample mean, likely related to extreme inheritance or incomplete U-Th recovery during grain dissolution) were identified as outliers using the Grubbs and modified Z value methods (Iglewicz & Hoaglin, 1993), and were not used to calculate sample mean ZHe ages. Mean ages and 1σ values, which approximate the 95% confidence interval in age for a sample with six grains, are listed in Table 1. Individual grain U-Th contents, He contents, and sizes are listed in Table S1 and laser ablation–inductively coupled plasma–mass spectrometry U-Pb ages are listed in Table S2 in the supporting information.

ZFT analysis was completed at the New Mexico Bureau of Geology and Mineral Resources. Samples were prepared for fission track dating using the external detector method (Naeser, 1979) so that individual grain ages could be determined. Zircon grains were sprinkled on glass slides, mounted in TEP Teflon tape, polished to expose the grains, and etched in an eutectic NaOH-KOH mixture at 230 °C. Most samples contained multiple detrital zircon subgroups, based on differing optical properties and etching characteristics. Consequently, three to four slide mounts were made for each sample and etched for different amounts of time to attain optimum etch conditions for each subgroup. Zircon grain mounts were then covered with muscovite detectors and placed in a reactor package with Fish Canyon zircon age standards and Corning (CN-5) fission track glass standards. Sample mounts and standards were irradiated at the Texas A&M Nuclear Science Center at a nominal fluence of 2×10^{15} n/cm^2, which was calibrated with a zeta value of 422 ± 67, determined using CN5 glass and an age of 28.0 ± 0.7 Ma for the Fish Canyon standard (Green & Hurford, 1983). Spontaneous and induced tracks were counted for 20 grains for most samples.

Analytical uncertainty in individual grain FT ages, related to counting statistics, had a standard error of ±8 to 15% of grain age. Grain ages were transformed by $z_j = \ln(t_j)$ and $s_j = \sigma_j/t_j$, where t_j is the calculated age of

10.1029/2018TC005444

Table 1
Summary of Sample ZHe Ages and ZFT Ages

Sample	Unit[a]	Depth (km)[b]	ZHe (Ma)	Standard deviation	n/N[c]	Individual grain ZHe ages (Ma)[d]	FT-K (Ma)[e]	Standard deviation	FT-J (Ma)[e]	Standard deviation	nk/nj/N[f]
Monte Cristo Transect											
CAT-09	*Cw*	*7.4*	166	18	5/5	148,157,161,171,194	-	-	156	15	0/5/19
CAT-10	*Cw*	*7.4*					-	-	-	-	0/0/20
WT-21	*Cgu*	*8.3*	160	18	4/5	142,154,159,184,[399]					
WT-20	*Cg*	*8.6*	156	17	3/6	140,153,170,[220,224,248]					
CAT-25	*Zgl*	*9.0*					-	-	~160	-	0/1/13
WT-19	*Zb*	*9.0*	160	10	4/6	147,158,163,171,[204,234]					
WT-17, 18	*Zq*	*9.3*	159 pooled	18	10/12	125,143,152,182,[212,232] 150,153,168,173,176,177					
Bear River Transect											
WT-06	*D*	*7.1*	172	27	4/6	140,154,192,200,[307,494]					
WT-05	*D*	*7.1**	121	28	5/6	100,102,113,120,169,[482]					
WT-03	*Cw*	*8.2*	127	5	4/5	121,125,127,134,[208]					
WT-26	*Cgu*	*9.3*	112	8	5/6	103,107,110,120,123,[150]					
CAT-18	*Zgl*	*10.3*					-	-	-	-	0/0/10
WT-24	*Zb*	*10.4*	109	9	6/6	102,103,106,108,109,128					
WT-28	*Zm*	*10.8*	96	10	5/5	85,90,94,103,110					
WT-29	*Zc*	*11.1*	100	12	5/5	91,92,98,98,121	-	-	149	18	0/4/20
CAT-05	*Zmc*	*12.0*	78	6	4/6	71,78,79,85,[119,340]					
Wellsville Transect											
WT-62	*M*	*7.5*	121	10	6/6	105,116,117,123,128,132					
WT-35	*D*	*8.1*	129	14	5/6	107,123,134,135,145,[174]					
WT-38	*Os*	*8.8*	129	11	6/6	109.128,130,132,136,142					
WT-16	*Cgu*	*10.9*	104	15	5/6	83,98,103,115,121,[155]	121	16	162	24	10/10/20
CAT-11	*Zgl*	*11.9*					105	9	160	18	11/7/20
WT-30	*Zb*	*12.0*	97	6	6/6	90,91,95,98,102,106					
WT-31	*Zm*	*12.5*	87	10	5/6	78,80,84,90,103,[152]					
WT-32	*Zc*	*12.9*	88	17	5/5	63,84,87,96,110	102	15	-	-	20/0/20
WT-63	*Zp*	*14.4*	71	8	6/6	61,66,72,73,76,82	72	7	-	-	20/0/20
WT-37	*Xf*	*14.8*	63	4	3/6	60,61,67,[92,92,102]					
WT-47	*Zp*	*14.3**	24	6	6/6	18,18,23,23,31,32	74	8	-	-	13/0/13
Promontory Transect											
WT-65	*D*	*8.5*	126	16	4/6	109,117,131,140,[182,225]					
WT-64	*Os*	*9.4*	109	16	5/5	83,106,114,120,124					
WT-66	*Cw*	*10.3*	92	8	5/5	80,91,91,96,100	108	17	172	24	7/13/20
WT-56	*Cgu*	*11.5*	89	14	5/5	76,83,85,88,113	106	14	-	-	20/0/20
CAT-23	*Zgl*	*12.6*	88	10	5/6	77,77,90,96,97,[142]	100	15	-	-	20/0/20
WT-55	*Zm*	*13.0*	92	10	5/5	74,94,96,96,99					
WT-53	*Zc*	*13.7*	77	8	5/5	69,70,74,83,87	82	11	-	-	20/0/20
WT-52	*Zk*	*14.3*	54	4	5/6	51,52,53,57,59,[101]					
EAB-11	*Zp*	*15.0*	68	5	6/6	62,64,66,68,72,75					
Worm Creek Traverse											
CAT-09	*Cw*	*7.4*	166	18	5/5	See above	-	-	156	15	0/5/19
WT-03	*Cw*	*8.2*	127	5	4/5	See above					
WT-40	*Cw*	*8.8*	111	15	6/6	99,100,101,109,121,137					
WT-41	*Cw*	*8.8*	113	26	4/6	83,127,128,[165,168]					
WT-66	*Cw*	*10.3*	92	8	5/5	See above	108	17	172	24	7/13/20

10.1029/2018TC005444

Table 1
(continued)

Sample	Unit[a]	Depth (km)[b]	ZHe (Ma)	Standard deviation	n/N[c]	Individual grain ZHe ages (Ma)[d]	FT-K (Ma)[e]	Standard deviation	FT-J (Ma)[e]	Standard deviation	nk/nj/N[f]
Browns Hole Traverse											
WT-19	*Zb*	*9.0*	160	10	4/6	See above					
CD-59	*Zb*	10.2	119	20	5/6	[54],94,104,123,137,140					
WT-24	*Zb*	*10.4*	109	9	6/6	See above					
CAT-15	*Zgl*	*10.6*	107	16	7/8	77,80,106,116, 119,123,125	-	-	~150	-	0/3/18
CAT-01	*Zgl*	*10.9*	97	15	5/6	[74],81,82,99,106,117					
CAT-02	*Zgl*	*10.9*					123	7	146	7	8/9/17
WT-46	*Zb*	*11.4*	112	13	6/6	92,101,111,114,123,129	114	11	161	14	9/8/17
CAT-11	*Zgl*	*11.9*					106	9	160	18	11/7/20
WT-30	*Zb*	*12.0*	97	6	6/6	See above					
CAT-23	*Zgl*	*12.6*	88	10	5/6	See above	100	15	-	-	20/0/20
Perry Canyon Traverse											
WT-43	*Zp*	*14.0*	70	15	3/3	53,74,82	103	18	-	-	16/0/16
CAT-04	*Zp*	*14.0*					101	10	-	-	19/0/19
WT-63	*Zp*	*14.4*	71	8	6/6	See above	72	7	-	-	20/0/20
WT-49	*Zp*	*15.0*	67	5	6/6	62,64,66,68,71,75	77	11	-	-	20/0/20

[a]Units are M = Mississippian Little Flat Formation; D = Devonian Beirdneau/Water Canyon Formations; Os = Ordovician Swan Peak Formation; Cw = Cambrian Worm Creek Member, St. Charles Formation; Cgu and Zgl = Cambrian upper and Neoproterozoic basal parts of Geertsen Canyon Formation; and Zb, Zm, Zc, Zp = Neoproterozoic Browns Hole, Mutual, Caddy Canyon, and Perry Canyon Formations. For traverses, samples with light gray shading are also listed on corresponding transects. [b]Maximum depth is based on observed thicknesses of Neoproterozoic to Permian strata plus an estimated 4 km of Triassic to Middle Jurassic strata. Asterisk indicates sample experienced additional tectonic burial in imbricate thrust footwall. [c]n = number of grains used to calculate ZHe sample mean age, N = total number of analyzed grains in sample. [d]Individual grain ages listed from young to old. Outliers not used to calculate sample mean in brackets. [e]ZFT ages divided into subgroups, FT-K = Cretaceous age subgroup and FT-J = Jurassic age subgroup. [f]nk is the number of grains in Cretaceous subgroup, nj is the number of grains in Jurassic subgroup, and N is the total number of analyzed grains in the sample.

the jth grain and σ_j is the standard error in age of the jth grain based on numbers of spontaneous and induced tracks, and then plotted using the radial projection method of Galbraith (1990) and the probability density method of Brandon (1996). Samples from lower levels typically contained younger grains that displayed low dispersion ($1\sigma \approx 10\%$ of mean age), consistent with complete resetting of grains below the PAZ prior to cooling. Middle-level samples typically contained multiple age subgroups based on chi-square tests (Galbraith, 1981), consistent with resetting of less retentive grains in the higher-temperature part of the PAZ prior to cooling. Two approaches were used to identify and estimate mean ages of young subgroups: the binomial fit method of Brandon (2002) and identifying age clusters with a mean square weighted deviation of ~1. Both methods gave similar results. Upper level samples displayed large dispersion and lacked young grains, consistent with partial resetting in the lower temperature part of the PAZ prior to thrusting. Sample and subgroup mean ZFT ages and 1σ values are listed in Table 1. For a sample with 20 young grains, the 95% confidence interval in mean age is approximated by $0.5 \times 1\sigma$. Spontaneous and induced track counts of individual grains are listed in Table S3 in the supporting information.

3.4. Thermal Modeling

General geologic constraints and ZHe age-paleodepth relations were first used to construct idealized temperature-time (T-t) paths for samples along each transect, assuming a constant geothermal gradient and fixed exhumation rates during prethrust, synthrust, and postthrust stages. The QTQt software package (Gallagher, 2012) was used to explore potential ranges of T-t paths consistent with ZHe age-paleodepth relations for each transect. Potential T-t paths for samples at upper levels were also evaluated from relations among U-Th contents, U-Pb ages, and ZHe grain ages, using the HeFTY software program (Ketcham, 2005) and radiation-damage-accumulation-annealing model of Guenthner et al. (2013). The FETKIN software package (Almendral et al., 2015), which uses sequential cross sections constructed with MOVE (Midland Valley) and incorporates transient thermal effects and varying rock thermal properties, was then used to model T-t paths and expected ZHe ages across the entire thrust sheet for a range of fault slip and erosion histories.

General geologic constraints on T-t paths include estimates of maximum temperature (T_{max}) at deeper levels, stratigraphic thicknesses, and characteristics of synorogenic strata that record unroofing. The western, lower part of the thrust sheet experienced T_{max} ~300–375 °C at depths of ~12 to 15 km, with an average geothermal gradient of ~25 °C/km, based on fluid inclusion data, greenschist-facies metamorphism, and widespread crystal plastic deformation of quartz (Condie, 1967; Yonkee et al., 1989, 2013). The eastern, lower part of the sheet experienced T_{max} ~150–200 °C at depths of ~8 to 10 km, with an average gradient of ~20 °C/km. Maximum stratigraphic depths were estimated from observed thicknesses of Neoproterozoic to Permian strata and an estimated thickness of ~4 km for Triassic to Middle Jurassic strata, followed by later Jurassic erosion prior to major thrusting. Aptian to Turonian (approximately 125–90 Ma) synorogenic strata in the foreland record progressive unroofing of lower Mesozoic to Paleozoic strata across the Willard-Paris-Meade sheet (DeCelles et al., 1993; Gentry et al., 2018). Paleogene strata that lie with angular unconformity over parts of the sheet provide a reference datum to estimate paleodepths at approximately 60–40 Ma (Rodgers & Janecke, 1992). These constraints, combined with inflection points at the top and bottom of steeper ZHe age-paleodepth gradients, were used to construct idealized T-t paths for the following stages: prethrust deposition of Middle Jurassic strata, later Jurassic erosion and development of a regional unconformity, synthrust Early to mid-Cretaceous cooling and exhumation during major fault slip, and postthrust exhumation during uplift of the Wasatch anticlinorium, followed by local deposition of flat-lying Paleogene strata.

The QTQt software package, which incorporates Markov chain Monte Carlo simulations to generate a series of T-t paths and corresponding expected ZHe ages (calculated with a simple Arrhenius relation), was used to evaluate the permissible range of thermal histories consistent with age-paleodepth relations for each transect. Two constraints were imposed on histories: an initial T range from 200 to 180 Ma based on maximum stratigraphic burial and a final T range from 60 to 40 Ma based on depth below Paleogene strata. Simulation algorithms in the QTQt package incorporate multiple sources of uncertainty, allow the thermal gradient to randomly vary between time steps, and provide a conservative (broad) range of permissible T-t paths.

Table 2
Parameter Ranges Used for FETKIN Thermo-Kinematic Models

1. Fault slip rate and thrust geometry
Slip rate cases:
(i) Constant slip rate of 1.5 km/Myr from 130 to 90 Ma (60-km total slip)
(ii) Constant slip rate of 2.4 km/Myr from 120 to 95 Ma
(iii) Variable slip rate of 1 km/Myr from 125 to 105 Ma, 3 km/Myr from 105 to 92 Ma
(iv) Limited Late Jurassic fault slip of 8 km, 1.5-km/Myr slip rate from 125 to 90 Ma
Thrust geometry based on Figure 3 with sequential restoration steps shown in Figure 11
2. Erosion
Prethrusting regional erosion of 1.5 km from 160 to 150 Ma. Synthrust erosion above 1 to 2° topographic slope across the thrust sheet adjusted for flexural loading
3. Boundary conditions
Basal temperature at 26-km depth (T_b) cases:
(i) Constant T_b with values ranging from 500 to 650 °C
(ii) Variable T_b of 550 and 600 °C in eastern and western parts of section, respectively
Fixed surface temperature of $T_0 = 20$ °C
No heat flow across side boundaries of model
4. Thermal properties
Thermal conductivity (k) cases:
(i) Homogeneous $k = 2.5$ W/m·K
(ii) Heterogeneous $k = 2$, 2.5, 3, and 4 W/m·K, respectively, for slate, mixed rock type, carbonate-rich, and quartzite-rich intervals in the Willard sheet and footwall
Rock density = 2,700 kg/m^3, specific heat capacity = 1,000 J/kg K, no internal heat production
5. Initial conditions
Steady-state conductive geotherm at 160 Ma for given $T_{b,26\text{km}}$ and thermal conductivity (k) structure. Examples of initial heat flow (q_0) and geothermal gradients (dT/dz) indicated below:
(i) $T_{b,26\ \text{km}} = 550$ °C and homogeneous $k = 2.5$ W/m·K, with $q_0 \approx 50$ mW/m^2 and $dT/dz \approx 20$ °C/km
(ii) $T_{b,26\ \text{km}} = 550$ °C and heterogeneous k, with $q_0 \approx 55$ mW/m^2 and $dT/dz \approx 22$, 18, and 14 °C/km in intervals with $k = 2.5$, 3, and 4 W/m·K, respectively
(iii) $T_{b,26\ \text{km}} = 650$ °C and heterogeneous k, with $q_0 \approx 65$ mW/m^2 and $dT/dz \approx 26$, 22, and 16 °C/km in intervals with $k = 2.5$, 3, and 4 W/m·K, respectively

Emplacement of large thrust sheets causes transient thermal changes due to advective transport of heat and rock. Additionally, thermal conductivity varies between micaceous, carbonate, and quartz-rich strata, and heat flow may vary laterally, leading to additional complexities. The FETKIN software package (Almendral et al., 2015), which solves the transient diffusion-advection heat equation with rock velocity fields determined from sequentially restored cross sections, was used to calculate thermo-kinematic models for a range of parameters, including varying fault slip rate, different basal temperature boundary conditions, and varying rock thermal properties (Table 2). Erosion was based on a uniform topographic slope across the Willard sheet and unroofing levels recorded by synorogenic strata (Gentry et al., 2018). For each model, predicted ZHe ages were calculated using output *T*-*t* paths and the Arrhenius relation of Reiners et al. (2004), and then compared with observed ZHe ages to evaluate what combinations of fault slip rate, basal temperature, and thermal properties best matched available data.

4. Thermochronometric Data and Results

4.1. Monte Cristo Transect

The Monte Cristo paleodepth transect lies within the eastern part of the sheet and contains a west dipping panel of thinner Neoproterozoic to Pennsylvanian strata above the frontal ramp of the Willard thrust, with imbricated Triassic to Middle Jurassic strata exposed in the footwall (Figure 3). The panel is unconformably capped by flat-lying Paleogene strata (Coogan & King, 2016). The sampling transect spans Upper Cambrian to Neoproterozoic strata, with estimated maximum stratigraphic burial depths of $z_{\text{ms}} = 7.4$ to 9.3 km, based on a 4-km thickness of Triassic to Jurassic strata (Figure 6). A shallow sample (CAT-09 from the Worm Creek Member at $z_{\text{ms}} = 7.4$ km) has a mean ZHe age of 166 ± 18 Ma. Three underlying samples (WT-21, WT-20, and WT-19 from the upper Geertsen Canyon to Browns Hole Formations at $z_{\text{ms}} = 8.3$, 8.6, and 9.0 km, respectively) have mean ZHe ages of 160 ± 18, 156 ± 17, and 160 ± 10 Ma. Two slightly deeper samples (WT-17 and WT-18 from Neoproterozoic quartzite at $z_{\text{ms}} = 9.3$ km) have a pooled mean ZHe age of 159 ± 18 Ma. Most zircon grains in this area have ZHe ages of approximately 140–180 Ma, with outlier grains having older ages likely related to He inheritance, indicating that samples were

located in the lower part of the PRZ during mid-Jurassic maximum burial. The later Jurassic ZHe ages are interpreted to record cooling during regional erosion prior to onset of major thrusting, or alternatively the ages could record an early phase of limited thrust slip, synchronous with early shortening in the hinterland of western Utah (Allmendinger & Jordan, 1984; Miller et al., 1997).

Three samples were run for ZFT analysis. Samples CAT-09 and CAT-10 (located southward) from the Worm Creek Member have ZFT grain ages mostly from 200 to 400 Ma, which are younger than approximately 500-Ma U-Pb ages for many grains in this unit, indicating that these samples entered the PAZ (Figure 6). CAT-09 has five less retentive grains with a mean ZFT age of 156 ± 15 Ma. CAT-25 from the Geertsen Canyon Formation has ZFT grain ages mostly from 200 to 600 Ma, which are younger than 1.7–1.8-Ga U-Pb ages for most grains in this unit, also indicating that the sample entered the PAZ. This sample contains one younger grain with a Jurassic ZFT age.

Idealized *T*-*t* paths for the Worm Creek and Browns Hole samples at maximum depths of z_{ms} = 7.4 and 9.0 km, respectively, have *T* ~170 and 200 °C during mid-Jurassic burial (using a thermal gradient of 20 °C/km), followed by 1.5 km of Late Jurassic erosion, and 4 km of exhumation during major slip on the Willard thrust (Figure 6b). Samples, however, only cover a limited depth range (<2 km), and thus, the amounts of Late Jurassic erosion and exhumation during major thrust slip are poorly constrained. Slow exhumation during the later Cretaceous brought samples near the surface, followed by deposition of flat-lying Paleogene strata.

The general range of *T*-*t* paths consistent with ZHe ages was evaluated using the QTQt software package. An initial *T* range of 120–160 °C at 180–200 Ma was assigned to sample CAT-09 that reached the PRZ during mid-Jurassic maximum burial, with a final *T* range of 40–60 °C at 40–60 Ma used to simulate shallow depths during the Paleogene. Permissible *T*-*t* paths show overall Late Jurassic to Cretaceous cooling (Figure 6c) but do not closely constrain the thermal history due to the limited depth range of samples.

Relations between ZHe ages, U-Th (eU) contents, and U-Pb ages of grains were further evaluated for a range of thermal histories using the HeFTY software program (Figure 6d; Ketcham, 2005). Grain data for samples WT-21, WT-20, WT-19, WT-18, and WT-17 were pooled to provide a wider range of ZHe-eU values to compare with models. Key observations include the following: most ZHe grain ages are 180–140 Ma; ZHe grain ages increase overall as eU increases from ~30 to 100 ppm, with ages of >200 Ma for more retentive grains; and most grains have 1.3–1.0- or 1.8–1.6-Ga U-Pb ages for basement sources. The preferred thermal history has slow burial from 550 to 200 Ma, rapid mid-Jurassic burial with T_{max} = 190 °C at 160 Ma, 30 °C of cooling during Late Jurassic erosion, and 80 °C of cooling from 125 to 90 Ma during Willard thrusting. Most observed grain ZHe-eU values lie within the composite envelope for this history. Thermal histories with T_{max} >200 °C predict low-amplitude inheritance envelopes, inconsistent with >200-Ma ZHe ages for more retentive grains. Thermal histories with onset of cooling at 125 Ma (i.e., lack Late Jurassic erosion) predict envelopes with Early Cretaceous ZHe grain ages along their lower parts, inconsistent with the abundance of 180–140-Ma grains. Detailed relations among ZHe age, eU, U-Pb age, and grain size, however, depart from model predictions, indicating additional sources of ZHe dispersion.

4.2. Bear River Range Transect

The Bear River Range paleodepth transect lies within the central part of the Willard thrust sheet and exposes Neoproterozoic to Pennsylvanian strata along the NNE plunging Browns Hole anticline and Logan Peak syncline that lies in the footwall of the Providence thrust (Figure 3; Coogan & King, 2016; Dover, 1995). These folded strata are locally capped with angular unconformity by flat-lying Eocene strata. The sample transect spans Devonian to Neoproterozoic strata with estimated mid-Jurassic maximum stratigraphic depths of z_{ms} = 7.1 to 12.0 km, based on a 4-km thickness of Triassic to Middle Jurassic strata (Figure 7). The shallowest sample (WT-06 from Devonian strata at z_{ms} = 7.1 km) has a poorly defined mean ZHe age of 172 ± 27 Ma with wide dispersion of grain ages, indicating that it was located within the PRZ during mid-Jurassic burial. A second sample (WT-05) of Devonian strata collected in the footwall of the Providence thrust experienced an estimated additional ~1.5 km of tectonic burial and has a younger mean age of 121 ± 28 Ma. Mean ZHe ages for other samples decrease systematically with depth. A sample from the Worm Creek Member (WT-03 at z_{ms} = 8.2 km) has a mean age of 127 ± 5 Ma along with one older grain. Middle-level samples (WT-26 and WT-24 from the upper Geertsen Canyon Formation and Browns Hole Formation at z_{ms} = 9.3 and 10.4 km, respectively) have mean ages of 112 ± 8 and 109 ± 9 Ma. Underlying

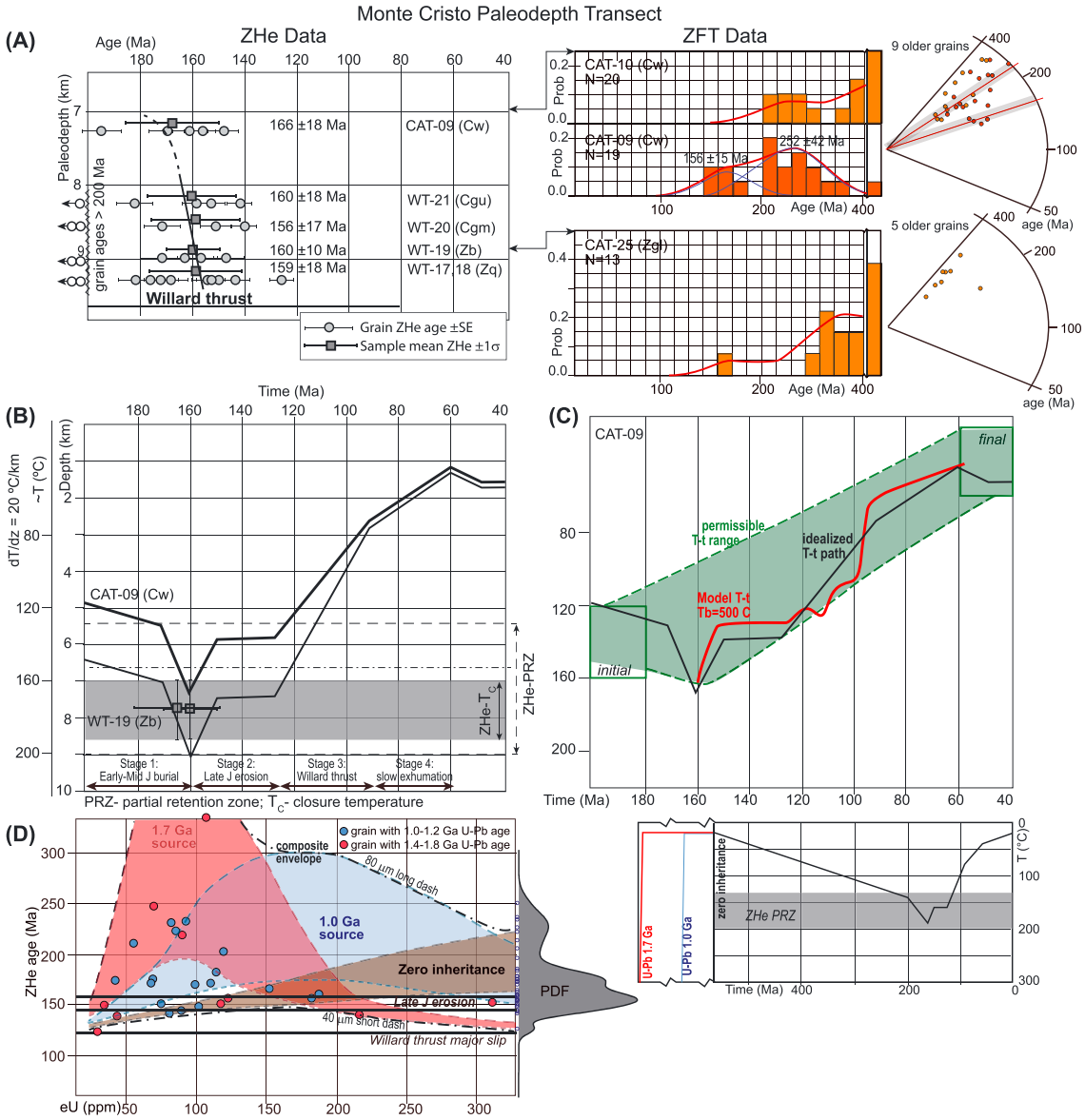

Figure 6. Thermochronometric data for the Monte Cristo transect. (a) ZHe ages versus paleodepth of samples on left. Squares are sample mean ZHe ages with 1σ error bars. Small gray circles are individual grain ages, and open circles are outlier grains. Histogram and radial plots of ZFT grain ages on right. Probability density (red line) and binomial fits of subgroups (blue line) shown on histograms. (b) Idealized *T-t* paths for upper and lower samples (CAT-09, WT-19), constructed for a fixed thermal gradient of 20 °C/km, 1.5 km of Late Jurassic erosion, enhanced exhumation during Willard thrusting, and later slower exhumation. (c) Permissible range of thermal histories (green shade) for sample CAT-09, based on QTQt simulations for indicated initial and final *T* values (boxes). The idealized *T-t* path and preferred thermo-kinematic model path (red line) lie within this range. (d) ZHe-eU grain values and predicted inheritance envelopes for 1.7-Ga (red) and 1.0-Ga (blue) basement sources and grain sizes of 40–80 μm. ZHe-eU grain values lie within the composite envelope. Probability density function plot of ZHe ages shows abundant 180–140-Ma grains, plus outlier older grains.

samples (WT-28 and WT-29 from the Mutual and Caddy Canyon Formations at z_{ms} = 10.8 and 11.1 km, respectively) have statistically indistinguishable mean ages of 96 ± 10 and 100 ± 12 Ma. The deepest sample (CAT-05 from the Maple Canyon Formation at z_{ms} = 12.0 km) has a mean ZHe age of 78 ± 6 Ma. The systematic decrease in sample mean ages from approximately 125 to 95 Ma over a paleodepth range of ~8 to 12 km (or ~6.5 to 10.5 km after 1.5 km of inferred Late Jurassic erosion) is interpreted to record cooling during synthrusting exhumation as this part of the Willard sheet was transported up the western ramp and part of the eastern ramp. The younger ZHe age for the deepest sample (CAT-05) likely records subsequent cooling during erosion above the northern plunge of the Wasatch anticlinorium.

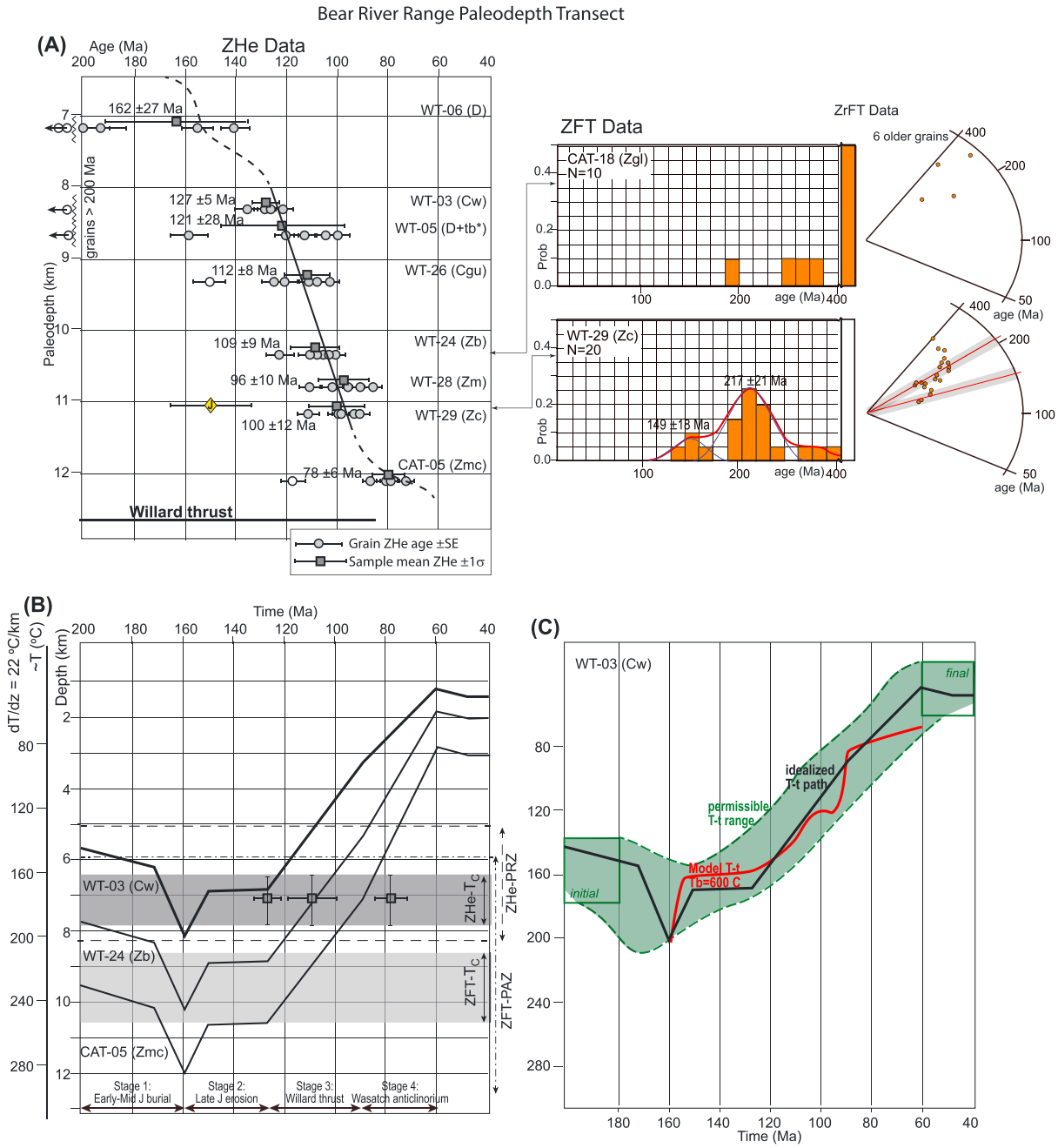

Figure 7. Thermochronometric data for the Bear River Range transect. (a) ZHe ages versus paleodepth of samples shown on left. Squares are sample mean ZHe ages with 1σ error bars, small gray circles are individual grain ages, and open circles are outlier grains. Histogram and radial plots of ZFT grain ages on right. Probability density (red) and binomial fits for subgroups (blue) shown on histograms. (b) Idealized *T-t* paths and ZHe ages for upper, middle, and lower samples (WT-03, WT-24, CAT-05), constructed for a fixed geothermal gradient of 22 °C/km, with 1.5 km of Late Jurassic erosion, enhanced exhumation during Willard thrusting, and erosion above the Wasatch anticlinorium. (c) Permissible range of thermal histories (green shade) for sample WT-03 based on QTQt simulations for indicated initial and final *T* values. The idealized *T-t* path and preferred thermo-kinematic model path (red line) lie within this range.

Two samples were run for ZFT analysis. A sample from the basal Geertsen Canyon Formation (CAT-18 at z_{ms} = 10.3 km) contains grains with ZFT ages mostly from 200 to 600 Ma that are younger than 1.7–1.8-Ga U-Pb ages, indicating that it entered the PAZ. A sample from Caddy Canyon Quartzite (WT-29 at z_{ms} = 11.1 km) has four younger grains with a mean ZFT age of 149 ± 18 Ma, and a group of grains with ages of 180–240 Ma, consistent with significant annealing of less retentive grains during mid-Jurassic maximum burial.

Idealized *T*-*t* paths for the Worm Creek, Browns Hole, and Maple Canyon samples at maximum depths of 8.2, 10.4, and 12.0 km, respectively, have *T* of ~200, 240, and 280 °C (using a thermal gradient of 22 °C/km), followed by ~1.5 km of Late Jurassic erosion and cooling, and by enhanced cooling from 125 to 90 Ma related to ~3.5 km of exhumation during major slip on the Willard thrust. Estimated later Cretaceous exhumation varies from ~1 km for the more northern Devonian sample to ~3.5 km for the more southern Maple Canyon sample uplifted above the north plunge of the Wasatch anticlinorium.

The general range of *T*-*t* paths consistent with ZHe ages (excluding sample WT-05 that experienced additional tectonic burial beneath the Providence thrust) was evaluated using the QTQt software package. An initial *T* range of 140–180 °C at 180–200 Ma was assigned to sample WT-03 that reached the base of the PRZ during mid-Jurassic burial, and a final *T* range of 40–60 °C at 40–60 Ma was used to simulate shallow depths during deposition of Paleogene strata. The permissible range of model *T*-*t* paths shows slight heating during the mid-Jurassic, minor Late Jurassic cooling, increased cooling (rates ~2 to 3 °C/Myr) from approximately 130 to 90 Ma, and continued cooling during the later Cretaceous (Figure 7c).

4.3. Wellsville Transect

The Wellsville paleodepth transect lies within the west-central part of the Willard sheet and contains a NE dipping panel of Neoproterozoic to Pennsylvanian strata above the Providence thrust (Figure 3). The panel initially dipped gently westward prior to Late Cretaceous northward tilting above the north plunge of the Wasatch anticlinorium and Neogene eastward tilting in the footwall of the Wasatch normal fault. The transect spans Mississippian to Neoproterozoic strata, and a thin slice of basement, with estimated mid-Jurassic maximum stratigraphic depths of z_{ms} = 7.5 to 14.8 km, based on a 4-km thickness of Triassic to Middle Jurassic strata (Figure 8). Three shallower samples in Mississippian, Devonian, and Ordovician strata (WT-62, WT-35, and WT-38 at z_{ms} = 7.5, 8.1, and 8.8 km, respectively) have mean ZHe ages of 121 ± 10, 129 ± 14, and 129 ± 11 Ma. These samples are interpreted to have been located near the base of the PRZ prior to major thrusting, and to record early cooling above the western ramp. Analyzed grains from the Mississippian sample had younger U-Pb basement source ages of 500–400 Ma, minimizing prior He inheritance. Samples collected from the Worm Creek Member did not yield zircon grains of sufficiently large size for ZHe analysis. Middle level samples (WT-16 and WT-30 from the upper Geertsen Canyon and Browns Hole Formations at z_{ms} = 10.9 and 12.0 km, respectively) have mean ZHe ages of 104 ± 15 and 97 ± 6 Ma. Underlying samples (WT-31 and WT-32 from the Mutual and Caddy Canyon Formations at z_{ms} = 12.5 and 12.9 km, respectively) have statistically indistinguishable mean ages of 87 ± 10 and 88 ± 17 Ma. The decrease in age from approximately 125 to 90 Ma over a paleodepth range of ~7.5 to 13 km (or ~6 to 11.5 km after 1.5 km of inferred Late Jurassic erosion) is interpreted to record cooling and exhumation as this part of the sheet was transported above the western Willard ramp and imbricate Providence thrust. Deeper samples (WT-63 from the Perry Canyon Formation at z_{ms} = 14.4 km and WT-37 from basement of the Facer Formation at z_t = 14.8 km) have mean ZHe ages of 71 ± 8 and 63 ± 4 Ma, respectively. These ages likely record younger cooling during uplift of the Wasatch anticlinorium. The structurally deepest sample (WT-47), located in the footwall of the Providence imbricate thrust, experienced additional tectonic burial and has a younger ZHe age of 24 ± 6 Ma, indicating that it remained below the PRZ or was buried beneath Paleogene strata prior to Neogene extension.

Five samples were run for ZFT analysis. A sample from the upper Geertsen Canyon Formation (WT-16 at z_{ms} = 10.9 km) has a young subgroup of ten grains with a mean ZFT age of 121 ± 16 Ma that likely records cooling during early thrusting, and seven more retentive grains with Jurassic ages. A sample from the basal Geertsen Canyon Formation (CAT-11 at z_{ms} = 11.9 km) has a young subgroup of 11 grains with a mean age of 105 ± 9 Ma that records continued thrust-related cooling, along with seven partially annealed grains with a mean age of 160 ± 18 Ma. The sample from the Caddy Canyon Quartzite (WT-32 at z_{ms} = 12.9 km) has all young grains with a mean age of 102 ± 15 Ma, and the Perry Canyon sample (WT-63 at z_{ms} = 14.4 km) also has all young grains with a mean age of 72 ± 7 Ma. ZFT ages of the youngest grain subgroups are slightly older than ZHe ages for a given sample. The deepest sample located to the southeast below the Providence imbricate thrust (WT-47) has a mean ZFT age of 74 ± 8 Ma.

Idealized *T*-*t* paths for the Devonian, Browns Hole, and Perry Canyon samples at maximum depths of 8.1, 12.0, and 14.4 km, respectively, have *T* of ~210, 300, and 360 °C (using a thermal gradient of 24 °C/km),

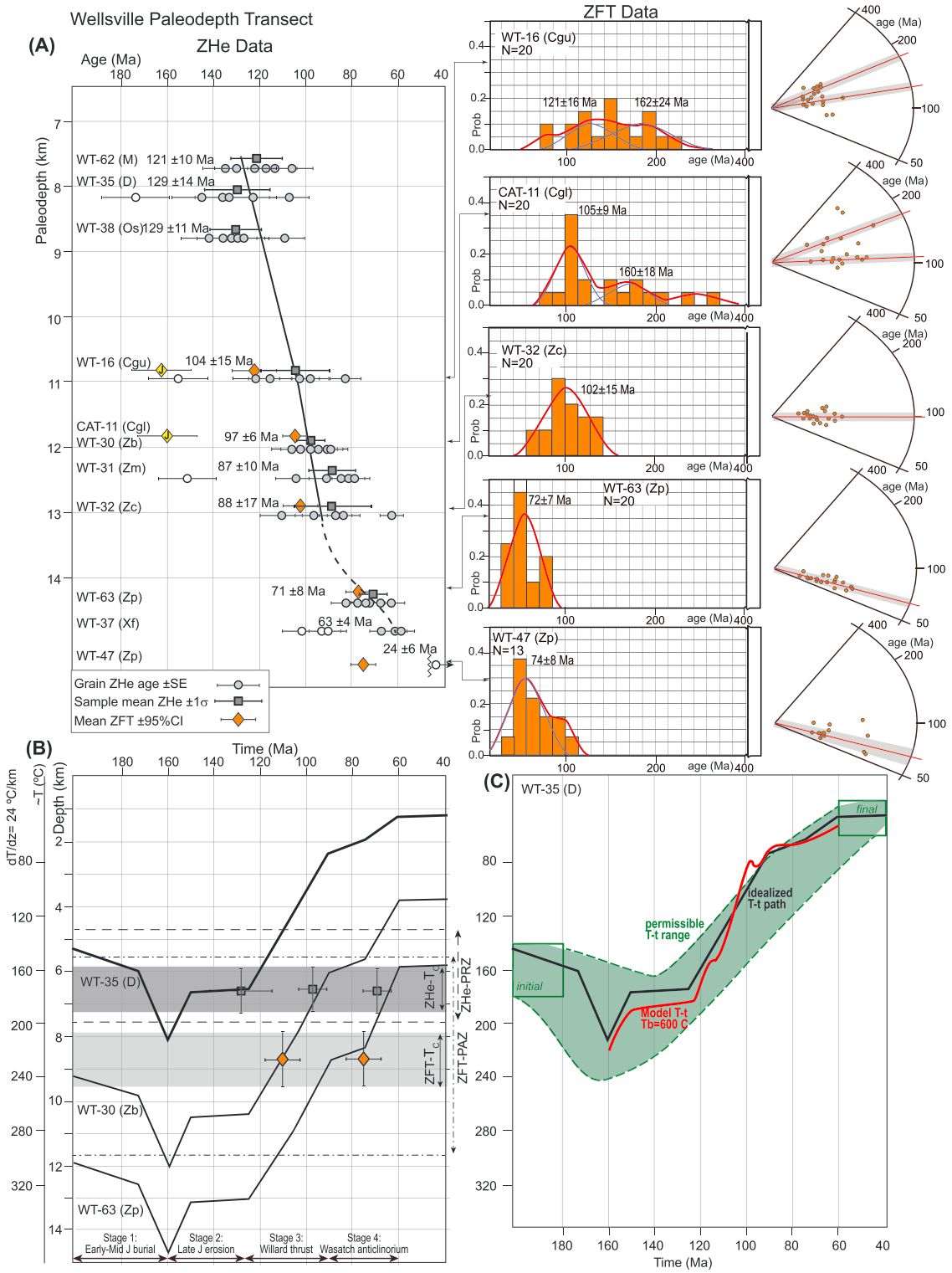

Figure 8. Thermochronometric data for the Wellsville transect. (a) ZHe age versus paleodepth of samples shown on left. Squares are sample mean ZHe ages with 1σ error bars. Small gray circles are individual grain ZHe ages, and open circles are outlier grains. Sample mean ZFT ages (J indicates Jurassic subgroup) are also shown. Histogram and radial plots of ZFT grain ages on right. Probability density (red) and binomial fits for subgroups (blue) are shown on histograms. (b) Idealized *T-t* paths and mean ZHe and ZFT ages for upper, middle, and lower samples (WT-35, WT-30, and WT-63), constructed for fixed geothermal gradient of 24 °C/km, Late Jurassic erosion, enhanced exhumation during Willard thrusting, and later erosion above the Wasatch anticlinorium. (c) Permissible range of thermal histories (green shade) for sample WT-35 based on QTQt simulations for indicated initial and final *T* values. The idealized *T-t* path and preferred thermo-kinematic model path (red line) lie within this range.

followed by ~1.5 km of Late Jurassic erosion and cooling, followed by enhanced cooling from approximately 125 to 90 Ma during ~4.5 km of exhumation related to major slip on the Willard and Providence thrusts. In detail, cooling rates appear faster from approximately 105 to 95 Ma. Later Cretaceous exhumation varies from 1 km for the more northern Devonian sample to 3 km for southern samples that were uplifted along the north plunge of the Wasatch anticlinorium.

The general range of *T-t* paths consistent with ZHe ages (excluding sample WT-47 that experienced additional tectonic burial beneath the Providence thrust) was evaluated using the QTQt software package. An initial *T* range of 140–180 °C at 180–200 Ma was assigned to sample WT-35 (Devonian level) that reached the base of the PRZ prior to thrusting, and a final *T* range of 40–60 °C at 40–60 Ma was used to simulate shallow depths during deposition of Paleogene wedge-top strata. The permissible range of model thermal histories shows slight heating during the Early to mid-Jurassic, increased cooling (rates ~2 to 3 °C/Myr) from approximately 130 to 90 Ma, and continued cooling during the later Cretaceous (Figure 8c). The age for onset of major thrusting is only broadly bracketed for this transect, partly due to lack of an inflection in ZHe age-depth relations as all samples were located below the fossil PRZ at onset of cooling.

4.4. Promontory Transect

The Promontory paleodepth transect lies within the western part of the Willard sheet and contains a panel of gently dipping Neoproterozoic to Pennsylvanian strata, with the deepest levels exposed to the southeast on Fremont Island (Figure 3). The panel was tilted gently northward during Late Cretaceous growth of the Wasatch anticlinorium and underwent Neogene eastward tilting in the footwall of the East Great Salt Lake normal fault. The transect spans Devonian to Neoproterozoic strata with estimated prethrusting depths of z_{ms} = 8.2 to 15.0 km, based on a 4-km thickness of Triassic to Middle Jurassic strata (Figure 9). Two upper level samples in Devonian and Ordovician strata (WT-65 and WT-64 at z_{ms} = 8.5 and 9.4 km, respectively) have mean ZHe ages of 126 ± 16 and 109 ± 16 Ma. These samples were likely located near the base of the ZHe PRZ prior to thrusting and record early cooling of this part of the sheet started up the western ramp. An underlying sample (WT-66 from the Worm Creek Member at z_{ms} = 10.3 km) has a mean age of 92 ± 8 Ma. Two middle-level samples (WT-56 and CAT-23 from the upper and basal parts of the Geertsen Canyon Formation at z_{ms} = 11.5 and 12.6 km, respectively) have mean ZHe ages of 89 ± 14 and 88 ± 10 Ma. Underlying samples (WT-55 and WT-53 from the Mutual and Caddy Canyon formations at z_{ms} = 13.0 and 13.7 km, respectively) have ages of 92 ± 10 and 77 ± 8 Ma. The decrease in age from approximately 125 to 90 Ma over a paleodepth range of ~8 to 13 or ~6.5 to 11. 5 km after 1.5 km of inferred Late Jurassic erosion) is interpreted to record synthrusting exhumation and cooling as this part of the Willard sheet was transported up the western ramp. Deeper samples (WT-52 from the Kelley Canyon Formation at z_{ms} = 14.3 km and EAB-11 from the Perry Canyon Formation on Fremont Island at z_{ms} = 15.0 km) have mean ZHe ages of 54 ± 4 and 68 ± 5 Ma, respectively, related to younger parts of the cooling history. The Perry Canyon sample likely records cooling during uplift of the Wasatch anticlinorium, whereas the Kelley Canyon sample was located farther northwest where uplift of the anticlinorium was less and cooling through the PRZ occurred later.

Five samples were run for ZFT analysis. The sample from the Worm Creek Member (WT-66 at z_{ms} = 10.3 km) has a young subgroup of seven grains with a mean age of 108 ± 17 Ma that records cooling during thrusting, and 10 more retentive grains with ages of 140–200 Ma. Samples from the upper and basal parts of the Geertsen Canyon Formation (WT-56 and CAT-23 at z_{ms} = 11.5 and 12.6 km) have grain age groups with mean ages of 106 ± 14 and 100 ± 15 Ma, respectively, along with a few younger grains. The sample from the Caddy Canyon Quartzite (WT-53 at z_{ms} = 13.7 km) has young grains with a mean age of 82 ± 11 Ma, and a Perry Canyon sample from nearby Little Mountain (WT-49 at z_{ms} = 15.0 km) also has young grains with a mean age of 77 ± 11 Ma.

Idealized *T-t* paths for the Devonian, basal Geertsen Canyon, and Perry Canyon samples at maximum depths of 8.5, 12.6, and 15.0 km, respectively, have T_{max} of ~220, 310, and 370 °C (using a thermal gradient of 24 °C/km), followed by 1.5 km of later Jurassic erosion and by enhanced cooling from approximately 120 to 90 Ma related to ~4.5 km of exhumation as the Willard sheet was transported up the western ramp. In detail, cooling rates were faster from approximately 100 to 90 Ma. Estimated later Cretaceous exhumation

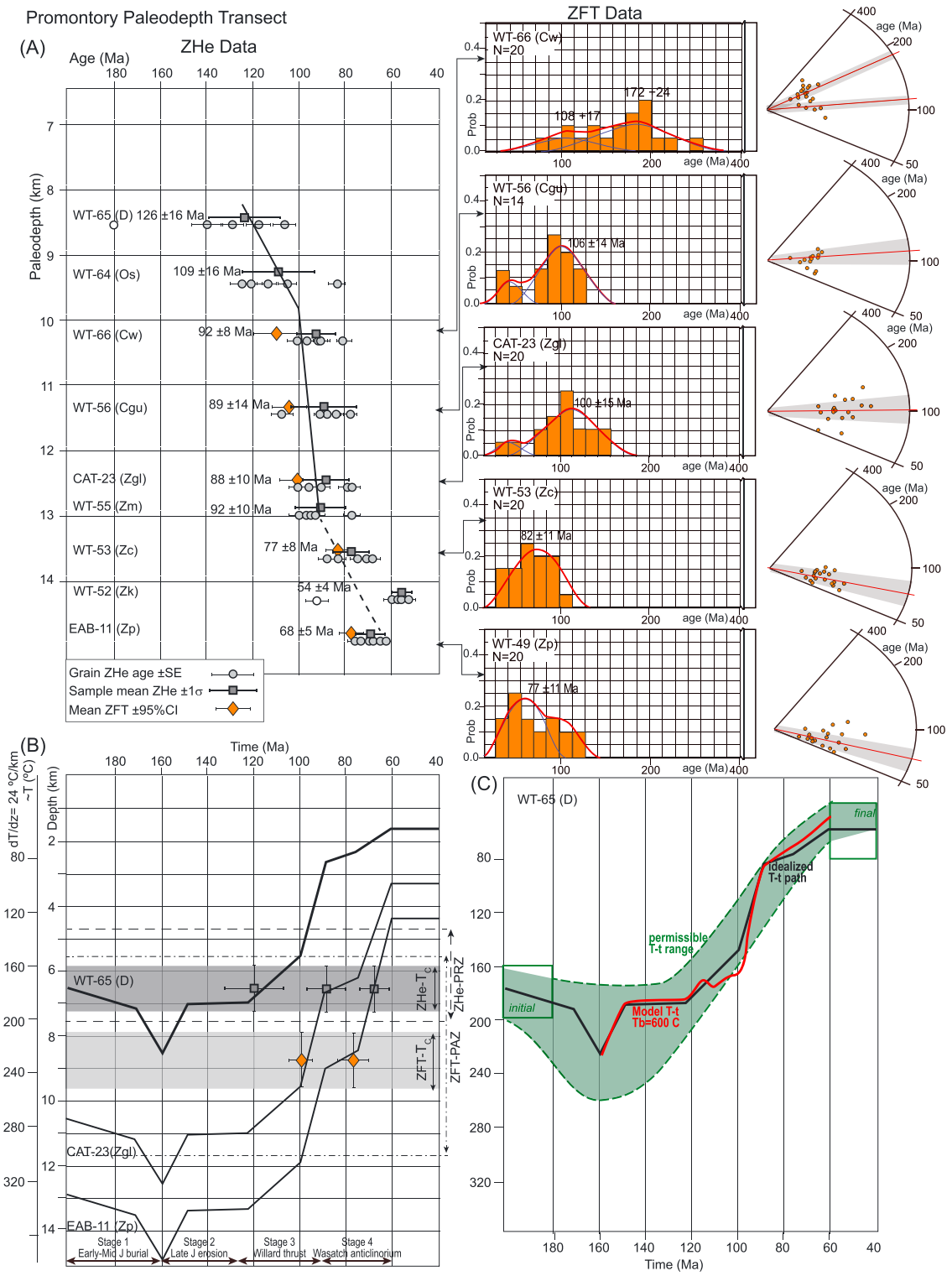

Figure 9. Thermochronometric data for the Promontory transect. (a) ZHe ages versus paleodepth of samples shown on left. Squares are sample mean ZHe ages with 1σ error bars. Small gray circles are individual grain ages, and open circles are outlier grains. Sample mean ZFT ages also shown. Histogram and radial plots of ZFT grain ages on right. Probability density (red) and binomial fits for subgroups (blue) shown on histograms. (b) Idealized *T-t* paths and mean ZHe and ZFT ages for upper, middle, and lower samples (WT-65, CAT-23, and EAB-11), constructed for a fixed geothermal gradient of 24 °C/km, 1.5 km of Late Jurassic erosion, enhanced exhumation during Willard thrusting, and later erosion above the Wasatch anticlinorium. (c) Permissible range of thermal histories (green shade) for sample WT-65 based on QTQt simulations for indicated initial and final *T* values. The idealized *T-t* path and preferred thermo-kinematic model path (red line) for WT-65 lie within this range.

varies from ~1 km for the Devonian sample to the north to 4 km for deeper samples on Fremont Island located along the north plunge of the underlying Wasatch anticlinorium, consistent with approximately 80–65-Ma ZFT ages for deeper samples.

The general range of *T*-*t* paths consistent with ZHe ages (excluding sample WT-52) was evaluated using the QTQt software package. An initial *T* range of 160–200 °C at 180–200 Ma was assigned to the sample WT-65, and a final *T* range of 40–80 °C at 40–60 Ma was used to simulate shallow depths during the Paleogene. The permissible range of thermal histories shows slight heating during the Early to mid-Jurassic, overall moderate cooling (rates of ~2 °C/Myr) from approximately 130 to 90 Ma, and continued cooling during the later Cretaceous (Figure 9c). Timing for onset of Willard thrusting is only broadly constrained, partly due to uncertainties in cooling ages of individual samples. Although QTQt simulations only provide broad constraints for each transect, the combination of 130–120-Ma ZHe ages for shallower samples on multiple transects brackets start of major slip on the Willard thrust.

4.5. Stratigraphic-Parallel Traverses

Traverses along the Worm Creek, Browns Hole, and Perry Canyon stratigraphic units were sampled to evaluate lateral variations in cooling ages related to progressive transport of the sheet upthrust ramps (Figure 10). Horizontal distances were measured eastward from the Promontory area on a fully restored cross section of the Willard sheet (Figure 11a). Paleodepths increased westward along each stratigraphic unit, reflecting the westward thickening of Neoproterozoic to Paleozoic strata in the Willard sheet.

The Worm Creek traverse includes five samples at upper levels that span a restored W-E distance of 5 to 63 km across the Willard sheet. Sample mean ZHe ages decrease overall westward, from 166 ± 18 Ma (CAT-09) in the eastern part of the sheet to 127 ± 5 Ma (WT-03), 113 ± 26 Ma (WT-41), and 111 ± 15 Ma (WT-40) in central parts of the sheet (distances of 42, 30, and 26 km, respectively), to 92 ± 8 Ma (WT-66) in the western part of the sheet (Figure 10a). Decreasing ages from approximately 130 to 90 Ma for central to western samples are consistent with progressive eastward transport of the thrust sheet up the western ramp. The eastern sample (CAT-09) was at the shallowest level and records later Jurassic erosion prior to major thrusting.

The Browns Hole (and overlying basal Geertsen Canyon) traverse includes 10 samples at middle levels that span a palinspastically restored W-E distance of 3 to 66 km across the Willard sheet. Sample mean ZHe ages decrease overall westward, from 160 ± 10 Ma (WT-19) in the eastern part of the sheet to 119 ± 20 Ma (CD-59) and 109 ± 9 Ma (WT-24) in the east-central part (distances of 48 and 42 km); to 106 ± 15 Ma (CAT-15), 112 ± 13 Ma (WT-46), and 97 ± 6 Ma (WT-30) in the west-central part (distances of 31, 26, and 20 km); and to 88 ± 10 Ma (CAT-23) in the western part (Figure 10b). Age-distance relations along this traverse are consistent with protracted transport of the Willard sheet upthrust ramps from approximately 125 to 90 Ma. Samples in eastern to east-central parts of the sheet (CAT-25 and CAT-18) contain grains with older ZFT ages (mostly >200 Ma), indicating that they were only partly reset. In the west-central part of the sheet, grain subgroups with Jurassic to Early Cretaceous ages become better developed. Sample CAT-15 (distance of 30 km) has three grains with approximately 150-Ma ages, along with mostly 200–300-Ma age grains that were only partly reset during mid-Jurassic maximum burial. Sample CAT-02 (distance of 26 km) contains two subgroups with mean ages of 123 ± 7 and 146 ± 7 Ma, and sample WT-46 (distance of 26 km) has similar subgroups with mean ages of 114 ± 11 and 161 ± 14 Ma. Sample CAT-11 (distance of 20 km) has a greater proportion of young grains with a mean ZFT age of 105 ± 9 Ma, and sample CAT-23 in the western part of the sheet has young grains with a mean ZFT age of 100 ± 15 Ma.

The Perry Canyon traverse includes five samples from lower levels of the Willard sheet that span restored horizontal distances from ~6 to 40 km; this level is absent in the eastern part of the sheet. Mean ZHe ages range from 68 ± 5 Ma for EAB-11 and 67 ± 5 Ma for WT-49 in the western part of the sheet to 71 ± 8 Ma for WT-63 in the west-central part, to 70 ± 15 Ma for WT-43 in the central part (Figure 10c), recording younger cooling during growth of the Wasatch anticlinorium that uplifted the southern Willard sheet. ZFT ages are slightly older, ranging from 77 ± 11 and 72 ± 7 Ma for WT-63 and WT-49 that record cooling during early uplift of the Wasatch anticlinorium to 103 ± 18 and 101 ± 10 Ma for WT-43 and CAT-04 that are located farther east and record cooling during Willard thrusting.

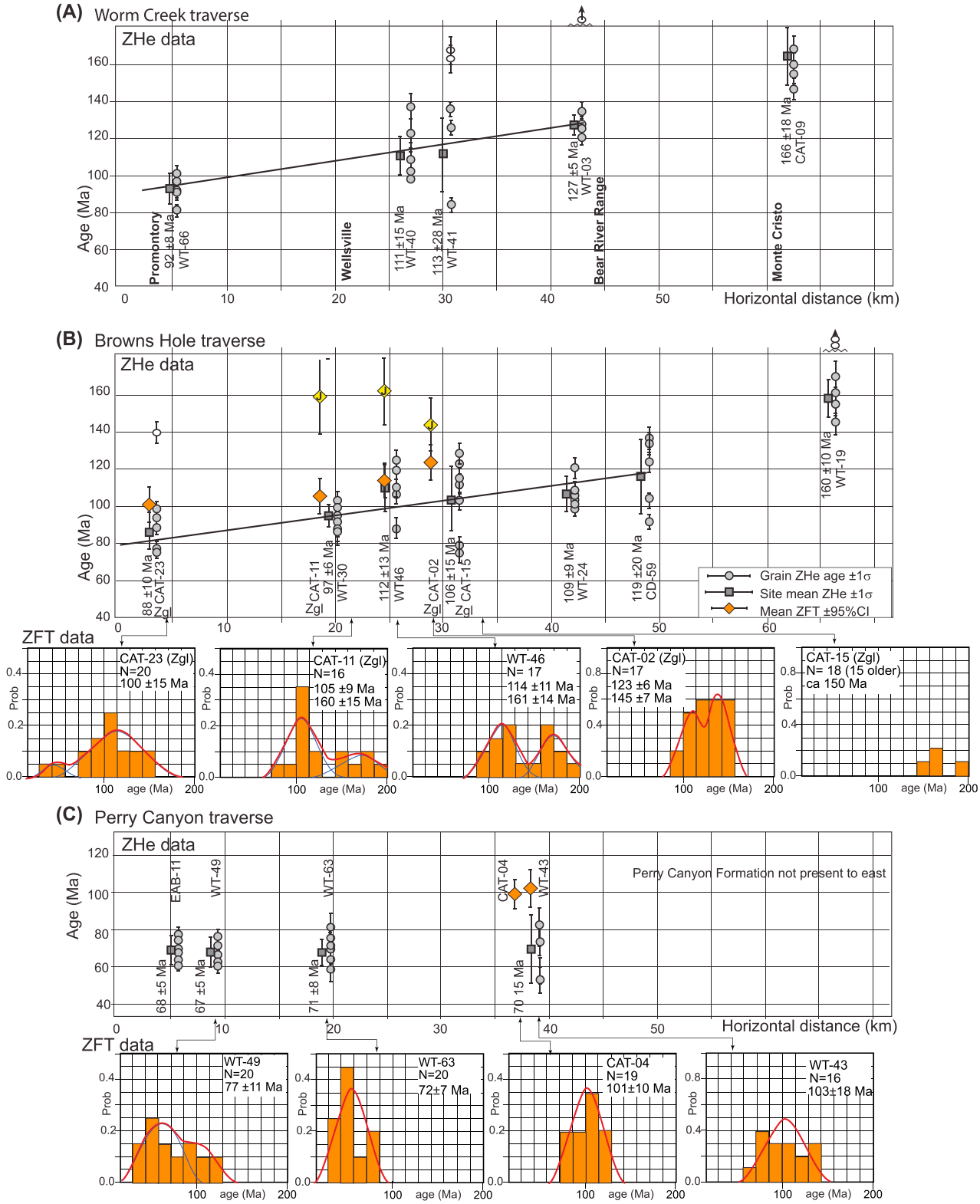

Figure 10. Thermochronometric data for (a) Worm Creek, (b) Browns Hole, and (c) Perry Canyon stratigraphic traverses. ZHe age versus restored horizontal distance of samples shown on the top plot for each traverse. Squares are sample mean ZHe ages with 1σ error bars, small gray circles are individual grain ages, and open circles are outlier grains. Sample mean ZFT ages (diamonds, "J" indicates Jurassic age subgroup) are also shown. ZFT grain age data are shown on lower histograms for the Browns Hole and Perry Canyon traverses. Probability density (red) and binomial fits for subgroups (blue) are indicated on histograms. The Browns Hole traverse also includes samples from the immediately overlying basal Geertsen Canyon Formation (Zgl).

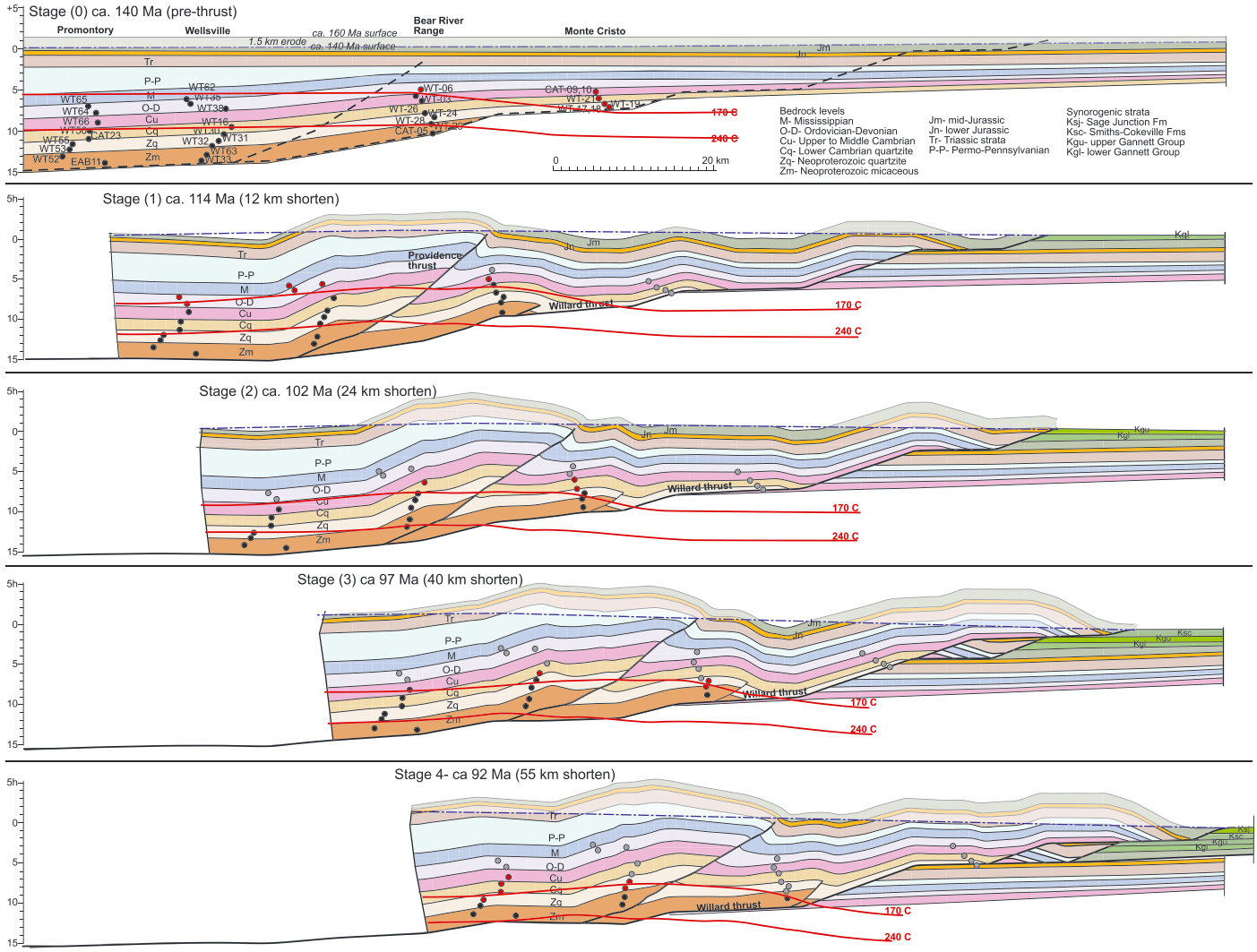

Figure 11. Palinspastically restored cross sections of Willard sheet for indicated time and net slip steps show restored sample positions (red color indicates that sample has ZHe age within that time step) and positions of 180 °C and 240 °C isotherms for the preferred thermal model. Sections are shown for primary sedimentary wedge and after 12, 24, 40, and 55 km of thrust slip.

5. Thermo-Kinematic Models

Thermo-kinematic modeling using FETKIN (Almendral et al., 2015) was completed to evaluate what combinations of thrust sheet geometry, fault slip history, rock thermal properties, and heat flow best matched thermochronometric data from the four paleodepth transects and the Browns Hole stratigraphic-parallel traverse. The composite down-plunge section of the Willard sheet in Figure 3b was used to construct 12 sequentially restored cross sections using Move software, beginning with a prethrust section (Figure 11). The thrust-sheet geometry is overall well constrained, with ramp dips and locations having small uncertainties (roughly ±3° and ±5 km) related to ambiguities in restoring Neogene extension and projecting structural relations along the north plunge of the Wasatch anticlinorium. The age for onset of major thrust slip in thermal models ranged from 130 to 120 Ma, based on ZHe ages from upper structural levels in the western to central transects (Figures 7–9). Models also included 1.5 km of regional erosion from 160 to 150 Ma, with an alternative model having variable erosion during limited (8 km) later Jurassic thrust slip, based on ZHe ages for the Monte Cristo transect (Figure 6) and limited Jurassic ZFT ages at middle levels (Figure 10b). The following scenarios for major fault slip were modeled: (i) constant slip rate of 1.5 km/Myr from 130 to 90 Ma (total slip of 60 km); (ii) constant slip rate of 2.4 km/Myr from 120 to 95

Ma; and (iii) variable slip rate with 1.0 km/Myr from 125 to 105 Ma, increasing to 3.0 km/Myr from 105 to 92 Ma. Erosion during thrusting was modeled with a surface slope of 1 to 2° across the thrust sheet as adjusted for isostatic flexure, giving erosion rates of ~0.1 to 0.3 km/Myr and broadly matching unroofing relations recorded by synorogenic strata (Gentry et al., 2018). Thermal models were sensitive to a basal T (T_b) boundary condition and related heat flow (q), with a range of T_b = 500 to 650 °C at a depth of 26 km explored in models. Models were run for homogeneous thermal conductivity of k = 2.5 W/m·K, and for heterogeneous conductivity related to lithologic layering with k = 2, 2.5, 3, and 4 W/m·K for slate, mixed rock, carbonate, and quartzite intervals, respectively. The initial condition was a conductive steady-state geotherm for the given T_b and k values. For T_b of 550 and 650 °C, and homogeneous k = 2.5 W/m·K, the initial thermal gradient was ~20 and 24 °C/km, respectively, with corresponding q ~50 and 60 mW/m^2. Other boundary conditions included fixed surface T_0 = 20 °C and no lateral heat flow across the model sides. Ranges of parameters used in thermal models are summarized in Table 2. Misfit for each model was calculated by summing the absolute values of the predicted ZHe age minus the observed sample ZHe age. Model misfit was also evaluated from the number of samples for which predicted ages were inconsistent with observed cooling ages within an uncertainty of ±10 Ma.

The preferred thermal model, which minimizes misfit between predicted and observed ZHe ages, has regional Late Jurassic erosion, onset of major fault slip at 125 Ma with a variable slip rate increasing from 1 km/Myr during early slip to 3 km/Myr from 105 to 92 Ma, T_b of 600 to 550 °C decreasing from the western to eastern parts of the sheet, and heterogeneous thermal conductivity related to rock type (Figure 12). For this model, the average misfit between predicted and observed sample ZHe ages is 4 Ma, and nearly all model ages agree with observed ages within uncertainty. The preferred model successfully matches steeper age-paleodepth gradients from approximately 105 to 95 Ma and in quartzite intervals, higher maximum temperatures toward the west, and slightly younger ZHe ages for the Promontory transect initially located along the western flat. The preferred model is also consistent with most ZFT ages, using a closure temperature of ~210–250 °C for less retentive grains. ZFT grain ages, however, display wide dispersion at middle structural levels and closure temperatures of grains likely depend on varying radiation damage.

Thermal models with constant thrust slip rates have slightly larger misfits between predicted and observed ZHe ages for the Wellsville and Promontory transects, and along the Browns Hole traverse. Earlier onset of thrusting at 130 Ma with a constant slip rate of 1.5 km/Myr predicts slightly older ages compared to observed ZHe ages, but age-paleodepth relations still overlap within uncertainties of many samples. More complex slip histories with short (<5 Myr) pulses and lulls in fault slip are possible, but not resolvable with available thermochronometric data. A model with 8 km of Late Jurassic thrust slip was designed to test if approximately 160-Ma ZHe ages along the Monte Cristo transect could be related to an early phase of faulting. Although this model matched ZHe ages for the Monte Cristo transect, early fault slip resulted in older predicted ages compared to observed ZHe ages at upper levels of the Bear River transect located along the western ramp, and slightly younger ages for the Promontory transect along the western flat. However, given uncertainties in thicknesses of Triassic-Jurassic strata, limited early slip cannot be ruled out.

Thermal models with high-conductivity quartzite predict steeper ZHe age-paleodepth gradients across middle levels of the Willard sheet, as compared to models with homogeneous conductivity, consistent with observed cooling age patterns. Heterogeneous conductivity has two other consequences: (1) thermal gradients (dT/dz) vary, with lower gradients in higher k material, and (2) higher heat flow is required to obtain the same T_b if a high k interval is present. Consider two rock columns, column A with homogeneous k = 2.5 W/m·K and column B that contains a 4-km-thick quartzite interval with k = 4 W/m·K. For surface T_0 = 20 °C and T_b = 600 °C at 26-km depth, column A has dT/dz ~22 °C/km and q ~55 mW/m^2. For the same T_0 and T_b, column B has dT/dz ~15 and 24 °C/km in quartzite and other rock intervals, respectively, and higher q ~60 mW/m^2.

No single value of T_b matches observed age-paleodepth relations along all paleodepth transects. For the western Promontory and Wellsville transects, models with T_b = 600 °C and heterogeneous k, corresponding to an initial heat flow of ~60 mW/m^2, have better fits, whereas models with cooler T_b predict deeper levels for the PRZ and too old of ZHe ages for shallower samples. For the eastern Monte Cristo transect, models with T_b = 550 °C and heterogeneous k, corresponding to a heat flow of ~55 mW/m^2, have better fits

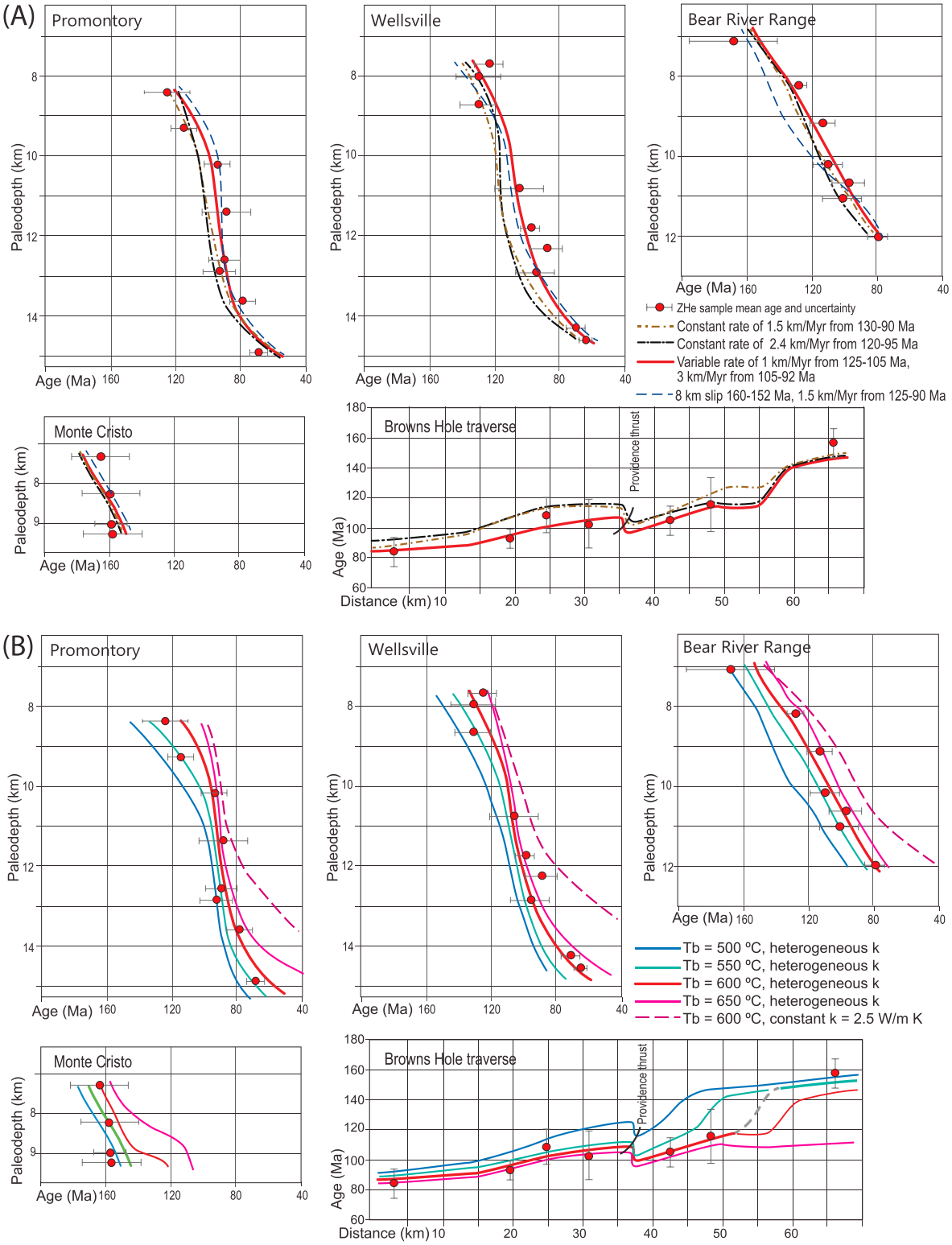

Figure 12. Results of FETKIN thermo-kinematic models show predicted ZHe age-paleodepth relations for structural transects and age-distance relations for the Browns Hole traverse, along with observed ZHe sample ages (red circles with ~95% confidence intervals). (a) Predicted ZHe age relations for different fault slip histories, with $T_b = 550$ and 600 °C in eastern and western parts of sheet, and heterogeneous thermal conductivity. The variable slip rate model (thick red line) best matches observed ZHe ages. (b) Predicted ZHe age relations for different T_b ranging from 500 to 650 °C and heterogeneous thermal conductivity (k), and for homogeneous k (dashed line), with variable fault slip rate. A model that combines heterogeneous k, $T_b = 550$, and 600 °C in eastern and western parts of sheet, and variable slip rate best fits observed ZHe ages.

compared to models with warmer T_b that predict too young of ZHe ages. Increases in T_b and q toward the west are consistent with geologic constraints on maximum temperatures, and with transition from more eastern cratonic to western passive margin settings. Estimated thicknesses of Triassic to Jurassic strata that have been mostly eroded across the Willard sheet, however, have uncertainties and presence of initially thicker sections, combined with lower average thermal gradients and heat flow, can match ZHe ages of shallower samples.

6. Discussion

ZHe and ZFT thermochronometric data along paleodepth transects and across stratigraphic traverses, combined with thermo-kinematic modeling, provide key constraints for the emplacement history of the areally extensive, far-travelled Willard thrust sheet. Key thermochronometric data and modeling results are first summarized, and sources of uncertainties in cooling ages and interpretations are addressed. Next, relations between thrust sheet emplacement and foreland sedimentation are discussed, and connections with hinterland crustal thickening are evaluated. Finally, along-strike variations in regional thrust timing, and relations to crustal architecture and evolving plate margin dynamics are explored.

6.1. Summary of Thermochronometric Data and Thermal Modeling

Samples from the cooler (T_{max} < 200 °C) eastern Monte Cristo transect have ZHe ages of approximately 160 Ma over a limited paleodepth range (Figure 6), interpreted to record Late Jurassic cooling from ~1.5 km of regional erosion, or alternatively an early phase of limited fault slip and erosion that preceded major thrust slip. ZHe ages of approximately 130–120 Ma for samples at restored depths of ~6 to 8 km (after Late Jurassic erosion) across the central to western parts of the Willard thrust sheet record onset of enhanced cooling during major thrust slip (Figures 7–9). ZHe ages decrease to approximately 100–90 Ma at restored depths of ~10 to 12 km, recording ~3 to 5 km of exhumation, with corresponding erosion rates of ~0.1 to 0.3 km/Myr and cooling rates of ~2 to 6 °C/Myr during major thrust slip. These erosion and cooling rates are broadly similar to values estimated for other retroarc fold-thrust belts (Fosdick et al., 2015; Giallorenzo et al., 2018; Mouthereau et al., 2014; Rak et al., 2017). In detail, thrust slip, cooling, and erosion rates were initially slower, and then increased from 105 to 92 Ma. Samples in structurally lower, western portions of the sheet at restored depths of ~12 to 14 km exhibit ZHe ages mostly from 70 to 60 Ma that record younger cooling as the Willard sheet was tilted and eroded during growth of the Wasatch anticlinorium. ZHe ages decrease systematically westward across the sheet along the Worm Creek and Browns Hole stratigraphic traverses, consistent with progressive eastward transport of the sheet upthrust ramps (Figure 10). ZFT grain ages of approximately 400–200 Ma for shallow samples reflect incomplete annealing of grains during stratigraphic burial. Samples from middle structural levels display complex patterns, with approximately 160–140-Ma ZFT ages of more retentive grains preserved in some samples likely related to Late Jurassic erosion, and approximately 120–100-Ma ages of most grains related to cooling during major thrust slip. ZFT ages of approximately 80–70 Ma in the lower western part of the sheet record cooling during early growth of the Wasatch anticlinorium. Ten sites have both ZFT and ZHe age data, with ZFT ages older by an average of 10 Ma, which for estimated closure temperatures of 220 and 170 °C of the ZFT and ZHe systems, respectively, indicate a cooling rate of 5 °C/Myr, similar to cooling rates estimated from ZHe age-paleodepth relations.

QTQt modeling of ZHe age-paleodepth relations along individual transects, incorporating uncertainties in cooling ages, broadly bracketed permissible thermal histories, but did not closely constrain the age for onset of major thrusting. The model allows for random changes in thermal gradients between time steps that may not be geologically realistic and give overly broad brackets for *T*-*t* paths. More refined estimates of thrust timing were obtained by combining thermochronometric data for all transects with thermo-kinematic modeling.

ZHe age-paleodepth relations along multiple structural transects, ZHe age-distance relations across stratigraphic traverses, well-characterized structural geometry of the Willard sheet, and provenance of synorogenic strata provided key constraints for thermo-kinematic models. Models were run for a range of fault slip histories, rock thermal properties, and basal T boundary conditions. The preferred model that best matched observed ZHe ages had 1.5 km of later Jurassic erosion, onset of major thrust slip at 125 Ma with early slower slip (1 km/Myr) from 125 to 105 Ma and faster slip (3 km/Myr) from 105 to 92 Ma, heterogeneous thermal conductivity related to rock type, and westward increasing basal T and heat flow from ~55

to 60 mW/m^2. Some other models, although having poorer fits, gave predicted cooling ages that still overlapped many sample ZHe ages within 95% uncertainty levels, reflecting trade-offs between initial stratigraphic depth, thermal gradient tied to basal *T*, and erosion rates.

6.2. Sources of Uncertainties in Cooling Ages and Interpretations

Understanding sources of intrasample dispersion in grain cooling ages is important for evaluating uncertainties in thermochronometric interpretations and optimizing sampling design. Most samples in this study displayed greater dispersion in ZHe grain ages (typical 1σ ~10% of mean age) than expected for analytical uncertainty (~4% of grain age), similar to results of other studies (e.g., Wolfe & Stockli, 2010; Guenthner et al., 2015; Powell et al., 2016; Ault et al., 2018), partly related to varying radiation damage that affects He diffusion (Guenthner et al., 2013). Grains were selected for ZHe analysis based on similar eU contents (mostly 30 to 300 ppm) and U-Pb ages (mostly 2.0–1.0 Ga), and thus similar values of maximum accumulated radiation damage. Actual radiation damage in detrital grains also depends on prior basement cooling histories that may have varied among grains. For deeper samples heated above ~300 °C, prior radiation damage is annealed and He degassed, removing memories of prior thermal histories. For shallower samples not heated above ~200 °C, ZHe ages may vary widely due to varying He inheritance. Inheritance envelopes, calculated using the radiation-damage-accumulation-annealing model of Guenthner et al. (2013), are broadly consistent with the range of ZHe-eU grain values for the Monte Cristo transect (Figure 6d), and the range of values in upper level samples from the Wellsville and Promontory transects (Figure 13a). However, detailed relations among grain size, U-Pb age, eU, and ZHe age fail to precisely match model predictions, suggesting additional sources of dispersion, such as U-Th zoning, presence of flaws that act as He traps (fluid inclusions) and fast pathways (microcracks), nonideal grain shapes, and limitations of the current model (Danišík et al., 2017; Meesters & Dunai, 2002). For this study, zircon grains were selected based on lack of U-Th zonation in laser-ablation depth profiles, but U-Th contents may have varied in other parts of grains. Presence of higher eU regions near a grain core results in less He loss by diffusion and an overestimate of the alpha ejection factor, leading to an older ZHe age compared to a homogeneous grain. Conversely, presence of higher eU regions near a grain rim leads to a younger ZHe grain age. Grains with visually obvious inclusions and cracks were avoided, but smaller flaws may be present, also adding to dispersion. The model of Guenthner et al. (2013) uses empirical factors for zircon FT annealing as a proxy for annealing of alpha damage, but healing mechanisms are incompletely understood and depend on accumulated radiation damage (Brandon et al., 1998; Rahn et al., 2004), adding uncertainties for interpreting ZHe-eU relations. Additionally, models of quantitative relations between radiation damage and He diffusion in zircon likely need refinement (Anderson et al., 2017; Powell et al., 2016; Weisberg et al., 2018).

Sampling schemes should reflect ZHe age uncertainties, desired precision, and nature of cooling histories. For this study, samples were collected at an ~1-km paleodepth spacing, with six grains analyzed per sample. Analysis of six grains yields a typical 95% confidence interval of about ±10 Ma for a 100-Ma ZHe sample age. Decreasing the number of grains per sample to three would allow analysis of more samples, but would increase age uncertainty. A paleodepth spacing of ~1 km is well suited for a sample age uncertainty of ±10 Ma and an erosion rate of 0.2 km/Myr. Sampling was based on paleodepths from restored cross sections of the Willard sheet that show spatial relations during Cretaceous thrusting and cooling, rather than current elevations that mostly reflect Neogene extension and erosion. Grains were selected based on similar eU, U-Pb age, and maximum radiation damage to lessen dispersion of grain ZHe ages, which is appropriate if samples can be collected across a large paleodepth range to yield age-depth relations, as was the case for the Willard thrust sheet. However, if the exposed paleodepth range is limited, constraints on lower *T* parts of cooling histories are needed, or samples were not heated above *T* ~200 °C, then selecting grains with a wide range of eU, including highly damaged grains with lower closure temperature, may be appropriate to better constrain thermal histories (Ault et al., 2018; Orme et al., 2016).

ZFT grain ages also display complex patterns at middle levels of the Willard thrust sheet, with different age subgroups interpreted to reflect varying track annealing rates related to accumulated radiation damage. Closure temperature for less retentive grains with approximately 100-Ma ZFT ages at middle levels is estimated as ~220 °C, based on comparison to *T*-*t* paths obtained from ZHe-paleodepth relations and thermal models. This value is similar to values estimated for other natural zircon grains with moderate radiation damage and cooling rates of ~2 to 5 °C/Myr (Brandon et al., 1998; compilation in Rahn et al., 2004), but is

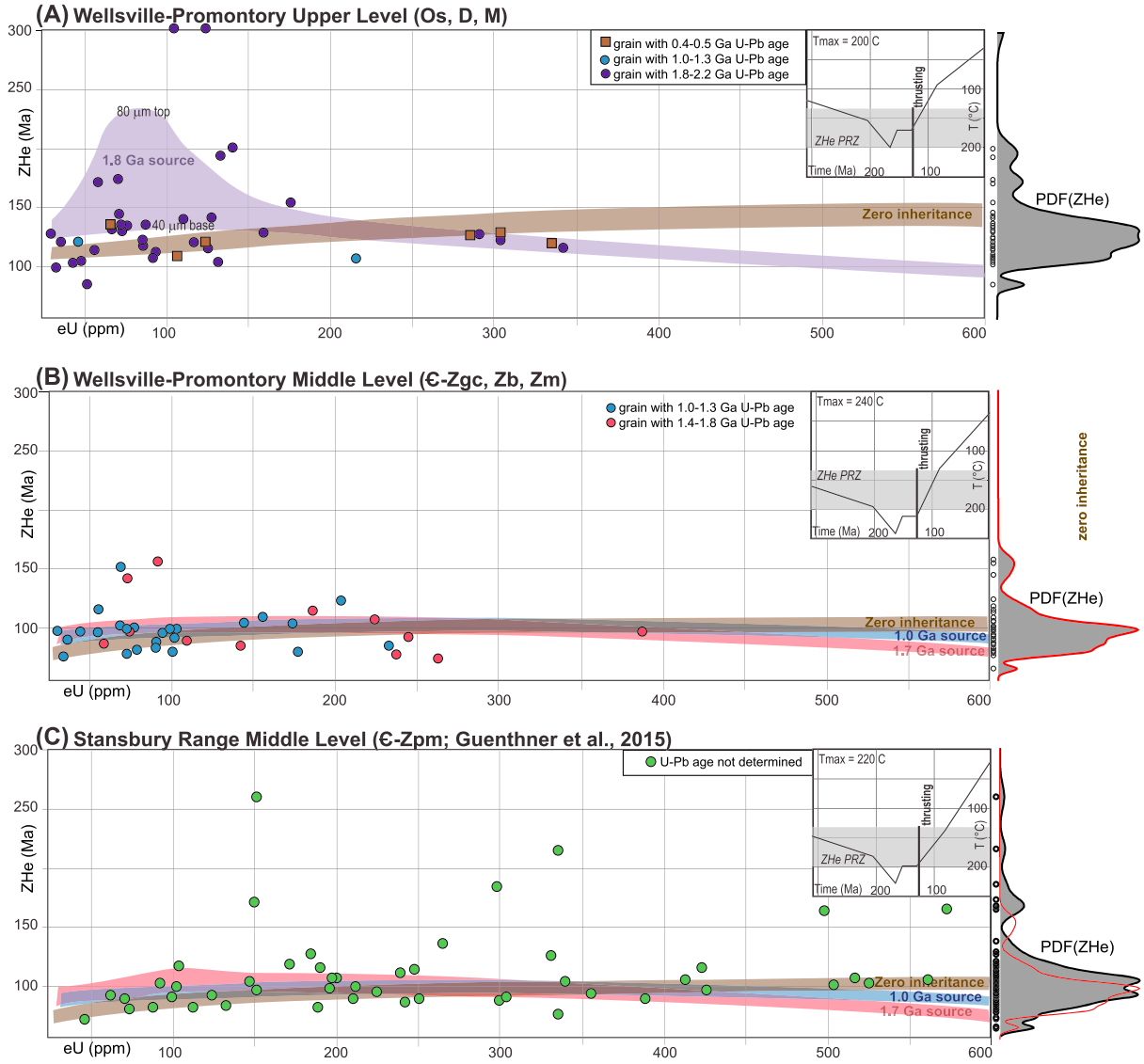

Figure 13. Observed ZHe-eU grain values for selected paleodepth levels and areas, and predicted envelopes for prior inheritance from different age basement sources and zero inheritance for grain sizes of 40 to 80 µm, calculated using HeFTY software (Ketcham, 2005), radiation-diffusion model of Guenthner et al. (2013), and thermal history indicated in the top right corner of each plot. Probability density functions (PDF) of ZHe ages shown on the right side of each plot. (a) ZHe-eU relations for pooled samples from upper levels (Mississippian, Devonian, Ordovician strata) of the Wellsville and Promontory transects. ZHe grain ages display larger dispersion partly related to He inheritance. (b) ZHe-eU relations for pooled samples from middle levels (Geertsen Canyon to Mutual formations) of the Wellsville and Promontory transects. ZHe grain ages range mostly from 110 to 80 Ma and define a quasi-normal distribution. (c) ZHe-eU relations for samples from the Prospect Mountain Formation in the Stansbury Range reported by Guenthner et al. (2015). ZHe grain ages range mostly from 120 to 80 Ma and define a quasi-normal distribution, similar to the pattern for middle levels of the Willard sheet (indicated by red outline).

lower than closure temperatures calculated from extrapolation of lab measurements to geologic time scales (Tagami et al., 1998).

6.3. Relations Between Thrust Sheet Emplacement and Foreland Sedimentation

Jurassic and Cretaceous synorogenic strata provide a complimentary record of the emplacement history of the Willard sheet. The area of the future Sevier belt experienced slow subsidence during the Triassic to Early Jurassic with deposition of mixed marine and continental strata. Subsidence rates increased during the Middle Jurassic, followed by development of a regional unconformity during the later Jurassic to earliest Cretaceous. Deposition of thick, westward coarsening, Aptian to Turonian synorogenic strata record flexural

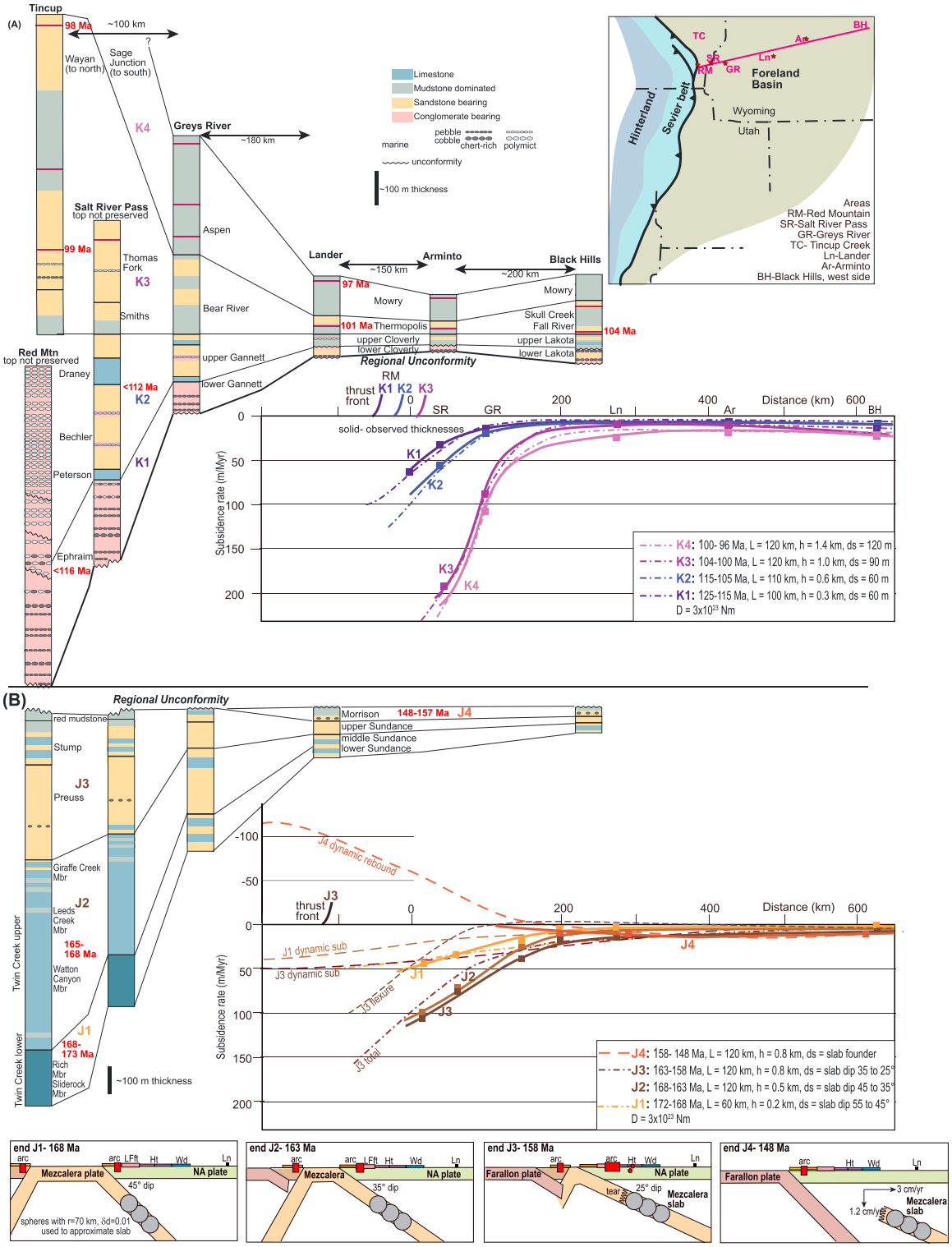

Figure 14. Generalized stratigraphic columns of (a) Cretaceous synorogenic strata divided into intervals K1 to K4 and (b) Jurassic strata divided into intervals J1 to J4 along a transect from the Willard sheet to the Black Hills (see inset map for locations). Ages for selected tuffs (in red), restored distances between columns, and formation names are indicated. Data are compiled from Eyer (1969), Imlay (1980), DeCelles (2004), Sprinkel et al. (2015), Christiansen et al. (2015), and Gentry et al. (2018). Graphs show observed sedimentation rates for intervals K1 to K4 and J1 to J4 as a function of distance from the Red Mountain area ($x = 0$) and predicted subsidence rates for a model that combines isostatic flexure and dynamic subsidence (dot-dashed lines). Half-width (L) and average height (h) of thrust sheets, and dynamic subsidence (d_s) parameters are listed. Cross sections at bottom show model subduction geometries and progressively restored locations of the Luning-Fencemaker belt (LF), hinterland (Ht), future Willard sheet (Wd), and foreland Lander (Ln) section.

subsidence during major slip on the Willard thrust. Key characteristics of Jurassic and Cretaceous strata, along with subsidence patterns related to thrust loading and subduction dynamics, are explored below.

Middle to Upper Jurassic strata, divided into four intervals (J1 to J4 in Figure 14b) based on lithology and subsidence patterns, record initial development of a foreland basin system. Ages are closely constrained by biostratigraphy (Imlay, 1980) and radiometrically dated tuffs (Christiansen et al., 2015; Sprinkel et al., 2015). Interval J1 corresponds to the mostly Bajocian (172–168 Ma) lower part of the Twin Creek Formation that comprises marine limestone, thickens gradually westward, and records initial incursion of the interior Sundance seaway. Interval J2 corresponds to the mostly Bathonian (168–163 Ma) upper part of the Twin Creek Formation that comprises marine limestone with minor fine-grained siliciclastic rocks, thickens moderately westward, and records increased sediment accumulation rates (up to 100 m/Myr). Interval J3 corresponds to the Callovian to Oxfordian (163–158 Ma) Preuss and Stump Formations that comprise red beds and interlayered marine limestone, sandstone, and mudstone; thicken westward; and record moderately high sedimentation rates (up to 100 m/Myr). Sandstone in this interval is sublithic (with chert and volcanic clasts) to subfeldspathic, contains rare pebbly lenses, and displays overall east directed paleocurrents, consistent with western sources from the hinterland and magmatic arc (Jordan, 1985). Drab, marine mudstone of the Stump Formation grades upward into a thin (<50 m), locally preserved unit of red mudstone. Although this unit has been included within the Ephraim Formation (Eyer, 1969), it lies beneath a regional unconformity marking the base of the conglomeratic main part of the Ephraim, and is herein included with the Stump Formation. The Preuss and Stump Formations are cut by the Meade and Willard thrusts, but lack coarse conglomeratic strata, precluding major fault slip during this interval. Small chert pebbles in these formations may have been eroded from Paleozoic strata in the hinterland of northwestern Utah to eastern Nevada, which experienced limited shortening and magmatism concentrated from 165 to 155 Ma (Miller & Hoisch, 1995), possibly related to a slab tear (Wyld & Wright, 2014). Interval J4 corresponds to the Tithonian to Kimmeridgian (158–148 Ma) Morrison Formation that contains fluvial sandstone, mudstone, and minor lacustrine limestone, and is only present in the foreland. Sandstone in this interval is subfeldspathic to sublithic, contains lenses of chert-pebble conglomerate, and displays east to northeast directed paleocurrents, consistent with western to southwestern sources (Currie, 1998; DeCelles, 2004). Ash-fall tuffs in the upper part of the formation record a change from subduction- to rift-related geochemical signatures, reflecting a change to transtension (Christiansen et al., 2015). The Morrison Formation may have been deposited in a backbulge setting with a phantom foredeep located westward (DeCelles, 2004), or during dynamic subsidence related to foundering of a subducted oceanic slab (Lawton, 1994). Presence of a foredeep, however, is problematic as approximately 160 Ma cooling ages in the Willard sheet preclude burial by thick Late Jurassic strata, and a regional unconformity separating the Stump Formation and conglomeratic Ephraim Formation precludes removal of thick Late Jurassic strata during Cretaceous thrusting in the footwall.

Regional thickness variations within intervals J1 to J4 are compared with a model that combines isostatic flexure from shortening and sediment redistribution (calculated from equations in Angevine et al. (1990)), and dynamic subsidence from sinking of a dense oceanic slab (calculated from equations in Morgan (1965), using a series of spheres to approximate a 120-km-thick slab having a density difference of 0.01). Subsidence (or rebound) over a given time interval results from net changes in isostatic flexure (with a typical wavelength of ~200 km related to changing thrust sheet topography) and dynamic subsidence (with a longer wavelength of ~1,000 km related to changing subduction geometry; Mitrovica et al., 1989; DeCelles & Giles, 1996). If the rate of thickening and uplift of a thrust sheet is greater than the erosion rate, then thrust topography grows and isostatic flexure increases. If the dip of a subducting slab decreases, then the width and magnitude of dynamic subsidence increase, whereas if a slab founders, then loading decreases leading to rebound. Increasing sedimentation rates during interval J1 may reflect dynamic subsidence as the dip of the subducting oceanic (Mezcalera) slab began to decrease. Intervals J2 and J3 show increased westward thickening over a wavelength of ~300 km, likely reflecting both isostatic flexure from hinterland shortening and dynamic subsidence from further decreases in the dip of the Mezcalera slab, as suggested by eastward migration of arc activity (Elison, 1995). Alternatively, Bjerrum and Dorsey (1995) invoked an unusually high flexural rigidity of 10^{24} Nm plus widespread sediment redistribution to form a wide foredeep during hinterland thickening. An unconformity developed across much of the future Sevier belt during the later Jurassic, with an estimated ~1 to 2 km of erosion across the Willard sheet, which can be partly explained by dynamic

rebound during tearing and foundering of the Mezcalera slab and start of Franciscan subduction. Predicted uplift rates are ~50 to 100 m/Myr across the future Willard sheet from 158 to 148 Ma, such that erosion of nonresistant Jurassic strata, combined with added rebound from thermal thinning of the lithosphere during later Jurassic plutonism (Elison, 1995), could produce interpreted regional erosion across the Willard sheet. Slow sedimentation rates for the Morrison Formation in a broad basin farther east (Currie, 1998) may reflect a waning wave of dynamic subsidence as the North American plate drifted northwestward (at ~3 cm/year) over the foundering Mezcalera slab (with a sinking rate of ~1 to 1.5 cm/year), followed by minor rebound and development of an unconformity. Although speculative, the model explains general patterns of middle to later Jurassic sedimentation and erosion. Increasing (or decreasing) the oceanic slab thickness and density contrast would increase (or decrease) the magnitude of dynamic subsidence and subsequent rebound.

Lower to mid-Cretaceous strata record a change in foreland sedimentation patterns related to major slip on the Willard thrust, and are divided into four intervals (K1 to K4 in Figure 14a; Gentry et al., 2018). Interval K1 corresponds to the Aptian (approximately 125–115 Ma) Ephraim Formation that contains sandstone, chert-pebble conglomerate, and mudstone. Heller and Paola (1989) interpreted these strata to record long-distance fluvial transport away from a thermally uplifted hinterland based on an apparent lack of thick, coarse strata representative of a foredeep. However, the Ephraim Formation thickens asymmetrically westward and contains cobble conglomerate in the Red Mountain area, recording major slip on the Paris-Willard thrusts (Figure 14a; Gentry et al., 2018). The age for the lowest conglomeratic part of the Ephraim Formation is poorly constrained, but the upper part of the formation contains 115-Ma U-Pb age zircon grains that bracket depositional age, consistent with approximately 125 Ma start of major thrusting. Initially, the foredeep was overfilled as erosion of nonresistant Mesozoic strata at shallower levels of the Willard sheet provided abundant sediment, and fault slip rate was slower. Interval K2 corresponds to the lower Albian (approximately 115–105 Ma) Bechler Formation that also thickens rapidly westward and contains boulder conglomerate in the proximal Red Mountain area, whereas mostly finer grained clastic rocks and lacustrine limestone were deposited eastward. Relations are consistent with an episodically underfilled foredeep during growing thrust sheet topography, with coarse sediments trapped near the mountain front. Erosion rates may also have slowed as more resistant Paleozoic carbonates became exposed across the thrust sheet, and possibly during periods of drier climate (Drummond et al., 1996). Interval K3 corresponds to the upper Albian (105–100 Ma) Bear River Formation and correlative strata that contain marine to fluvial sandstone, pebbly sandstone, and mudstone; thicken rapidly westward; and record increased sedimentation rates (up to 200 m/Myr; Rubey, 1973; Gentry et al., 2018). Interval K4 corresponds to the mostly Cenomanian (100–96 Ma) Aspen to Lower Frontier Formation and correlative strata that also contain marine to fluvial sandstone, pebbly sandstone, and mudstone; thicken rapidly westward; and record continued high sedimentation rates. The 105–95-Ma age range of increased subsidence rates is similar to the age range for faster thrust slip rates inferred from cooling age-paleodepth relations. Faster slip rates likely led to growing topography, as erosion did not keep pace with uplift above thrust ramps. The overlying Turonian (94–90 Ma) upper Frontier Formation marks a transition to sediment sources from both the Willard sheet and Wasatch anticlinorium, as slip transferred onto the more eastern Ogden and Crawford thrusts.

Regional thickness variations of intervals K1 to K4 show a distinct foredeep and broad forebulge zone farther east, consistent with flexural loading from growing topography across the Willard sheet (Figure 14a; Gentry et al., 2018). The model also includes a smaller component of dynamic subsidence to match deposition in distal areas.

6.4. Relations Between Thrust Shortening and Hinterland Crustal Thickening

Upper crustal shortening of the sedimentary cover in the Willard and eastern thrust sheets of the Sevier belt was balanced by corresponding lower crustal thickening in the hinterland and underthrusting beneath the magmatic arc. Key constraints on timing and styles of hinterland deformation, metamorphism, and paleoelevation are summarized below, and then compared with timing and rates of Sevier thrusting to develop a simple crustal balance model (Figure 15).

The hinterland at the latitude of northern Utah to Nevada comprises the western Luning-Fencemaker belt, central Nevada fold-thrust belt, and eastern metamorphic core complexes separated by gently tilted, little metamorphosed Paleozoic strata. The Luning-Fencemaker belt accommodated ~100 km of shortening and

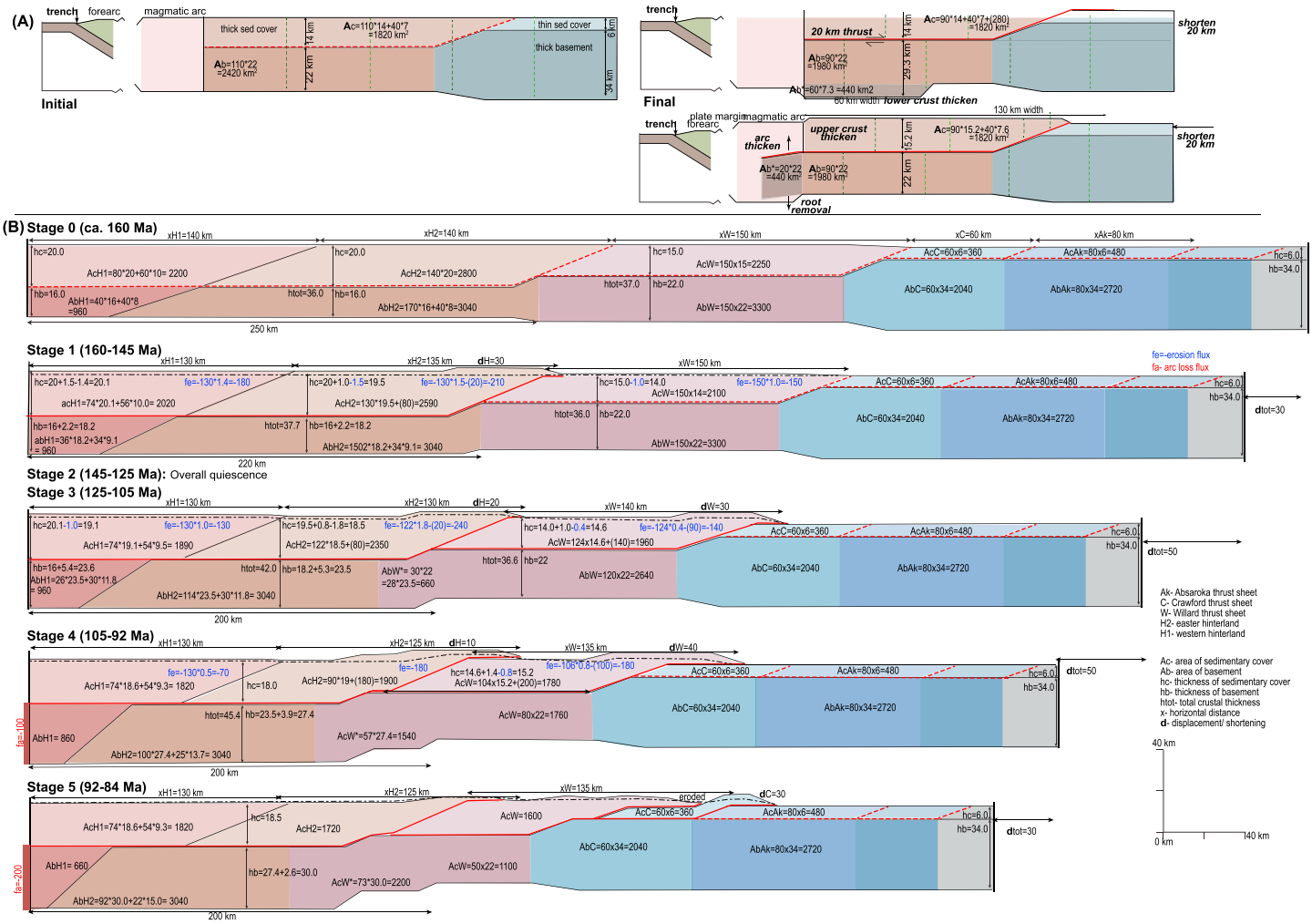

Figure 15. (a) Cartoon illustrates area (A) balance between shortening of sedimentary cover by thin-skin thrusting, and lower crustal thickening and underthrusting into the magmatic arc in reference frame of a "fixed" trench. Crustal thickness (h) listed for initial and final stages. Material is removed from the wedge by erosional flux (f_e) with erosion surface indicated by dot-dashed line. (b) Simplified crustal balance model for the Sevier belt and hinterland during progressive stages. The primary wedge has basement overlain by a westward thickening sedimentary cover, with pericratonic terranes to the west. Model values of Sevier shortening, hinterland upper crustal shortening, hinterland lower crustal thickening, and erosion are indicated for each stage, along with average crustal thickness. Thin-skinned shortening in the Sevier belt is balanced by lower crustal thickening beneath the hinterland, with growth of an orogenic plateau.

associated thickening of back-arc basin strata, mostly during the mid-Jurassic (Wyld, 2002). Unconformably overlying continental strata of the approximately 135–120-Ma King Lear Formation were then deposited within transtensional basins, recording a switch in tectonic mode (Martin et al., 2010). The central Nevada belt may have experienced limited shortening during the Late Jurassic, based on correlation with faults to the south (Giallorenzo et al., 2018), and during the Early Cretaceous (Long et al., 2014; Taylor et al., 2000). The Aptian-Albian Newark Canyon Formation was deposited in wedge-top basins east of the belt, and the overlying Upper Cretaceous to Paleogene Sheep Pass Formation was deposited in internally drained basins during a switch to upper crustal extension (Druschke et al., 2011). The eastern hinterland experienced limited Late Jurassic shortening (Allmendinger & Jordan, 1984), with more concentrated shortening in the Raft River-Albion-Grouse Creek core complex where rocks reached peak depths of ~35 km at approximately 85 Ma, followed by later Cretaceous to Paleocene alternating local extension to shortening, and Eocene to Miocene rapid extension (Wells et al., 2000, 2012).

The hinterland likely developed into a topographic plateau, referred to as the Nevadaplano (DeCelles, 2004), with crustal thickness reaching 50 to 60 km during the Late Cretaceous, based on restoration of current

crustal thickness for Tertiary extension (Coney & Harms, 1984), elevated pressures recorded by metamorphic rocks (Wells et al., 2012), crustal shortening balances (DeCelles & Coogan, 2006), and paleoelevation estimates. Similar fossil assemblages within the Newark Canyon Formation and correlative strata in the foreland indicate limited elevation differences at approximately 120 Ma (Bonde et al., 2015), whereas clumped C-O isotopic signatures in the Sheep Pass Formation and temporally correlative foreland strata indicate paleoelevations of ~2 to 3 km in the hinterland by 70 Ma (Snell et al., 2014). Erosional exhumation of the hinterland was limited during later Cretaceous to Paleocene topographic isolation and development of a widespread unconformity across Paleozoic strata (Long, 2013).

A simple model connecting thin-skinned shortening in the Sevier belt with lower crustal thickening beneath the hinterland is shown in Figure 15 for stages spanning the mid-Jurassic to later Cretaceous. Key model parameters include timing and rates of thrust slip in the Sevier belt, position of the regional décollement and lower crustal thickening, erosion amounts, and initial crustal thicknesses (taken as 40 km for the future Sevier belt and 36 km for pericratonic terranes). The model balances areas of basement and sedimentary cover during progressive shortening and erosion, in a reference frame of upper plate motion relative to the trench (Figure 15a). The model approximates lower crustal thickening with distributed pure shear, and upper crustal shortening with simplified thrust geometries and distributed fold shortening, providing a conceptual framework based on general regional constraints, rather than attempting detailed, sequential restorations.

During stage 1 (160–145 Ma) of the model, the hinterland undergoes 30 km of upper crustal shortening, balanced by ~3 km of lower crustal thickening across a width of 220 km. The upper crust experiences 1 to 2 km of erosion, and average crustal thickness in the hinterland increases to ~38 km (Figure 15b). During stage 2 (145–125 Ma), most of the region experiences quiescence and slow erosion. During stage 3 (125–105 Ma), the Willard thrust sheet has 20 km of slip at a rate 1 km/Myr and the hinterland undergoes 20 km of upper crustal shortening, which together are balanced by ~5 km of lower crustal thickening beneath the hinterland. The hinterland and Willard sheet experience moderately increased erosion, with synorogenic strata deposited in the foreland basin. Average crustal thickness in the hinterland increases to ~42 km and paleoelevation begins rising. During stage 4 (105–92 Ma), the Willard thrust has 40 km of slip at a faster rate of 3 km/Myr, and the hinterland undergoes 10 km of upper crustal shortening, which together are balanced by ~4 km of lower crustal thickening beneath the hinterland. Erosion increases across the Willard sheet, along with increased sedimentation in the foreland basin. Average crustal thickness of the hinterland increases to ~45 km and paleoelevation continues to rise. During stage 5 (92–84 Ma), Sevier deformation propagates eastward onto the Crawford thrust sheet that accommodates 30 km of shortening, balanced by ~3 km of lower crustal thickening below the hinterland. The hinterland transitions into a topographically isolated plateau, while erosion is concentrated along frontal parts of the Sevier belt. Average crustal thickness of the hinterland increases to ~49 km and some lower crust is underthrust and partly melted beneath the magmatic arc. During stage 6 (approximately 80–50 Ma), the wedge front continues propagating eastward with ~60 km of shortening in the Absaroka and Hogsback thrust sheets, balanced by ~6 km of lower crustal thickening beneath the hinterland, while the upper crust undergoes local extension. Average crustal thickness in the hinterland reaches a maximum of ~55 km, with paleoelevation increasing to 3 km, based on a simple isostatic balance, similar to values interpreted by DeCelles and Coogan (2006). Alternating synconvergent extension to shortening at different structural levels in the hinterland reflects a dynamic interplay between tectonic compressive forces, gravitational potential energy of elevated crust, mantle lithosphere thinning, and surface processes (Wells et al., 2012). Although simplistic, the model illustrates connections between Sevier thin-skinned shortening and hinterland lower crustal thickening, leading to uplift of a broad orogenic plateau.

6.5. Regional Thrust Timing and Relations to Crustal Architecture and Plate Dynamics

The timing for onset of thrusting in the Sevier belt (herein taken as the region marked by thin-skinned thrusting of passive margin to platform strata, as compared to the hinterland region marked by middle to lower crustal metamorphism and thickening) has been widely debated and likely varied regionally along the length of the orogenic system (Armstrong & Oriel, 1965; DeCelles, 2004; Fuentes et al., 2009; Giallorenzo et al., 2018; Heller et al., 1986; Heller & Paola, 1989). Timing relations are briefly summarized at the latitudes of northern to central Utah, southern Nevada, and Alberta to NW Montana. Relations are

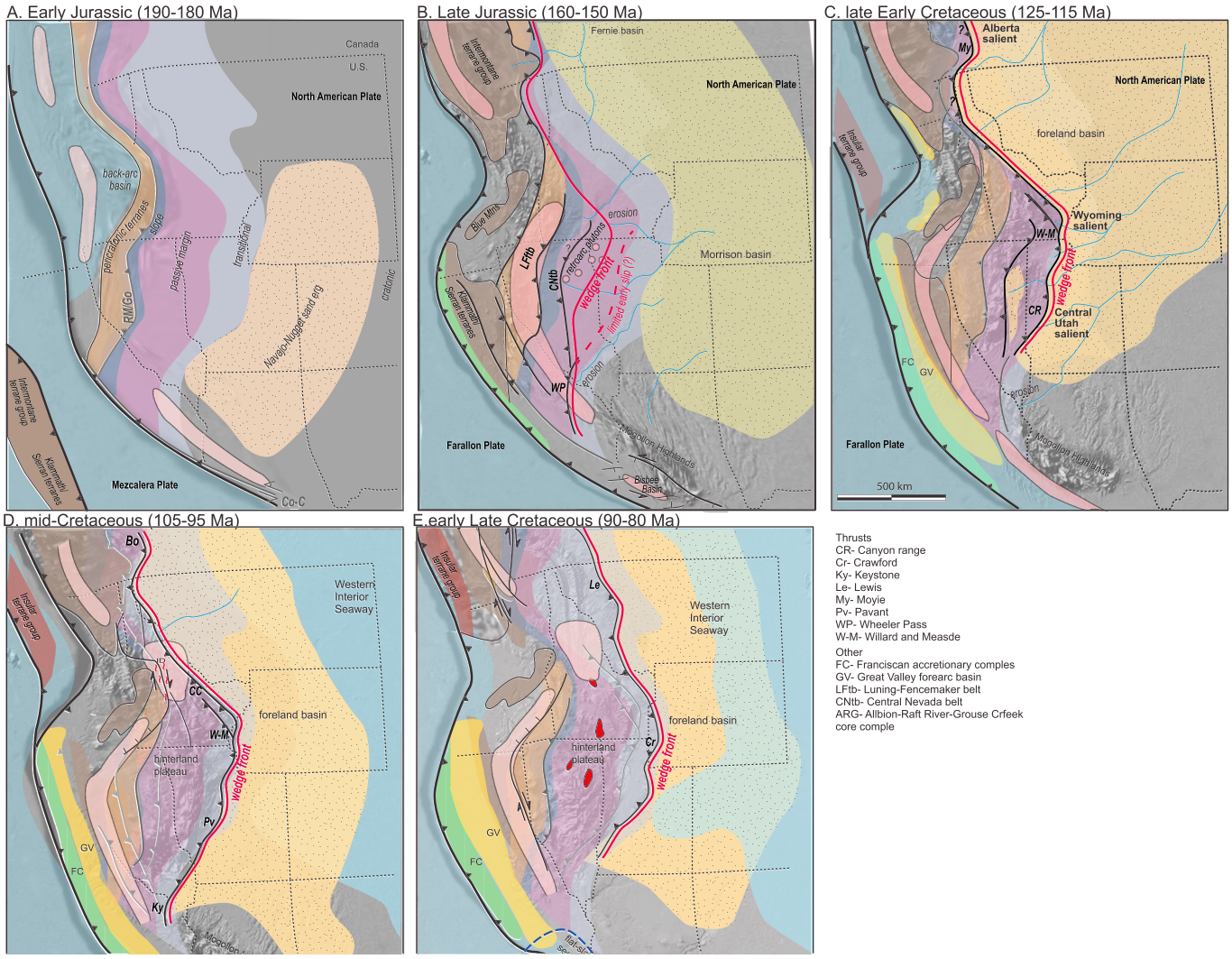

Figure 16. Paleogeographic reconstructions of the Cordilleran orogenic system illustrate relations between thin-skinned shortening in the Sevier fold-thrust belt, deposition of synorogenic strata in the foreland basin (yellow shadings), growth of topography, activity of the magmatic arc (red shadings), plate convergence, and terrane accretion. Reconstructions shown for (a) Early Jurassic initial crustal architecture; (b) Late Jurassic terrane accretion and consolidation of the subduction boundary, early shortening in western parts of the retroarc, and early basins; (c) late Early Cretaceous shortening along western thrusts of the Sevier belt and development of a regional foreland basin; (d) mid-Cretaceous increased shortening rates in Sevier belt, enhanced subsidence of foreland basin, growth of topography in the hinterland, and increased activity along magmatic arc; and (e) Late Cretaceous propagation of eastern thrusts of the Sevier belt, continued foreland subsidence, and initial development of the flat-slab segment. Leading edge of the shortening retroarc orogenic wedge indicated by red line. Maps partly based on reconstructions by Price (1994), DeCelles (2004), and Yonkee and Weil (2015).

used to construct a series of paleogeographic maps showing location of active shortening (Figure 16), and compared with along-strike variations in crustal architecture and temporal changes in plate margin dynamics.

At the latitude of the northern Utah, shortening occurred within the hinterland during the later Jurassic (Allmendinger & Jordan, 1984; Cruz-Uribe et al., 2015), while erosion occurred across the future Sevier belt and the Morrison Formation was deposited farther east (Figure 17). The orogenic wedge front then propagated eastward onto the Willard thrust of the western Sevier belt. Thermochronometric data (Figures 7–10) and recent analysis of synorogenic strata (Gentry et al., 2018) clarify the timing for onset of major slip on the Willard thrust at approximately 125 Ma, continuing to approximately 92 Ma, followed by eastward propagation of the Crawford and early Absaroka thrusts and associated early uplift of the Wasatch anticlinorium.

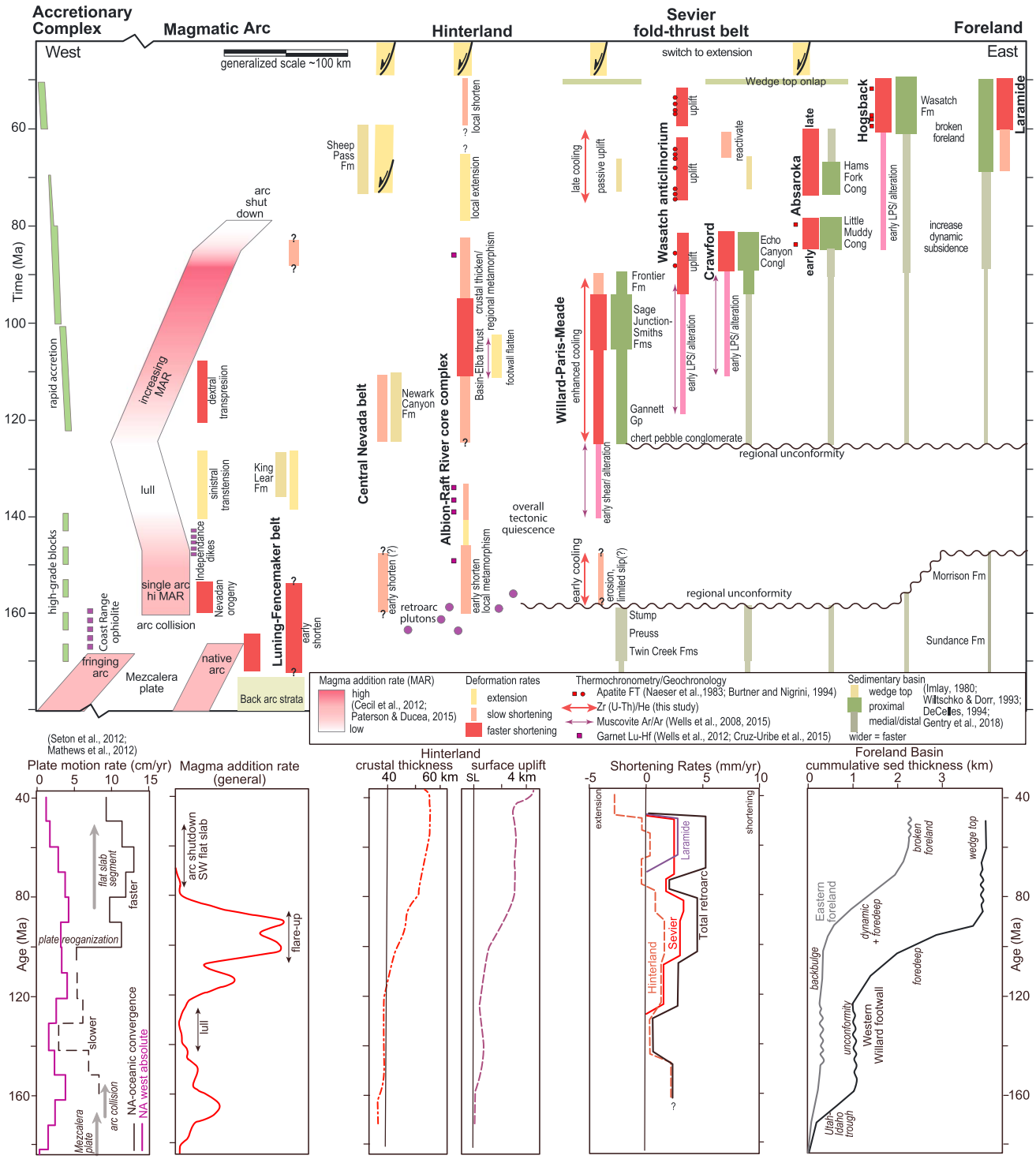

Figure 17. Summary of temporal relations between thrust slip in the Sevier belt, foreland sedimentation, hinterland deformation, and arc magmatism. Available geochronologic and thermochronometric data (Naeser et al., 1983; Burtner & Nigrini, 1994; Wells et al., 2008, 2015; Cruz-Uribe et al., 2015; this study) record overall west to east propagation of the thrusts and protracted uplift of the Wasatch anticlinorium in the Sevier belt. Relative deformation rates given by colors; lighter to darker blues indicate slower to faster shortening rates, and orange hues indicate extension. Synorogenic strata across the foreland (in various shades of green) provide a long-term record to flexural loading during progressive emplacement of thrust sheets (Imlay, 1980; DeCelles, 1994; Wiltschko & Dorr, 1983). The hinterland records a polyphase history of metamorphism, magmatism, and early shortening to later extension (Wells et al., 2012). The magmatic arc experienced flare-ups and lulls, along with migration in response to changing dip of the subducting slab (Cecil et al., 2012; Paterson & Ducea, 2015). Bottom plots show plate motion rates (Matthews et al., 2012; Seton et al., 2012), magma addition rates, generalized hinterland topographic evolution, upper crustal shortening rates for the hinterland and Sevier belts, and representative sedimentary thickness curves from the foreland modified from Yonkee and Weil (2015).

The adjoining Charleston-Nebo salient to the south also experienced Early Cretaceous thrusting, based on ZHe ages of approximately 110–90 Ma reported by Guenthner et al. (2015) for the Prospect Mountain Formation exposed in the Stansbury Range (Figure 13c), similar to ZHe ages from the correlative Geertsen Canyon Formation exposed at middle levels in the Willard sheet (Figure 13b). Guenthner et al. (2015) explored a range of potential thermal histories with exhumation starting sometime between 120 and 80 Ma and different T_{max}, but acknowledged difficulties in constraining the thermal history due to the limited paleodepth range of the samples. Our preferred thermal history for the area, informed by relations at similar levels in the Willard sheet, has T_{max} of 220 °C during the mid-Jurassic and enhanced cooling from 125 to 80 Ma, which gives inheritance envelopes that bracket most ZHe-eU grain values. Details of the thrust slip history, however, are poorly constrained due to the limited paleodepth range of samples.

Within the central Utah salient, DeCelles and Coogan (2006) proposed that slip on the Canyon Range thrust in the western Sevier belt started by 145 Ma. The Upper Jurassic Morrison Formation is thicker across the Colorado Plateau as compared to Wyoming, which may reflect greater shortening in the hinterland or an early phase of slip on the Canyon Range thrust (Currie, 1998). Conglomerate-bearing strata of the mostly Aptian Cedar Mountain Formation and more proximal Aptian-Albian San Pitch Formation include clasts and detrital zircon grains derived from Lower Paleozoic carbonates to Neoproterozoic quartzite, recording deep exhumation of the Canyon Range sheet (Hunt et al., 2011; Lawton et al., 2010; Sprinkel et al., 1999). The western thrust system in central Utah thus also experienced major slip from approximately 125 to 105 Ma, but overall deeper erosion levels here may reflect a component of prior Jurassic slip and erosion, or a steeper ramp trajectory compared to the Willard sheet. Slip propagated eastward onto the Pavant thrust that experienced significant cooling during the Cenomanian, synchronous with wedge-top deposition of the lower part of the Canyon Range Conglomerate (Pujols et al., 2018).

Farther south in southern Nevada to southeast California, 160–145-Ma ZHe ages record Late Jurassic onset of major slip along the Wheeler Pass thrust in the western Sevier belt, which was located closer to the magmatic arc in this area (Giallorenzo et al., 2018). Early shortening in the Sevier belt here overlapped with crustal thickening and regional metamorphism in hinterland rocks of the Funeral Mountains (Hoisch et al., 2014). The Wheeler Pass sheet and foreland experienced Late Jurassic erosion, likely related to broad uplift near the magmatic arc, with sediment transported northeastward and likely deposited in the Morrison Formation. Following a period of quiescence, major slip propagated eastward on the Keystone thrust from approximately 105 to 95 Ma, synchronous with local deposition of synorogenic strata in the foreland and passive uplift of the Wheeler Pass sheet (Giallorenzo et al., 2018).

Farther north in western Alberta to British Columbia and northwest Montana, relations record protracted growth of the hinterland, Sevier belt, and foreland basin system. The hinterland experienced Middle to Late Jurassic shortening and igneous intrusion associated with terrane accretion; Early to mid-Cretaceous crustal thickening, regional metamorphism, and shear along zones that linked eastward into thrusts in the Sevier belt; and Paleocene to Eocene extension (Gervais & Brown, 2011; Simony & Carr, 2011; Webster et al., 2017). Gervais and Hynes (2013) reported groupings of U-Pb monazite ages at approximately 150, 122–94, and 76–58 Ma in parts of the hinterland. Pana and van der Pluijm (2015) reported clusters of $^{40}Ar/^{39}Ar$ clay ages from fault gouge samples at 163–146 Ma for western thrusts, 103–99 Ma and 76–72 for central thrusts, and 52–50 Ma for eastern thrusts of the Sevier belt, which they interpreted to record deformation pulses. Fault gouge ages, however, may only record parts of protracted fault slip histories. In comparison, subsidence patterns across the foreland basin record long-term flexural loading from a growing fold-thrust wedge. Late Jurassic strata record onset of flexural loading, with a mix of western (hinterland) and southern sediment sources (Fuentes et al., 2009; Gillespie & Heller, 1995; Raines et al., 2013). A regional unconformity developed across much of the foreland from approximately 140 to 125 Ma during a period of overall quiescence, followed by widespread deposition of Aptian chert-pebble conglomerate (Leier & Gehrels, 2011), similar to patterns in Utah and Wyoming interpreted to record start of a new phase of major thrusting. Subsidence and deposition of thick strata within an eastward migrating foredeep continued during Aptian to Paleocene growth of the fold-thrust belt, with short hiatuses during the latest Albian and the Maastrichtian (Price, 1994).

Timing for onset of thrusting in the Sevier belt (as defined herein exclusive of the hinterland region) thus ranged from the Early Cretaceous in central parts of the retroarc to Late Jurassic in more southern and

northern parts, which appears related to regional variations in crustal architecture (Figure 16a). In central parts of the retroarc (at the latitude of Utah), the future Sevier belt was located far inboard from the plate margin and magmatic arc due to presence of a wide passive margin and prior accretion of pericratonic terranes. Farther south (at the latitude of southern Nevada), the passive margin was narrower and located close to the magmatic arc due to prior truncation of southwestern Laurentia along the California-Coahuila transform during Permian to Triassic time (Dickinson & Lawton, 2001). Farther north (at the latitude of Alberta), pericratonic terranes were narrow and the passive margin was located at intermediate distances from the plate margin prior to Jurassic accretion of the Intermontane terrane group. Thus, in central parts of the retroarc, the orogenic wedge front had to first propagate across a wide hinterland during the Late Jurassic, prior to eastward propagation and major slip on the Willard thrust in the Sevier belt during the Early Cretaceous. To the south, the wedge front propagated rapidly eastward across the narrower passive margin, with Late Jurassic slip on the Wheeler Pass thrust, followed by a lull in activity and mid-Cretaceous eastward propagation and slip on the Keystone thrust system. The total amount of thrust shortening was less to the south, reflecting the narrower, thinner sedimentary prism. To the north, shortening propagated into far western thrusts of the Sevier belt during Late Jurassic terrane accretion, with subsequent eastward thrust propagation and major shortening across the Sevier belt during the Early to mid-Cretaceous.

Thrust timing and shortening rates, as well as magmatic arc activity, display broadly consistent tempos along much of the length of the retroarc, suggestive of relations to plate margin dynamics (Figure 17). Retroarc shortening was widespread during the Late Jurassic, beginning close to the magmatic arc. This early episode of shortening was broadly synchronous with terrane accretion (Intermontane terrane group in the north, Klamath and Sierran terranes to the south) and development of a consolidated east dipping subduction zone and associated magmatic arc (Figure 16b). Convergence rates are poorly constrained, in part due to the potential for missing oceanic plates and back arc basins that have been entirely subducted. Uncertainties also exist in the detailed timing for consolidation of the subduction zone, with estimates ranging from approximately 180 to 150 Ma (Mulcahy et al., 2018; Price, 1994; Schweickert, 2015; Wakabayashi, 2015), complicating interpretation of early shortening in relation to plate margin dynamics.

A period of overall tectonic quiescence spanned approximately 140–125 Ma, marked by development of a regional unconformity along much of the retroarc. The magmatic arc retreated westward and magmatic activity decreased as the subduction angle steepened, which may have led to dynamic rebound and erosion. Plate convergence rates likely slowed during this period.

The orogenic wedge front then propagated eastward, with major slip along the western Sevier belt in central parts of the retroarc starting at approximately 125 Ma (Figure 16c). Presence of a weak basal fault zone combined with an overlying interval of strong quartzite allowed rapid propagation of the Willard thrust sheet at low taper. Slip rates on the Willard thrust were slower from approximately 125 to 105 Ma, and then increased. The Sevier belt, however, may have been inactive during this time farther south in southern Nevada. To the north in Alberta, flexural subsidence and provenance of foreland strata indicate thrust sheet loading and exhumation during the Aptian. The magmatic arc began migrating eastward as subduction angles decreased and igneous activity increased (Cecil et al., 2012). This period of renewed shortening temporally overlapped with a slight increase in westward motion of the North American plate (Figure 17).

Shortening rates increased during the mid-Cretaceous along much of the retroarc (Figure 16d). Slip rates increased from 105 to 92 Ma along the Willard thrust and subsidence rates increased across the Wyoming foreland. Slip also increased along the Pavant thrust in central Utah at approximately 105 Ma, major slip occurred along the Keystone thrust system in southern Nevada from 103 to 96 Ma (Wells, 2016), and 103–99-Ma fault gouge ages record slip along central thrusts in Alberta (Pana & van der Pluijm, 2015). The magmatic arc continued to migrate eastward with a significant increase (flare-up) in activity (Paterson & Ducea, 2015). Matthews et al. (2012) summarized marine geophysical evidence for mid-Cretaceous reorganization of global plate motions, including increased rates of plate convergence along the North American Cordilleran margin. Rates of upper plate motion in a mantle frame may also have increased, which combined with decreasing slab dip, likely increased plate coupling, retroarc shortening, and dynamic subsidence leading to incursion of the Western Interior seaway (Liu et al., 2008).

Shortening rates continued to be high along central to northern parts of the retroarc from approximately 90 to 80 Ma (Figure 17), although slip slowed or ceased along southern parts of the Sevier belt, synchronous

with disruption of the fore-arc and onset of flat-slab subduction at the latitude of Southern California (Figure 16e; Saleeby, 2003; Sharman et al., 2015). Slip transferred eastward onto the Crawford and early Absaroka thrusts in the Wyoming salient. Rapid subsidence expanded across the foreland of eastern Utah to Wyoming, likely related to increasing dynamic subsidence ahead of the NE propagating flat-slab segment (Liu et al., 2008). High subsidence rates also continued within the foredeep in Alberta. The Sierra Nevada sector of the magmatic arc shut down toward the end of this period as the flat slab disrupted asthenospheric flow, but high rates of igneous activity continued along the magmatic arc to the north. This period corresponded to high plate convergence rates.

The onset of major Sevier thrusting in central parts of the retroarc during the Early Cretaceous occurred at the end of a magmatic lull, and the period of increased shortening rates during the mid-Cretaceous was roughly synchronous with hinterland crustal thickening and increasing activity along the magmatic arc. Relations between increased retroarc shortening rates, slightly delayed increases in magmatic addition rates, punctuated outward propagation of the orogenic wedge, and increased foreland basin subsidence are broadly consistent with the Cordilleran cycle model (DeCelles & Graham, 2015; Ducea & Barton, 2007), but are also temporally related to reorganization of plate motions (Figure 17).

7. Conclusions

1. Thermochronometric analysis of 47 samples spanning upper to lower levels of the Willard thrust sheet, combined with thermo-kinematic modeling, constrain the emplacement history of this areally extensive, far traveled sheet in the western part of the Sevier fold-thrust belt.
2. ZHe ages range from approximately 125 Ma at paleodepths of ~7 km to approximately 100–90 Ma at paleodepths of ~10 to 12 km across central to western parts of the Willard sheet, recording ~3 to 5 km of erosion during major thrust slip. ZHe ages of 160–150 Ma from the cooler eastern part of the sheet are interpreted to record Late Jurassic erosion that preceded major thrust slip. ZFT ages of approximately 120–100 Ma at paleodepths of ~10 to 12 km are on average 10 Ma older than ZHe ages for the same sample, recording cooling rates of ~5 °C/Myr. ZHe and ZFT ages at deeper levels (>12-km depth) record later cooling during uplift of the Wasatch anticlinorium.
3. Thermo-kinematic models were run to find what ranges of fault slip rates, rock thermal properties, basal T and heat flow boundary conditions, and erosion histories were consistent with cooling age patterns. The preferred model had 1.5 km of Late Jurassic erosion, onset of major thrust slip at 125 Ma with an early slower slip rate (1 km/Myr) and a late faster slip rate (3 km/Myr) from 105 to 92 Ma, heterogeneous thermal conductivity related to rock type, and westward increasing basal T and heat flow of ~50 to 60 mW/m^2.
4. Intrasample dispersion in ZHe grain ages (1σ ~10% of mean age) was greater than analytical uncertainty (~4% of grain age), likely reflecting a combination of He inheritance (especially for shallower samples), unrecognized U-Th zonation, and small flaws in zircon grains.
5. Synorogenic strata record a change from a slower subsiding, overfilled foreland basin during the Aptian, to a rapidly subsiding, underfilled basin from 105 to 95 Ma, consistent with increasing fault slip rates during this time based on thermochronometric data.
6. A simple crustal balance model linking rates of upper crustal, thin-skinned shortening in the Sevier fold-thrust belt with lower crustal thickening in the hinterland is consistent with growth of an orogenic plateau during the middle to later Cretaceous.
7. Timing for onset of major thin-skinned thrusting in the Sevier belt varied from Early Cretaceous in central parts at the latitude of Utah to Late Jurassic in more southern and northern parts, reflecting differences in initial width and location of the passive margin sedimentary prism relative to the plate margin. Orogen-wide episodes of Late Jurassic shortening, overall quiescence from 140 to 125 Ma, slower shortening and foreland basin subsidence from approximately 125 to 105 Ma, and increasing shortening rates and foreland subsidence from approximately 105 to 95 Ma were synchronous with changes in activity of the magmatic arc and plate convergence rates, suggesting a dynamically linked orogenic system.

Acknowledgments
This research was funded by National Science Foundation grants EAR-1050073 to Wells and EAR-1050069 to Yonkee. We thank Roman Kislitsyn for the assistance in zircon helium analyses and Lisa Stockli for the help with the laser ablation ICP-MS analysis. Thoughtful reviews by Pete DeCelles, an anonymous reviewer, and Associate Editor Sean Long significantly improved this manuscript. Primary data sets for zircon grain (U/Th)-He ages and sample locations, zircon grain U-Pb ages in depth profiles, and zircon grain fission track counts and ages are available in Tables S1–S3 in the supporting information. Special thanks to David Rodgers whose conversations and initial work on the Willard thrust sheet provided inspiration for this study. Special thanks to Richard Ketcham for augmenting and providing guidance with the FETKIN software package used in thermal modeling, and to Ecopetrol for use of and developmental support for FETKIN.

References

Allmendinger, R. W., & Jordan, T. E. (1984). Mesozoic structure of the Newfoundland Mountains, Utah: Horizontal shortening and subsequent extension in the hinterland of the Sevier belt. *Geological Society of America Bulletin*, *95*(11), 1280–1292. https://doi.org/10.1130/0016-7606(1984)95<1280:MSOTNM>2.0.CO;2

Almendral, A., Robles, W., Parra, M., Mora, A., Ketcham, R. A., & Raghib, M. (2015). FetKin: Coupling kinematic restorations and temperature to predict thrusting, exhumation histories, and thermochronometric ages. *American Association of Petroleum Geologists Bulletin*, *99*(08), 1557–1573. https://doi.org/10.1306/07071411112

Anderson, A. J., Hodges, K. V., & van Soest, M. C. (2017). Empirical constraints on the effects of radiation damage on helium diffusion in zircon. *Geochimica et Cosmochimica Acta*, *218*, 308–322. https://doi.org/10.1016/j.gca.2017.09.006

Anderson, R. B., Long, S. P., Horton, B. K., Thomson, S. N., Calle, A. Z., & Stockli, D. F. (2018). Orogenic wedge evolution of the central Andes, Bolivia (21S): Implications for Cordilleran cyclicity. *Tectonics*, *37*, 1–33. https://doi.org/10.1029/2018TC005132

Angevine, C. L., Heller, P. L., & Paola, C. (1990). *Quantitative sedimentary basin modeling*, *American Association of Petroleum Geologists Short Course Note Series #32*, (p. 247).

Armstrong, F. C., & Oriel, S. S. (1965). Tectonic development of the Idaho-Wyoming thrust belt. *American Association of Petroleum Geologists Bulletin*, *49*, 1847–1866.

Armstrong, R. L. (1968). Sevier orogenic belt in Nevada and Utah. *Geological Society of America Bulletin*, *79*(4), 429–458. https://doi.org/10.1130/0016-7606(1968)79[429:SOBINA]2.0.CO;2

Ault, A. K., Guenthner, W. B., Moser, A. C., Miller, G. H., & Refsnider, K. B. (2018). Zircon grain selection reveals (de)coupled metamictization radiation damage and He diffusivity. *Chemical Geology*, *490*, 1–12. https://doi.org/10.1016/j.chemgeo.2018.04.023

Bargnesi, E. A., Stockli, D. F., Hourigan, J. K., & Hager, C. (2016). Improved accuracy of zircon (U-Th)/He ages by rectifying parent nuclide zonation with practical methods. *Chemical Geology*, *426*, 158–169. https://doi.org/10.1016/j.chemgeo.2016.01.017

Bernet, M. (2009). A field-based estimate of the zircon fission-track closure temperature. *Chemical Geology*, *259*(3-4), 181–189. https://doi.org/10.1016/j.chemgeo.2008.10.043

Bjerrum, C., & Dorsey, R. (1995). Tectonic controls on deposition of Middle Jurassic strata in a retroarc foreland basin, Utah-Idaho trough, western interior, United States. *Tectonics*, *14*(4), 962–978. https://doi.org/10.1029/95TC01448

Bonde, J. W., Hilton, R. P., Jackson, F. D., & Druschke, P. A. (2015). Fauna of the Newark Canyon formation (Lower Cretaceous), east-central Nevada. In W. Pennell, & L. Garside (Eds.), *2015 Geological Society of Nevada Symposium Volume* (pp. 139–150). NV: Reno.

Boyer, S. E., & Elliott, D. (1982). Thrust systems. *American Association of Petroleum Geologists Bulletin*, *66*, 1196–1230.

Brandon, M. T. (1996). Probability density plot for fission-track grain-age samples. *Radiation Measurements*, *26*(5), 663–676. https://doi.org/10.1016/S1350-4487(97)82880-6

Brandon, M. T. (2002). Decomposition of mixed grain age distributions using BINOFIT. *On Track*, *24*, 13–18.

Brandon, M. T., Roden-Tice, M. K., & Garver, J. I. (1998). Late Cenozoic exhumation of the Cascadia accretionary wedge in the Olympic Mountains, northwest Washington State. *Geological Society of America Bulletin*, *110*(8), 985–1009. https://doi.org/10.1130/0016-7606(1998)110<0985:LCEOTC>2.3.CO;2

Brichau, S., Ring, U., Ketcham, R. A., Carter, A., Stockli, D., & Brunel, M. (2006). Constraining the long-term evolution of the slip rate for a major extensional fault system in the central Aegean, Greece, using thermochronology. *Earth and Planetary Science Letters*, *241*(1-2), 293–306. https://doi.org/10.1016/j.epsl.2005.09.065

Burtner, R., & Nigrini, A. (1994). Thermochronology of the Idaho-Wyoming thrust belt during the Sevier orogeny: A new, calibrated multiprocess thermal model. *American Association of Petroleum Geologists Bulletin*, *78*, 1586–1612.

Camilleri, P., & Chamberlain, K. (1997). Mesozoic tectonics and metamorphism in the Pequop Mountains and Wood Hills region, northeast Nevada: Implications for the architecture and evolution of the Sevier orogeny. *Geological Society of America Bulletin*, *109*(1), 74–94. https://doi.org/10.1130/0016-7606(1997)109<0074:MTAMIT>2.3.CO;2

Carrapa, B., Trimble, J. D., & Stockli, D. F. (2011). Patterns and timing of exhumation and deformation in the Eastern Cordillera of NW Argentina revealed by (U-Th)/He thermochronology. *Tectonics*, *30*, TC3003. https://doi.org/10.1029/2010tc002707

Cecil, M. R., Rothberg, G. I., Ducea, M. N., Saleeby, J. B., & Gehrels, G. E. (2012). Magmatic growth and batholitic root development in the northern Sierra Nevada, California. *Geosphere*, *8*(3), 592–606. https://doi.org/10.1130/GES00729.1

Christiansen, E. H., Kowallis, B. J., Dorais, M. J., Hart, G. L., Mills, C. N., Pickard, M., & Parks, E. (2015). The record of volcanism in the Brushy Basin Member of the Morrison formation: Implications for the Late Jurassic of western North America. In T. H. Anderson, A. N. Didenko, C. L. Johnson, A. I. Khanchuk, & J. H. MacDonald, Jr. (Eds.), *Late Jurassic margin of Laurasia—A record of faulting accommodating plate rotation*, *Geological Society of America Special Paper* (Vol. 513, pp. 399–499). https://doi.org/10.1130/2015.2513(11)

Condie, K. C. (1967). Petrology of the late Precambrian tillite(?) association in northern Utah. *Geological Society of America Bulletin*, *78*(11), 1317–1343. https://doi.org/10.1130/0016-7606(1967)78[1317:POTLPT]2.0.CO;2

Coney, J., & Harms, T. A. (1984). Cordilleran metamorphic core complexes: Cenozoic extensional relics of Mesozoic compression. *Geology*, *12*(9), 550–554. https://doi.org/10.1130/0091-7613(1984)12<550:CMCCCE>2.0.CO;2

Coogan, J. C., & King J. (2016). Interim geologic map of the Ogden 30′ × 60′ quadrangle, Box Elder, Cache, Davis, Morgan, Rich, and Summit Counties, Utah, and Uinta County, Wyoming. *Utah Geological Survey Open-File Report* 653DM.

Crittenden, M. C. Jr. (1972). Willard thrust and the Cache allochthon, Utah. *Geological Society of America Bulletin*, *83*(9), 2871–2880. https://doi.org/10.1130/0016-7606(1972)83[2871:WTATCA]2.0.CO;2

Cruz-Uribe, A. M., Hoisch, T. D., Vervoort, J. D., Wells, M. L., & Mazdab, F. K. (2015). Linking thermodynamic modeling, Lu-Hf geochronology, and trace elements in garnet: New *P-T-t* paths from the Sevier hinterland. *Journal of Metamorphic Petrology*, *33*(7), 763–781. https://doi.org/10.1111/jmg.12151

Currie, B. (1998). Upper Jurassic-Lower Cretaceous Morrison and Cedar Mountain formations, NE Utah-NW Colorado: Relationships between nonmarine deposition and early Cordilleran foreland-basin development. *Journal of Sedimentary Research*, *68*(4), 632–652. https://doi.org/10.2110/jsr.68.632

Danišík, M., McInnes, B. I. A., Kirkland, C. L., McDonald, B. J., Evans, N. J., & Becker, T. (2017). Seeing is believing: Visualization of He distribution in zircon and implications for thermal history reconstruction on single crystals. *Science Advances*, *3*(2), e1601121. https://doi.org/10.1126/sciadv.1601121

DeCelles, P. G. (1994). Late Cretaceous-Paleocene synorogenic sedimentation and kinematic history of the Sevier thrust belt, northwest Utah and southwest Wyoming. *Geological Society of America Bulletin*, *106*(1), 32–56. https://doi.org/10.1130/0016-7606(1994)106<0032:LCPSSA>2.3.CO;2

DeCelles, P. G. (2004). Late Jurassic to Eocene evolution of the Cordilleran thrust belt and foreland basin system, western U.S.A. *American Journal of Science*, *504*, 105–168.

DeCelles, P. G., & Coogan, J. (2006). Regional structure and kinematic history of the Sevier fold-and-thrust belt, central Utah. *Geological Society of America Bulletin*, *118*(7-8), 841–864. https://doi.org/10.1130/B25759.1

DeCelles, P. G., & Giles, K. A. (1996). Foreland basin systems. *Basin Research*, *8*(2), 105–123. https://doi.org/10.1046/j.1365-2117.1996.01491.x

DeCelles, P. G., & Graham, S. A. (2015). Cyclical processes in the North American Cordillera orogenic system. *Geology*, *43*(6), 499–502. https://doi.org/10.1130/G36482.1

DeCelles, P. G., Lawton, T. F., & Mitra, G. (1995). Thrust timing, growth of structural culminations, and synorogenic sedimentation in the type Sevier orogenic belt, western United States. *Geology*, *23*(8), 699–702. https://doi.org/10.1130/0091-7613(1995)023<0699:TTGOSC>2.3.CO;2

DeCelles, P. G., Pile, H. T., & Coogan, J. C. (1993). Kinematic history of the Meade thrust based on provenance of the Bechler Conglomerate at Red Mountain, Idaho, Sevier thrust belt. *Tectonics*, *12*(6), 1436–1450. https://doi.org/10.1029/93TC01790

Dickinson, W. R. (2004). Evolution of the North American Cordillera. *Annual Review of Earth and Planetary Sciences*, *32*(1), 13–45. https://doi.org/10.1146/annurev.earth.32.101802.120257

Dickinson, W. R., & Gehrels, G. (2008). Sediment delivery to the Cordilleran foreland basin: Insights from U-Pb ages if detrital zircons in Upper Jurassic and Cretaceous strata of the Colorado Plateau. *American Journal of Science*, *308*, 1041–1082.

Dickinson, W. R., & Lawton, T. F. (2001). Carboniferous to Cretaceous assembly and fragmentation of Mexico. *Geological Society of America Bulletin*, *113*(9), 1142–1160. https://doi.org/10.1130/0016-7606(2001)113<1142:CTCAAF>2.0.CO;2

Dover, J. H. (1995). Geologic map of the Logan 30′ × 60′ quadrangle, Cache and Rich Counties, Utah, and Lincoln and Uinta Counties, Wyoming: U.S. Geological Survey Map I2210, scale 1:100,000.

Drummond, C. N., Wilkinson, B. H., & Lohmann, K. C. (1996). Climatic control of fluvial and lacustrine cyclicity in the Cretaceous Cordilleran foreland basin, western United States. *Sedimentology*, *43*(4), 677–689. https://doi.org/10.1111/j.1365-3091.1996.tb02020.x

Druschke, P., Hanson, A. D., Wells, M. L., Gehrels, G. E., & Stockli, D. (2011). Paleogeographic isolation of the Cretaceous to Eocene Sevier hinterland, east-central Nevada: Insights from U-Pb and (U-Th)/He detrital zircon ages of hinterland strata. *Geological Society of America Bulletin*, *123*(5-6), 1141–1160. https://doi.org/10.1130/B30029.1

Ducea, M. N., & Barton, M. D. (2007). Igniting flare-up events in Cordilleran arcs. *Geology*, *35*(11), 1047–1050. https://doi.org/10.1130/G23898A.1

Elison, M. W. (1995). Jurassic magmatism in the northern Great Basin. In D. M. Miller, & C. Busby (Eds.), *Jurassic magmatism and tectonics of the North American Cordillera*, *Geological Society of America Special Paper* (Vol. 299, pp. 249–265). https://doi.org/10.1130/SPE299-p249

Eyer, J. A. (1969). Gannett Group of western Wyoming and southeastern Idaho. *American Association of Petroleum Geologists Bulletin*, *53*, 1368–1390.

Farley, K. A. (2002). U-Th/He dating: Techniques, calibrations, and applications. *Reviews in Mineralogy and Geochemistry*, *47*(1), 819–844. https://doi.org/10.2138/rmg.2002.47.18

Fosdick, J. C., Carrapa, B., & Ortiz, G. (2015). Placing limits to shortening evolution in the Pyrenees: Role of margin architecture and implications for the Iberia/Europe convergence. *Earth and Planetary Science Letters*, *432*, 73–83. https://doi.org/10.1016/j.epsl.2015.09.041

Fuentes, F., DeCelles, P. G., & Gehrels, G. E. (2009). Jurassic onset of foreland basin deposition in northwestern Montana, U.S.A.: Implications for along-strike synchroneity of Cordilleran orogenic activity. *Geology*, *37*(4), 379–382. https://doi.org/10.1130/G25557A.1

Galbraith, R. F. (1981). On statistical models for fission-track counts. *Journal of Mathematical Geology*, *13*(6), 471–478. https://doi.org/10.1007/BF01034498

Galbraith, R. F. (1990). The radial plot: Graphical assessment of spread in ages. *Nuclear Tracks and Radiation Measurements*, *17*(3), 207–214. https://doi.org/10.1016/1359-0189(90)90036-W

Gallagher, K. (2012). Transdimensional inverse thermal history modeling for quantitative thermochronology. *Journal of Geophysical Research*, *117*, B02408. https://doi.org/10.1029/2011JB008825

Garver, J. I., Reiners, P. W., Walker, L. J., Ramage, J. M., & Perry, S. E. (2005). Implications for timing of Andean uplift from thermal resetting of radiation-damaged zircon in the Cordillera Huayhuash, northern Peru. *Journal of Geology*, *113*(2), 117–138. https://doi.org/10.1086/427664

Gentry, A., Yonkee, W. A., Wells, M. L., & Balgord, E. A. (2018). Resolving the history of early fault slip and foreland basin evolution along the Wyoming salient of the Sevier fold-and-thrust belt: Integrating detrital zircon geochronology, provenance modeling, and subsidence analysis. In R. V. Ingersoll, T. F. Lawton, & S. A. Graham (Eds.), *Tectonics, sedimentary basins, and provenance: A celebration of William R. Dickinson's career*, *Geological Society of America Special Paper 540* (pp. 509–545). https://doi.org/10.1130/2018.2540(23)

Gervais, F., & Brown, R. L. (2011). Testing modes of exhumation in collisional orogens: Synconvergent channel flow in the southeastern Canadian Cordillera. *Lithosphere*, *3*(1), 55–75. https://doi.org/10.1130/L98.1

Gervais, F., & Hynes, A. (2013). Linking metamorphic textures to U-Pb monazite in-situ geochronology to determine the age and nature of aluminosilicate-forming reactions in the northern Monashee Mountains, British Columbia. *Lithos*, *160-161*, 250–267. https://doi.org/10.1016/j.lithos.2012.12.007

Giallorenzo, M. A., Wells, M. L., Yonkee, W. A., Stockli, D. F., & Wernicke, B. P. (2018). Timing of exhumation, Wheeler Pass thrust sheet, southern Nevada and California: Late Jurassic to middle Cretaceous evolution of the southern Sevier fold-thrust belt. *Geological Society of America Bulletin*, *130*(3-4), 558–579. https://doi.org/10.1130/B31777.1

Gillespie, J. M., & Heller, P. L. (1995). Beginning of foreland subsidence in the Columbia-Sevier belts, southern Canada and northwest Montana. *Geology*, *25*, 723–726.

Gleadow, A. J. W., Hurford, A. J., & Quaife, R. D. (1976). Fission-track dating of zircon: Improved etching techniques. *Earth and Planetary Science Letters*, *33*(2), 273–276. https://doi.org/10.1016/0012-821X(76)90235-1

Green, P. F., & Hurford, A. J. (1983). The zeta age calibration of fission-track dating. *Chemical Geology*, *1*, 285–317.

Guedes, S., Moreira, P., Devanathan, R., Weber, W. J., & Hadler, J. C. (2013). Improved zircon fission-track annealing model based on reevaluation of annealing data. *Physics and Chemistry of Minerals*, *40*(2), 93–106. https://doi.org/10.1007/s00269-012-0550-8

Guenthner, W., Reiners, P., DeCelles, P. G., & Kendall, J. (2015). Sevier belt exhumation in central Utah constrained from complex zircon (U-Th)/He data sets: Radiation damage and He inheritance effects on partially reset detrital zircons. *Geological Society of America Bulletin*, *127*(3-4), 323–348. https://doi.org/10.1130/B31032.1

Guenthner, W., Reiners, P., Ketcham, R., Nasdala, L., & Giester, G. (2013). Helium diffusion in natural zircon: Radiation damage, anisotropy, and the interpretation of zircon U-Th/He thermochronology. *American Journal of Science*, *313*, 1–54.

Heller, P. L., Bowdler, S., Chambers, H., Coogan, J. C., Hagen, E., Shuster, M., et al. (1986). Time of initial thrusting in the Sevier orogenic belt, Idaho-Wyoming and Utah. *Geology*, *14*, 288–291.

Heller, P. L., & Paola, C. (1989). The paradox of Lower Cretaceous gravels and the initiation of thrusting in the Sevier orogenic belt, United States Western Interior. *Geological Society of America Bulletin*, *101*(6), 864–875. https://doi.org/10.1130/0016-7606(1989)101<0864:TPOLCG>2.3.CO;2

Herman, F., Copeland, P., Avouac, J., Bollinger, L., Maheo, G., Le Fort, P., et al. (2010). Exhumation, crustal deformation, and thermal structure of the Nepal Himalaya derived from the inversion of thermochronological and thermobarometric data. *Journal of Geophysical Research*, *115*, B06407. https://doi.org/10.1029/2008jb006126

Hoisch, T. D., Wells, M. L., Beyene, M. A., Styger, S., & Vervoort, J. D. (2014). Jurassic Barrovian metamorphism in a western U.S. Cordilleran metamorphic core complex, Funeral Mountains, California. *Geology*, *42*(5), 399–402. https://doi.org/10.1130/G35352.1

Hourigan, J. K., Reiners, P. W., & Brandon, M. T. (2005). U-Th zonation-dependent alpha ejection in (U-Th)/He chronometry. *Geochimica et Cosmochimica Acta*, *69*(13), 3349–3365. https://doi.org/10.1016/j.gca.2005.01.024

Hubbert, M. K., & Rubey, W. W. (1959). Role of fluid pressure in mechanics of overthrust faulting 1. Mechanics of fluid-filled porous solids and its application to overthrust faulting. *Geological Society of America Bulletin*, *70*, 115–166.

Hunt, G. J., Lawton, T. F., & Kirkland, J. I. (2011). Detrital zircon U-Pb geochronological provenance of Lower Cretaceous strata, foreland basin, Utah. In D. A. Sprinkel, W. A. Yonkee, & T. C. Chidsey, Jr. (Eds.), *Sevier thrust belt: Northern and central Utah and adjacent areas*, *Utah Geological Association Publication*, (Vol. 40, pp. 193–211).

Iglewicz, B., & Hoaglin, D. (1993). How to detect and handle outliers (Volume 16). In E. F. Mykyta (Ed.), *The ASQC Basic References in Quality Control: Statistical Techniques*. (p. 87). Milwaukee, WI: ASQC Quality Press.

Imlay, R. W. (1980). Jurassic paleobiogeography of the conterminuous United States and its continental setting. *U.S. Geological Survey Professional Paper* 1062, 134 p.

Jordan, T. E. (1981). Thrust loads and foreland basin evolution, Cretaceous, western United States. *American Association of Petroleum Geologists Bulletin*, *65*, 2506–2520.

Jordan, T. E. (1985). Tectonic setting and petrography of Jurassic foreland basin sandstone, Idaho-Utah-Wyoming. In G. J. Kearns, & R. L. Kearns (Eds.), *Orogenic patterns and stratigraphy of north-central Utah and southeastern Idaho*, *Utah Geological Association Publication*, (Vol. 14, pp. 201–214).

Ketcham, R. A. (2005). Forward and inverse of low-temperature thermochronology data. *Reviews in Mineralogy and Geochemistry*, *58*(1), 275–314. https://doi.org/10.2138/rmg.2005.58.11

Ketcham, R. A., Guenthner, W. R., & Reiners, P. W. (2013). Geometric analysis of radiation damage connectivity in zircon, and its implications for helium diffusion. *American Mineralogist*, *98*(2-3), 350–360. https://doi.org/10.2138/am.2013.4249

Laskowski, A. K., DeCelles, P. G., & Gehrels, G. E. (2013). Detrital zircon geochronology of Cordilleran retroarc foreland basin strata, western North America. *Tectonics*, *32*, 1027–1048. https://doi.org/10.1002/tect.20065

Lawton, T. F. (1994). Tectonic setting of Mesozoic sedimentary basins, Rocky Mountain region, United States. In M. V. Caputo, J. A. Peterson, & K. J. Franczyk (Eds.), *Mesozoic systems of the Rocky Mountain region*, (pp. 1–26). Denver, CO: USA, SEPM Rocky Mountain Section Publication.

Lawton, T. F., Hunt, G. J., & Gehrels, G. E. (2010). Detrital zircon record of thrust belt unroofing in Lower Cretaceous synorogenic conglomerates, central Utah. *Geology*, *38*(5), 463–466. https://doi.org/10.1130/G30684.1

Leier, A. L., & Gehrels, G. E. (2011). Continental-scale detrital zircon provenance signatures in Lower Cretaceous strata, western North America. *Geology*, *39*(4), 399–402. https://doi.org/10.1130/G31762.1

Liu, L., Spasojevic, S., & Gurnis, M. (2008). Reconstructing Farallon plate subduction beneath North America back to the Late Cretaceous. *Science*, *322*(5903), 934–938. https://doi.org/10.1126/science.1162921

Liu, S., Nummedal, D., & Gurnis, M. (2014). Dynamic versus flexural controls of Late Cretaceous Western Interior Basin, USA. *Earth and Planetary Science Letters*, *389*, 221–229. https://doi.org/10.1016/j.epsl.2014.01.006

Lock, J., & Willett, S. (2008). Low-temperature thermochronometric ages in fold-and-thrust belts. *Tectonophysics*, *456*(3-4), 147–162. https://doi.org/10.1016/j.tecto.2008.03.007

Long, S. P. (2013). Magnitudes and spatial patterns of erosional exhumation in the Sevier hinterland, eastern Nevada and western Utah, USA: Insights from a Paleogene paleogeographic map. *Geosphere*, *8*, 881–901. https://doi.org/10.1130/GES00783.1

Long, S. P., Henry, C. D., Muntean, J. L., Edmondo, G. P., & Cassel, E. J. (2014). Early Cretaceous construction of a structural culmination, Eureka, Nevada, U.S.A.: Implications for out-of-sequence deformation in the Sevier hinterland. *Geosphere*, *10*(3), 564–584. https://doi.org/10.1130/GES00997.1

Long, S. P., McQuarrie, N., Tobgay, T., Coutand, I., Cooper, F. J., Reiners, P. W., et al. (2012). Variable shortening rates in the eastern Himalaya thrust belt, Bhutan: Insights from multiple thermochronologic and geochronologic data sets tied to kinematic reconstructions. *Tectonics*, *31*, TC5004, 23 p. https://doi.org/10.1029/2012tc003155

Mancktelow, N. S., & Grasemann, B. (1997). Time-dependent effects of heat advection and topography on cooling histories during erosion. *Tectonophysics*, *270*(3-4), 167–195. https://doi.org/10.1016/S0040-1951(96)00279-X

Marsh, J. H., & Stockli, D. F. (2015). Zircon U–Pb and trace element zoning characteristics in an anatectic granulite domain: Insights from LASS-ICP-MS depth profiling. *Lithos*, *239*, 170–185. https://doi.org/10.1016/j.lithos.2015.10.017

Martin, A. J., Wyld, S. J., Wright, J. E., & Bradford, J. H. (2010). The Lower Cretaceous King Lear formation, northwest Nevada: Implications for Mesozoic orogenesis in the western US Cordillera. *Geological Society of America Bulletin*, *122*(3-4), 537–562. https://doi.org/10.1130/B26555.1

Matthews, K. J., Seton, M., & Muller, R. D. (2012). A global-scale pate reorganization event at 105–100 Ma. *Earth and Planetary Science Letters*, *355-356*, 283–298. https://doi.org/10.1016/j.epsl.2012.08.023

McGrew, A. J., Peters, M. T., & Wright, J. E. (2000). Thermobarometric constraints on the tectonothermal evolution of the East Humboldt Range metamorphic core complex, Nevada. *Geological Society of America Bulletin*, *112*(1), 45–60. https://doi.org/10.1130/0016-7606(2000)112<45:TCOTTE>2.0.CO;2

McQuarrie, N., & Ehlers, T. A. (2015). Influence of thrust belt geometry and shortening rate on thermochronometer cooling ages: Insights from thermokinematic and erosion modeling of the Bhutan Himalaya. *Tectonics*, *34*, 1055–1079. https://doi.org/10.1002/2014TC003783

Meesters, A. G., & Dunai, T. J. (2002). Solving the production-diffusion equation for finite diffusion domains of various shapes: Part 2—Applications to cases with α ejection and non-homogeneous distribution of the source. *Chemical Geology*, *186*(3-4), 345–363. https://doi.org/10.1016/S0009-2541(02)00072-4

Miller, D. M., Hillhouse, W. C., Zartman, R. E., & Lanphere, M. A. (1997). Geochronology of intrusive and metamorphic rocks in the Pilot range, Utah and Nevada, and comparison with regional patterns. *Geological Society of America Bulletin*, *99*, 866–879.

Miller, D. M., & Hoisch, T. D. (1995). Jurassic tectonics of northeastern Nevada and northwestern Utah from the perspective of barometric studies. In D. M. Miller, & C. Busby (Eds.), *Jurassic magmatism and tectonics of the North American cordillera*, *Geological Society of America Special Paper*, (Vol. 299, pp. 267–294). https://doi.org/10.1130/SPE299-p267

Mitrovica, J. X., Beaumont, C., & Jarvis, G. T. (1989). Tilting of continental interiors by the dynamical effects of subduction. *Tectonics*, *8*(5), 1079–1094. https://doi.org/10.1029/TC008i005p01079

Morgan, W. J. (1965). Gravity anomalies and convection currents: 1—A sphere and sylinder sinking beneath the surface of a viscous fluid. *Journal of Geophysical Research*, *70*(24), 6175–6187. https://doi.org/10.1029/JZ070i024p06175

Mouthereau, F., Filleaudeau, P.-Y., Vacherat, A., Pik, R., Lacombe, O., Fellin, M. G., et al. (2014). Placing limits to shortening evolution in the Pyrenees: Role of margin architecture and implications for the Iberia/Europe convergence. *Tectonics*, *33*, 2283–2314. https://doi.org/10.1002/2014tc003663

Mulcahy, S. R., Starnes, J. K., Day, H. W., Coble, M. A., & Vervoort, J. D. (2018). Early onset of Franciscan subduction. *Tectonics*, *37*(5), 1194–1209. https://doi.org/10.1029/2017TC004753

Naeser, C. W. (1979). Fission-track dating and geologic annealing of fission tracks. In E. Jager, & J. C. Hunziker (Eds.), *Lectures in isotope geology* (pp. 154–169). New York: Springer-Verlag. https://doi.org/10.1007/978-3-642-67161-6_10

Naeser, C. W., Bryant, B., & Crittenden, M. D. (1983). Fission-track ages of apatite in the Wasatch Mountains, Utah: An uplift study. *Geological Society of America Memoirs*, *157*, 29–36. https://doi.org/10.1130/MEM157-p29

Orme, D. A., Guenthner, W. R., Laskowski, A. K., & Reiners, P. W. (2016). Long-term tectonothermal history of Laramide basement from zircon He age-eU correlations. *Earth and Planetary Science Letters*, *453*, 119–130. https://doi.org/10.1016/j.epsl.2016.07.046

Painter, C. S., & Carrapa, B. (2013). Flexural versus dynamic processes of subsidence in the North American Cordillera foreland basin. *Geophysical Research Letters*, *40*, 4249–4253. https://doi.org/10.1002/grl.50831

Pana, D. I., & van der Pluijm, B. A. (2015). Orogenic pulses in the Alberta Rocky Mountains: Radiometric dating of major faults and comparison with the regional tectono-stratigraphic record. *Geological Society of America Bulletin*, *127*(3-4), 480–502. https://doi.org/10.1130/B31069.1

Parra, M., Mora, A., Sobel, E. R., Strecker, M. R., & Gonzalez, R. (2009). Episodic orogenic front migration in the northern Andes: Constraints from low-temperature thermochronology in the Eastern Cordillera, Columbia. *Tectonics*, *28*, TC4004, 27 p. https://doi.org/10.1029/2008tc002423

Paterson, S. R., & Ducea, M. N. (2015). Arc magmatic tempos: Gathering the evidence. *Elements*, *11*(2), 91–98. https://doi.org/10.2113/gselements.11.2.91

Petrus, J. A., & Kamber, B. S. (2012). VizualAge: A novel approach to laser ablation ICP-MS U-Pb geochronology data reduction. *Geostandards and Geoanalytical Research*, *36*(3), 247–270. https://doi.org/10.1111/j.1751-908X.2012.00158.x

Powell, J., Schneider, D., Stockli, D., & Fallas, K. (2016). Zircon (U-Th)/He thermochronology of Neoproterozoic strata from the Mackenzie Mountains, Canada: Implications for the Phanerozoic exhumation and deformation history of the northern Canadian Cordillera. *Tectonics*, *35*, 663–689. https://doi.org/10.1002/2015TC003989

Price, R. A. (1994). Chapter 2-Cordilleran tectonics and the evolution of the western Canada sedimentary basin. In G. D. Mossop, & I. Shetsen (Eds.), *Geological Atlas of the Western Canada Sedimentary Basin*, *Canadian Society of Petroleum Geologists and Alberta Research Council* (pp. 13–24). https://ags.aer.ca/document/Atlas/chapter_2.pdf

Pujols, E. J., Stockli, D. F., Constenius, K. N., & Horton, B. K. (2018). Interplay between deformation and proximal foreland sedimentation in the Late Cretaceous Sevier orogenic belt. *American Geophysical Union* abstract #T41E-0349.

Rahn, M. K., Brandon, M. T., Batt, G. E., & Garver, J. I. (2004). A zero-damage model for fission-track annealing in zircon. *American Mineralogist*, *89*(4), 473–484. https://doi.org/10.2138/am-2004-0401

Raines, M. K., Hubbard, S. M., Kukulski, R. B., Leier, A. L., & Gehrels, G. E. (2013). Sediment dispersal in an evolving foreland: Detrital zircon geochronology from Upper Jurassic and lowermost Cretaceous strata, Alberta Basin, Canada. *Geological Society of America Bulletin*, *125*(5-6), 741–755. https://doi.org/10.1130/B30671.1

Rak, A. J., McQuarrie, N., & Ehlers, T. A. (2017). Kinematics, exhumation, and sedimentation of the north central Andes (Bolivia): An integrated thermochronometer and thermokinematic modeling approach. *Tectonics*, *36*, 2524–2554. https://doi.org/10.1002/2016TC004440

Reiners, P. W. (2005). Zircon (U-Th)/He thermochronometry. *Reviews in Mineralogy and Geochemistry*, *58*(1), 151–179. https://doi.org/10.2138/rmg.2005.58.6

Reiners, P. W., & Brandon, M. T. (2006). Using thermochronology to understand orogenic erosion. *Annual Review of Earth and Planetary Sciences*, *34*(1), 419–466. https://doi.org/10.1146/annurev.earth.34.031405.125202

Reiners, P. W., & Ehlers, T. A. (2005). *Low-temperature thermochronology: Techniques, interpretations, and applications*, *Reviews in Mineralogy and Geochemistry* (Vol. 58). 22 chap.

Reiners, P. W., Spell, T. L., Nicolescu, S., & Zanetii, K. A. (2004). Zircon (U-Th)/He thermo-chronometry: He diffusion and comparisons with $^{40}Ar/^{39}Ar$ dating. *Geochimica et Cosmochimica Acta*, *68*(8), 1857–1887. https://doi.org/10.1016/j.gca.2003.10.021

Rodgers, D. W., & Janecke, S. U. (1992). Tertiary paleogeographic maps of the western Idaho-Wyoming-Montana thrust belt. In P. K. Link, M. A. Kuntz, & L. B. Platt (Eds.), *Regional geology of Eastern Idaho and Western Wyoming*, *Geological Society of America Memoir* (Vol. 179, pp. 83–94). https://doi.org/10.1130/MEM179-p83

Royse, F. Jr. (1993). An overview of the geologic structure of the thrust belt in Wyoming, northern Utah, and eastern Idaho. In A. W. Snoke, J. R. Steidtmann, & S. M. Roberts (Eds.), *Geology of Wyoming: Geological Survey of Wyoming Memoir* No. 5 (pp. 272–311). Laramie, WY: Wyoming Geological Survey.

Rubey, W. W. (1973). *New Cretaceous formations in western Wyoming thrust belt*, *U.S. Geological Survey Bulletin 1372-1*, (p. 35).

Saleeby, J. B. (2003). Segmentation of the Laramide slab—Evidence from the southern Sierra Nevada region. *Geological Society of America Bulletin*, *115*, 655–668. https://doi.org/10.1130/0016-7606(2003)115<0655:SOTLSF>2.0.CO;2

Schweickert, R. A. (2015). Jurassic evolution of the Western Sierra Nevada metamorphic province. In T. H. Anderson, A. N. Didenko, C. L. Johnson, A. I. Khanchuk, & J. H. MacDonald, Jr. (Eds.), *Late Jurassic margin of Laurasia—A record of faulting accommodating plate rotation*, *Geological Society of America Special Paper* (Vol. 513, pp. 299–358). https://doi.org/10.1130/2015.2513(08)

Seton, M., Muller, R. D., Zahirovic, S., Gaina, C., Torsvik, T., Shelhard, G., et al. (2012). Global continental and ocean basin reconstructions since 200 Ma. *Earth-Science Reviews*, *113*(3-4), 212–270. https://doi.org/10.1016/j.earscirev.2012.03.002

Sharman, G. R., Graham, S. A., Grove, M., Kimbrough, D. L., & Wright, J. E. (2015). Detrital zircon provenance of the Late Cretaceous–Eocene California forearc: Influence of Laramide low-angle subduction on sediment dispersal and paleogeography. *Geological Society of America Bulletin*, *127*(1-2), 38–60. https://doi.org/10.1130/B31065.1

Simony, S., & Carr, S. D. (2011). Cretaceous to Eocene evolution of the southeastern Canadian Cordillera: Continuity of Rocky Mountain thrust systems with zones of "in-sequence" mid-crustal flow. *Journal of Structural Geology*, *23*, 1417–1434. https://doi.org/10.1016/j.jsg.2011.06.001

Singleton, J. S., Stockli, D. F., Gans, P. B., & Prior, M. G. (2014). Timing, rate, and magnitude of slip on the Buckskin-Rawhide detachment fault, west central Arizona. *Tectonics*, *33*, 1596–1615. https://doi.org/10.1002/2013TC003517

Snell, K. E., Koch, P. L., Druschke, P., Foreman, B. Z., & Eiler, J. M. (2014). High elevation of the "Nevadaplano" during the Late Cretaceous. *Earth and Planetary Science Letters*, *386*, 52–63. https://doi.org/10.1016/j.epsl.2013.10.046

Sprinkel, D. A., Doelling, H. H., Kowallis, B. J., Waanders, G., & Kuehne, P. A. (2015). Early results of a study of the Middle Jurassic strata in the Sevier fold and thrust belt, Utah. In D. A. Sprinkel, W. A. Yonkee, & T. C. Chidsey, Jr. (Eds.), *Sevier thrust belt: Northern and central Utah and adjacent areas*, *Utah Geological Association Guidebook* (Vol. 40, pp. 151–172).

Sprinkel, D. A., Weiss, M. P., Fleming, R. W., & Waanders, G. L. (1999). *Redefining the Lower Cretaceous stratigraphy within the central Utah foreland basin*, *Utah Geological Survey Special Study* (Vol. 97, p. 21).

Stockli, D. F. (2005). Applications of low-temperature thermochronometry to extensional settings. In Reiners, P.W., & Ehlers, T.A. (Eds.). *Reviews in Mineralogy and Geochemistry*, *58*(1), 411–448. https://doi.org/10.2138/rmg.2005.58.16

Stockli, D. F., Linn, J. K., Walker, J. D., & Dumitru, T. A. (2001). Miocene unroofing of the Canyon Range during extension along the Sevier Desert detachment, west-central Utah. *Tectonics*, *20*(3), 289–307. https://doi.org/10.1029/2000TC001237

Tagami, T., Galbraith, R. F., Yamada, R., & Laslett, G. M. (1998). Revised annealing kinetics of fission tracks in zircon and geological implications. In P. van den Haute & F. De Corte (Eds.), *Advances in Fission-Track Geochronology*, *Solid Earth Sciences Library* (Vol. 10). Dordrecht: Springer.

Taylor, W., Bartley, J., Martin, M., Geissman, J., Walker, J., & Armstrong, P. (2000). Relations between hinterland and foreland shortening: Sevier orogeny, central North American Cordillera. *Tectonics*, *196*, 1124–1143. https://doi.org/10.1029/1999TC001141

von Hagke, C., Cederbom, C. E., Oncken, O., Stockli, D. F., Rahn, M. K., & Schlunegger, F. (2012). Linking the northern Alps with their foreland: The latest exhumation history resolved by low-temperature thermochronology. *Tectonics*, *31*, TC 5010, 25 p. https://doi.org/10.1029/2011TC003078

Wakabayashi, J. (2015). Anatomy of a subduction complex: architecture of the Franciscan Complex, California, at multiple length and time scales. *International Geology Review*, *57*(5-8), 669–746. https://doi.org/10.1080/00206814.2014.998728

Webster, E. R., Pattison, D., & DuFrane, S. A. (2017). Geological constrains on magmatism and polyphase deformation and metamorphism in the southern Omineca Belt, British Columbia. *Canadian Journal of Earth Sciences*, *54*(5), 529–549. https://doi.org/10.1139/cjes-2016-0126

Weisberg, W. R., Metcalf, J. R., & Flowers, R. M. (2018). Distinguishing slow cooling versus multiphase cooling and heating in zircon and apatite (U-Th)/He datasets: The case of the McClure Mountain syenite standard. *Chemical Geology*, *485*, 90–99. https://doi.org/10.1016/j.chemgeo.2018.03.038

Wells, M. L. (1997). Alternating contraction and extension in the hinterlands of orogenic belts: An example from the Raft River Mountains, Utah. *Geological Society of America Bulletin*, *109*(1), 107–126. https://doi.org/10.1130/0016-7606(1997)109<0107:ACAEIT>2.3.CO;2

Wells, M. L. (2016). A major mid-Cretaceous shortening event in the southern Sevier orogenic belt; Continental record of global plate reorganization? *Geological Society of America Abstracts with Programs*, *48*(7). https://doi.org/10.1130/abs/2016AM-287809

Wells, M. L., Hoisch, T., Cruz-Uribe, A., & Vervoort, J. (2012). Geodynamics of synconvergent extension and tectonic mode switching: Constraints from the Sevier-Laramide orogeny. *Tectonics*, *31*, TC 1002, 20 p. https://doi.org/10.1029/2011TC002913

Wells, M. L., Snee, L. W., & Blythe, A. E. (2000). Dating of major normal fault systems using thermochronology: An example from the Raft River detachment, Basin and Range, western United States. *Journal of Geophysical Research*, *105*(B7), 16303–16327. https://doi.org/10.1029/2000JB900094

Wells, M. L., Spell, T. L., Hoisch, T. D., Arriola, T., & Zanetti, K. A. (2008). Laser-probe $^{40}Ar/^{39}Ar$ dating of strain fringes: Mid-Cretaceous synconvergent orogen-parallel extension in the interior of the Sevier orogeny. *Tectonics*, *27*, TC3012, 20 p. https://doi.org/10.1029/2007TC002153

Wells, M. L., Yonkee, W. A., Giallorenzo, M. A., Spell, T. L., & Zanetti, K. (2015). UV laserprobe $^{40}Ar/^{39}Ar$ dating of early internal strain and late fluid-induced strain localization associated with the Willard thrust, Utah. *Geological Society of America Abstracts with Programs*, *47*(7), 227.

Wiltschko, D. V., & Dorr, J. A. (1983). Timing of deformation in overthrust belt and foreland of Idaho, Wyoming, and Utah. *American Association of Petroleum Geologists Bulletin*, *67*, 1304–1322. https://doi.org/10.1306/03b5b740-16d1-11d7-8645000102c1865d

Wolfe, M. R., & Stockli, D. F. (2010). Zircon (U-Th)/He thermochronometry in the KTB drill hole, Germany, and its implication for bulk He diffusion kinetics in zircon. *Earth and Planetary Science Letters*, *295*(1-2), 69–82. https://doi.org/10.1016/j.epsl.2010.03.025

Wyld, S. J. (2002). Structural evolution of a Mesozoic backarc fold-and-thrust belt in the U.S. Cordillera: New evidence from northern Nevada. *Geological Society of America Bulletin*, *114*(11), 1452–1468. https://doi.org/10.1130/0016-7606(2002)114<1452:SEOAMB>2.0.CO;2

Wyld, S. J., & Wright, J. E. (2014). Jurassic back-arc magmatism in the eastern Great Basin: A product of slab-tear due to localized arc collision at the plate boundary. *Geological Society of America Abstract with Porgrams*, *46*(5), 19.

Yamada, R., Murakami, M., & Tagami, T. (2007). Statistical modelling of annealing kinetics of fission tracks in zircon: Reassessment of laboratory experiments. *Chemical Geology*, *236*(1-2), 75–91. https://doi.org/10.1016/j.chemgeo.2006.09.002

Yonkee, W. A. (1992). Basement-cover relations, Sevier orogenic belt, northern Utah. *Geological Society of America Bulletin*, *104*(3), 280–302. https://doi.org/10.1130/0016-7606(1992)104<0280:BCRSOB>2.3.CO;2

Yonkee, W. A. (2005). Strain patterns within part of the Willard thrust sheet, Idaho-Utah-Wyoming thrust belt. *Journal of Structural Geology*, *27*(7), 1315–1343. https://doi.org/10.1016/j.jsg.2004.06.014

Yonkee, W. A., Czeck, D. M., Nachbor, A. C., Barszewski, C., Pantone, S., Balgord, E. A., & Johnson, K. R. (2013). Strain accumulation and fluid-rock interaction in a naturally deformed diamictite, Willard thrust system, Utah (USA): Implications for crustal rheology and strain softening. *Journal of Structural Geology*, *50*, 91–118. https://doi.org/10.1016/j.jsg.2012.10.012

Yonkee, W. A., Dehler, C. D., Link, P. K., Balgord, E. A., Keeley, J. A., Hayes, D. S., et al. (2014). Tectono-stratigraphic framework of Neoproterozoic to Cambrian strata, west-central US: Protracted rifting, glaciation, and evolution of the North American Cordilleran margin. *Earth Science Reviews*, *136*, 59–95. https://doi.org/10.1016/j.earscirev.2014.05.004

Yonkee, W. A., Parry, W. P., Bruhn, R. L., & Cashman, P. (1989). Thermal models of thrusting: Constraints from fluid-inclusion observations, Willard thrust sheet, Idaho-Utah-Wyoming thrust belt. *Geological Society of America Bulletin*, *101*(2), 304–313. https://doi.org/10.1130/0016-7606(1989)101<0304:TMOTFC>2.3.CO;2

Yonkee, W. A., & Weil, A. B. (2015). Tectonic evolution of the Sevier and Laramide belts within the North American Cordilleran orogenic system. *Earth Science Reviews*, *150*, 531–593. https://doi.org/10.1016/j.earscirev.2015.08.001